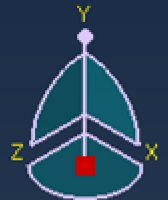
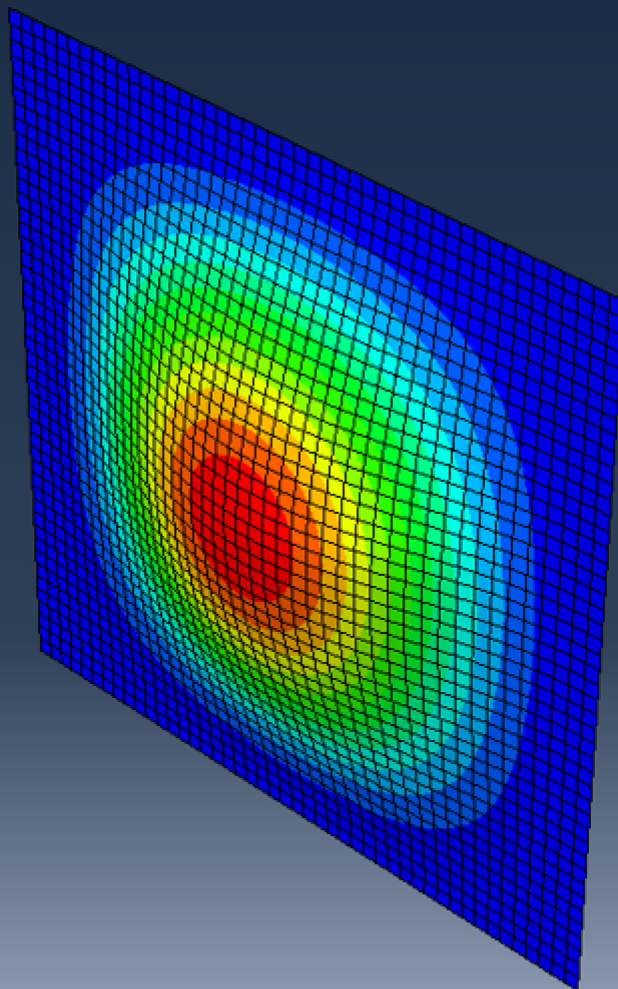


Non-linear buckling analysis of GFRP plates

A numerical approach with progressive failure analysis

B. Renckens



Non-linear buckling analysis of GFRP plates

A numerical approach with progressive failure analysis

by

B. Renckens

to obtain the degree of Master of Science
at the Delft University of Technology,
to be defended publicly on Monday July 5th, 2021 at 10:00 AM.

Student number:	4223284	
Thesis committee:	dr. M. Pavlović,	TU Delft
	ir. T. Boeters	Royal HaskoningDHV
	ir. L. Tromp	Royal HaskoningDHV
	dr. ir. F. P. van der Meer	TU Delft
	ir. A. Christoforidou	TU Delft

An electronic version of this thesis is available at <http://repository.tudelft.nl/>.

Preface

Dear reader,

This thesis is written to conclude the Master Structural Engineering at the faculty of Civil Engineering and Geosciences at the Delft University of Technology. The research was performed under the supervision of my graduation committee and in cooperation with the engineering and consultancy firm Royal HaskoningDHV.

I would like to thank all of my supervisors for their guidance and support during this project. First of all, I would like to express my gratitude towards Royal HaskoningDHV for giving me the opportunity to finish this thesis and for providing me with great guidance. Ton Boeters, thank you for your endless encouragement and advice. Liesbeth Tromp, thank you for your knowledge and out-of-the-box thinking. Secondly, I would like to thank Marko Pavlović, my daily supervisor and chairman of my graduation committee, who guided me with a lot of persistence and generously offered his expertise every time that I needed help. Furthermore, I would like to thank Frans van der Meer for his critical notes, Angeliki Chrisoforiou for always taking her time for me when needed and Lieuwe van der Meer who laid out the path for this thesis. I feel grateful to all who have helped me during the process of writing this thesis.

After finishing this thesis, my time as a student in Delft comes to an end. I want to thank my friends for the time we spent together. Aukje, Natalia and Rick, thank you for all the welcome distractions during my studies and this thesis in particular. I am very grateful for the support of my family; you always believed in me and provided continuous support. And last but not least, I would like to thank Dennis for always encouraging me.

I hope you enjoy reading my thesis as much as I enjoyed writing it.

*Berber Renckens
Delft, July 2021*

Abstract

Fiber Reinforced Polymer (FRP) has increased rapidly in popularity in the past few decades. The material's advantageous properties, such as a high strength-to-weight ratio and low required maintenance, gave rise to its popularity in multiple major engineering branches. Buckling behaviour develops due to the notably low stiffness-to-strength ratio and the usual high slenderness of FRP plates. The occurrence of initial imperfections increases the tendency of the material to buckle. This study focuses on the non-linear buckling behaviour of a GFRP plate with progressive failure analysis.

The load-carrying capacity of structures with post-buckling behaviour can be determined with progressive failure analysis, which requires a damage model that characterises the onset and evolution of damage. In Abaqus, the Hashin damage model is implemented by default, which considers the four failure modes of the material: fibres in tension, fibres in compression, the matrix in tension and the matrix in compression. Numerical analysis of strain-softening materials with local damage leads to deformation localisation in a single element: a finer mesh will decrease the amount of energy dissipated. To prevent this localisation into arbitrarily small regions, the stress is related to the deformation of a finite volume. The damage evolution is described with a stress-displacement response instead of a stress-strain response. The energy needed to open a unit area of the crack, the fracture energy, is defined as a material parameter and depends on the mesh size of the model.

The assessment of fracture energy properties in composite materials is challenging due to specimen geometry and fibre lay-up, and accurate data of GFRP fracture energy is largely unknown. When no actual post-failure behaviour is acquired, the lower bound fracture energy can be determined from the material properties. A numerical analysis is performed to determine if the lower bound value can be applied for non-linear buckling analysis of GFRP plates. For this analysis, two data sets were used. Uni-directional and multi-directional coupon tests performed on a GFRP plate with a $[90/0_3/45/-45/0_2]_s$ lay-up and experimental buckling tests of a GFRP plate consisting of different variations of 0° and $\pm 45^\circ$ layers. The non-linear buckling analysis is performed on the material of the first data set. The second data set is used as a verification method.

The difference between the stress-displacement and stress-strain response is numerically analysed with a one-element model with constant fracture energy input and changing mesh size. Numerical analysis of the uni-directional coupon experiments is performed to determine the input values and response of the lower bound fracture energy. The lower bound fracture energy implementation results in an abrupt drop in stress when the material strength is reached. Increasing the lower bound fracture energy by a minimum of 2% prevented numerical inconsistencies. Progressive failure analysis of the multi-directional coupons experiments validated an increase of 10% for the lower bound values. The use of lower bound fracture energy for non-linear buckling analysis is verified with progressive failure analysis of the buckling experiments. The lower bound fracture energy, increased by 10%, approximates the ultimate strength of six tests with an average difference of 7.7%.

To analyse the non-linear buckling behaviour of a GFRP plate, a buckling curve is created by varying the plate thickness. The influence of geometric imperfections on a plate's buckling strength is studied by applying different initial imperfections. Two types of boundary conditions are used to analyse if they result in a different buckling curve. A difference in the buckling strength reduction factor of 0.1 is found. Initial imperfections reduce the buckling strength of the material, which is most apparent for plate slenderness around 1.0. An initial imperfection of B/125 resulted in a 40% strength reduction compared to the elastic buckling strength. The average difference in reduction factor between an initial imperfection of B/1000 and B/125 was 16%, with a maximum difference of 26%. The conservative option of B/125, as recommended by the design codes, resulted in up to 26% higher strength reduction compared to an initial imperfection of B/1000, and can lead to over dimensioning of the plates.

Contents

Preface	i
Abstract	iii
List of Figures	vii
List of Tables	xi
List of Symbols	xiii
List of Abbreviations	xv
1 Introduction	1
1.1 Introduction	1
1.2 Scope	2
1.3 Problem statement	2
1.4 Aim and objective.	3
1.5 Methodology	3
2 Literature review	4
2.1 Introduction	4
2.1.1 Fibres	4
2.1.2 Resin	5
2.2 Material properties	5
2.2.1 Determination of material properties from coupon tests	6
2.3 Failure behaviour	7
2.3.1 Mechanical behaviour in fibre direction	8
2.3.2 Mechanical behaviour in transverse direction	8
2.4 Damage model	8
2.4.1 Development of failure criteria	9
2.4.2 Damage initiation	10
2.4.3 Damage evolution	12
2.5 Buckling behaviour	15
2.5.1 Buckling design	15
2.5.2 Initial imperfections	16
2.5.3 JRC - Prospect for new guidance in the design of FRP	17
2.5.4 CUR96 - Dutch design guidance for infrastructure	18
2.6 Conclusion	19
3 One-element model	21
3.1 Equivalent displacement model	21
3.2 Material properties	23
3.3 Conventional shell element results	24
3.4 Continuum shell element results	26
3.5 Conclusion	27
4 Uni-directional model	28
4.1 Uni-directional coupon tests	28
4.1.1 Model properties	28
4.1.2 Post-failure behaviour experiments	30
4.1.3 Lower bound fracture energy	30
4.1.4 Material properties	31
4.1.5 Models loaded in tension.	32

4.1.6	Models loaded in compression	34
4.1.7	Fracture energy input below the lower bound value	36
4.1.8	Larger mesh size	37
4.2	Conclusions	38
5	Multi-directional model	40
5.1	Multi-directional coupon tests	40
5.1.1	Modelling approach	41
5.1.2	Material properties	42
5.2	Test results	42
5.2.1	Lower bound fracture energy	42
5.2.2	MDT0 model	42
5.2.3	MDT90 model	44
5.2.4	MDC90 model	44
5.2.5	Difference in material properties between UD- and MD-coupons	45
5.3	Conclusion	46
6	Component model	47
6.1	Introduction	47
6.2	Part 1: Buckling model	47
6.2.1	Material	47
6.2.2	Buckling test set-up	48
6.2.3	Test-results	48
6.3	Finite element model	49
6.3.1	LBA	50
6.3.2	Boundary conditions	50
6.4	Numerical results	51
6.4.1	End-shortening and deflection graphs for series 1	51
6.4.2	End-shortening and deflection graphs for series 2	53
6.4.3	Numerical agreement with experimental results	55
6.5	Part 2: Initial imperfections	56
6.5.1	Model properties	56
6.5.2	Geometry and boundary conditions	57
6.5.3	Initial imperfection	58
6.6	Numerical results	58
6.6.1	Buckling curve	58
6.6.2	Design code	60
6.6.3	Influence of initial imperfection size	60
6.6.4	Influence of boundary conditions	61
6.6.5	Failure modes	62
6.7	Conclusion	65
7	Conclusion & recommendation	66
7.1	Conclusion	66
7.2	Recommendation	67
	References	69
A	Damage variables one-element model	72
A.1	Conventional shell element results	72
A.1.1	Damage variables	72
A.2	Continuum shell element results	74
A.2.1	Damage variables	74

B	Continuum shell model with cohesive zone modelling	76
C	Classical Laminate Theory	78
D	Stress-displacement buckling models	82
D.1	Simply supported boundary conditions	82
D.2	Clamped boundary conditions	84

List of Figures

2.1	Stress-strain behaviour of FRP materials compared to steel Prince-Lund Engineering (2011)	5
2.2	Reference axis for an uni-directional ply (CUR Recommendation 96, 2017)	5
2.3	Overview of a material from constituents to structure (Sungkha777, 2016)	6
2.4	Failure modes of a fractured GFRP composite (Beura et al., 2018)	7
2.5	Examples of types of damage in FRP (Unnthorsson and Runarsson, 2020)	9
2.6	A fibre, the interface between the fibres and the matrix, and the matrix Kalveram (2015)	10
2.7	Relation between fibre orientation and different failure modes Gunes (2013)	10
2.8	Equivalent stress versus equivalent displacement for each of the failure modes	14
2.9	The damage variable as a function of the equivalent displacement	14
2.10	An element can be treated as a continuous folded plate which can be modelled as an assembly of individual plates (Landolfo, 2008)	15
2.11	For loading below the critical buckling load, a perfect plate remains flat (a), but when the load reaches the critical buckling load, the plate buckles (b) and experiences out-of-plane deformation (c) (Helbig et al., 2016)	15
2.12	Buckling of a square plate with initial imperfections (Kaskovits, 2018)	16
3.1	Conventional shell model	21
3.2	Continuum shell model	21
3.3	Difference between a conventional shell and continuum shell model (Systèmes, 2011)	22
3.4	Schematization of the four different loading directions	22
3.5	Stress-displacement comparison of the analytical results (Eq.) and the numerical output of the Abaqus/Standard conventional shell element model (FEM) for an element of 1.0 by 1.0 mm for each of the four failure modes	24
3.6	Numerical determined stress-displacement curves for the four failure modes with an element size of 1.0 by 1.0 mm, 2.0 by 2.0 mm and the maximum characteristic element size. For figure d, the maximum characteristic element size equals 2.0 by 2.0 mm.	25
3.7	Numerical determined stress-strain curves for the four failure modes with an element size of 1.0 by 1.0 mm, 2.0 by 2.0 mm and the maximum characteristic element size. For figure d, the maximum characteristic element size equals 2.0 by 2.0 mm.	25
3.8	Numerical results for the stress-displacement behaviour of the four failure modes	26
3.9	Stress-displacement comparison of the analytical results (Eq.) and the numerical output of the Abaqus/Standard continuum shell element model (FEM) for an element of 1.0 by 1.0 mm for each of the four failure modes	27
4.1	Coupon geometry for 0° tensile testing (ISO527-5 type A)	28
4.2	Coupon geometry for 90° tensile testing (ISO527-5 type B)	28
4.3	Coupon geometry for 0° compressive testing (ISO14126)	29
4.4	Coupon geometry for 90° compressive testing (ISO14126)	29
4.5	Geometry for the models loaded in tension	29
4.6	Geometry for the models loaded in compression	29
4.7	Mesh size of 1.0 by 1.0 mm for tension models	30
4.8	Mesh size of 1.0 by 1.0 for compression models	30
4.9	Experimental results for 0° tensile model (UDT0)	30
4.10	Experimental results for 90° tensile model (UDT90)	30
4.11	Experimental results for 0° compression mode (UDC0)	31
4.12	Experimental results for 90° compression model (UDC90)	31
4.13	UDT0 stress-strain curve for different fracture energy values and element size of 1.00 mm	32

4.14	UDT0 stress-strain curve with different fracture energy values and element size of 2.50 mm	32
4.15	UDT0 stress-strain curve with different fracture energy values and an element size of 1.00 mm	33
4.16	Relation between the fracture energy input and area under the stress-strain curve	33
4.17	UDT90 stress-strain curve with different fracture energy values and an element size of 1.00 mm	34
4.18	UDT90 stress-strain curve with different fracture energy values and an element size of 2.50 mm	34
4.19	UDC0 stress-strain curve with different fracture energy values and element size of 1.00 mm	35
4.20	UDC0 stress-strain curve with different fracture energy values and element size of 2.50 mm	35
4.21	UDC90 stress-strain curve with different fracture energy values and element size of 1.00 mm	36
4.22	UDC90 stress-strain curve with different fracture energy values and element size of 2.50 mm	36
4.23	UDT0 stress-strain curve with fracture energy values below the lower bound value and an element size of 1.00 mm	36
4.24	Different fracture energy values result in the same stress-strain curves before coefficient is updated	36
4.25	Stress-strain curves of an UDT0 plate with element size of 5.00 mm	37
4.26	Stress-strain curves of an UDT0 plate with element size of 25.00 mm	37
4.27	Fracture energy lower bound values (input) versus the area under the curve (output)	37
4.28	Mesh size of 25.00 by 25.00 mm for tension models	38
4.29	Mesh size of 25.00 by 25.00 for compression models	38
4.30	Stress-strain curve UDT0 for fracture energy related to the lower bound value	38
4.31	Stress-strain curve UDT90 for different fracture energy values	38
4.32	Stress-strain curve UDC0 for fracture energy related to the lower bound value	38
4.33	Stress-strain curve UDC90 for different fracture energy values	38
5.1	Lay-up of the multi-directional laminate	40
5.2	Coupon geometry for 0° and 90° tensile testing (ISO527-4 type 3)	41
5.3	Coupon geometry for 0° and 90° compressive testing (ISO14126 type B2)	41
5.4	Geometry of the model for tensile loading	41
5.5	Geometry of the model for compressive loading	41
5.6	Stress-strain curves for the test results from the MDT0-coupon tests and their average value	43
5.7	Stress-strain curves of the numerical results for the MDT0-coupon	43
5.8	Stress-strain curves for the test results from the MDT90-coupon tests and their average value	44
5.9	Stress-strain curves of the numerical results for the MDT90-coupon	44
5.10	Stress-strain curves for the test results from the MDC90-coupon tests and their average value	45
5.11	Stress-strain curves of the numerical results for the MDT90-coupon	45
6.1	The front side (left) and the back side (right) of a plate specimen installed in the test rig, ready for testing (Hayman et al., 2011)	49
6.2	Lay-up for series 1 with a thickness of 9.7 mm (left) and lay-up for series 2 with a thickness of 15.14 mm (right)	49
6.3	Shape of the geometric imperfection	50
6.4	Schematization of the test rig (Hayman et al., 2011)	50
6.5	Schematic view of the six degrees of freedom	50
6.6	Boundary conditions for 'CC/CC'	50
6.7	Boundary conditions for 'CC/CC, U2=free'	51
6.8	Boundary conditions for 'CC/SS, U2=free'	51

6.9	Boundary conditions for 'CC/SS'	51
6.10	Boundary conditions for 'SS/SS'	51
6.11	Stress-end shortening curves for series 1 with zero imperfection	51
6.12	Stress-central deflection curves for series 1 with zero imperfection	51
6.13	Stress-end shortening curves for series 1 with imperfection size B/100	52
6.14	Stress-central deflection curves for series 1 with imperfection size B/100	52
6.15	Stress-end shortening curves for series 1 with imperfection size B/33	52
6.16	Stress-central deflection curves for series 1 with imperfection size B/33	52
6.17	Stress-end shortening curves for series 2 with zero imperfection	53
6.18	Stress-central deflection curves for series 2 with zero imperfection	53
6.19	Stress-end shortening curves for series 2 with imperfection size B/100	54
6.20	Stress-central deflection curves for series 2 with imperfection size B/100	54
6.21	Stress-end shortening curves for series 2 with imperfection size B/33	54
6.22	Stress-central deflection curves for series 2 with imperfection size B/33	54
6.23	Dimensions of the plate	57
6.24	Schematic view of the six degrees of freedom	57
6.25	Simply supported boundary conditions	57
6.26	Clamped boundary conditions	57
6.27	Shape of the geometric imperfection for the simply supported model	58
6.28	Shape of the geometric imperfection for the clamped model	58
6.29	Buckling curve for different initial imperfections with clamped boundary conditions	59
6.30	Buckling curve for different initial imperfections with simply supported boundary conditions	59
6.31	Difference in reduction factor between B/1000 and B/125 for simply supported [SS] and clamped [CC] boundary conditions	60
6.32	Reduction factor comparison for both types of boundary conditions and initial imperfection of B/1000	61
6.33	Reduction factor comparison for both types of boundary conditions and initial imperfection of B/125	61
6.34	Force-displacement curve for plate thickness of 13.76 mm, $\lambda = 1.21$, initial imperfection size of B/1000 and clamped boundary conditions	62
6.35	Force-displacement curve for plate thickness of 13.76 mm, $\lambda = 1.21$, initial imperfection size of B/125 and clamped boundary conditions	62
6.36	Force-displacement curve for plate thickness of 20.64 mm, $\lambda = 1.14$, initial imperfection size of B/1000 and simply supported boundary conditions	62
6.37	Force-displacement curve for plate thickness of 20.64 mm, $\lambda = 1.14$, initial imperfection size of B/125 and simply supported boundary conditions	62
6.38	Clamped BC and initial imperfection of B/1000 - First failure mode: matrix in compression	63
6.39	Clamped BC and initial imperfection of B/1000 - Second failure mode: matrix in tension	63
6.40	Clamped BC and initial imperfection of B/1000 - Third failure mode: fibres in compression	63
6.41	Clamped BC and initial imperfection of B/1000 - Fourth failure mode: fibres in tension	63
6.42	Clamped BC and initial imperfection of B/125 - First failure mode: matrix in tension	63
6.43	Clamped BC and initial imperfection of B/125 - Second failure mode: matrix in compression	63
6.44	Clamped BC and initial imperfection of B/125 - Third failure mode: fibres in compression	63
6.45	Clamped BC and initial imperfection of B/125 - Fourth failure mode: fibres in tension	63
6.46	Simply supported BC and initial imperfection of B/1000 - First failure mode: matrix in compression	64
6.47	Simply supported BC and initial imperfection of B/1000 - Second failure mode: matrix in tension	64
6.48	Simply supported BC and initial imperfection of B/1000 - Third failure mode: fibres in compression	64
6.49	Simply supported BC and initial imperfection of B/1000 - No failure of fibres in tension	64
6.50	Simply supported BC and initial imperfection of B/125 - First failure mode: matrix in tension	64
6.51	Simply supported BC and initial imperfection of B/125 - Second failure mode: matrix in compression	64
6.52	Simply supported BC and initial imperfection of B/125 - Third failure mode: fibres in compression	64

6.53 Simply supported BC and initial imperfection of B/125 - No failure of fibres in tension . . .	64
A.1 Applied displacement for the conventional shell models of 1.0 by 1.0 millimetres for each of the four loading directions	72
A.2 The four damage variables for the conventional shell model loaded in tension in fibre directions	72
A.3 The four damage variables for the conventional shell model loaded in tension in fibre directions	73
A.4 The four damage variables for the conventional shell model loaded in tension in fibre directions	73
A.5 The four damage variables for the conventional shell model loaded in tension in fibre directions	73
A.6 The continuum shell model for each of the four loading directions in the displaced situation	74
A.7 The four damage variables for the continuum shell model loaded in tension in fibre directions	74
A.8 The four damage variables for the continuum shell model loaded in tension in fibre directions	74
A.9 The four damage variables for the continuum shell model loaded in tension in fibre directions	75
A.10 The four damage variables for the continuum shell model loaded in tension in fibre directions	75
B.1 Stacked shell method: (a) laminate cross-section, (b) laminate split in plies, (c) shell model of sub-laminates, (d) stacked shells with CZM (Pearce et al., 2014)	76
B.2 Boundary conditions	77
B.3 SC8R elements with a length of 0.43 millimetre	77
B.4 Stress-strain curve continuum shell model with cohesive zone modelling	77
C.1 Critical buckling load for a plate with clamped boundary conditions (<i>CC</i>) and simply supported boundary conditions (<i>SS</i>)	80
D.1 Stress-displacement curve for laminate thickness 6.88 mm	82
D.2 Stress-displacement curve for laminate thickness 10.40 mm	82
D.3 Stress-displacement curve for laminate thickness 13.76 mm	82
D.4 Stress-displacement curve for laminate thickness 16.00 mm	82
D.5 Stress-displacement curve for laminate thickness 20.64 mm	83
D.6 Stress-displacement curve for laminate thickness 24.00 mm	83
D.7 Stress-displacement curve for laminate thickness 27.52 mm	83
D.8 Stress-displacement curve for laminate thickness 32.00 mm	83
D.9 Stress-displacement curve for laminate thickness 34.40 mm	83
D.10 Stress-displacement curve for laminate thickness 41.28 mm	83
D.11 Stress-displacement curve for laminate thickness 48.00 mm	83
D.12 Stress-displacement curve for laminate thickness 6.88 mm	84
D.13 Stress-displacement curve for laminate thickness 10.40 mm	84
D.14 Stress-displacement curve for laminate thickness 13.76 mm	84
D.15 Stress-displacement curve for laminate thickness 16.00 mm	84
D.16 Stress-displacement curve for laminate thickness 20.64 mm	84
D.17 Stress-displacement curve for laminate thickness 24.00 mm	84
D.18 Stress-displacement curve for laminate thickness 27.52 mm	85
D.19 Stress-displacement curve for laminate thickness 32.00 mm	85
D.20 Stress-displacement curve for laminate thickness 34.40 mm	85
D.21 Stress-displacement curve for laminate thickness 41.28 mm	85
D.22 Stress-displacement curve for laminate thickness 48.00 mm	85

List of Tables

2.1	Overview of fracture energy values found in literature for pultruded GFRP laminates . . .	14
3.1	Material properties for the four failure modes	23
3.2	Input values for the engineering constants	23
4.1	Geometry and material properties of the four different models	31
4.2	UDT0: difference between the lower bound fracture energy (input) and numerical stress-strain area (output)	32
4.3	UDT90: difference between the lower bound fracture energy (input) and numerical stress-strain area (output)	34
4.4	UDC0: difference between the lower bound fracture energy (input) and numerical stress-strain area (output)	35
4.5	UDC90: difference between the lower bound fracture energy (input) and numerical stress-strain area (output)	35
5.1	Material properties of the UD-models	42
5.2	Material properties of the MD-models	42
5.3	Original (UD-values) and updated material properties (MD-values) for MDT0-coupon model	43
5.4	Original (UD-values) and updated material properties (MD-values) for MDT90-coupon model	44
5.5	Original (UD-values) and updated material properties (MD-values) for MDC90-coupon model	45
5.6	Strength and stiffness difference between UD-coupons and MD-coupons	45
6.1	Average material properties from NTUA test and DTU test	48
6.2	Ultimate failure load for each plate	49
6.3	Material properties for the component model, including the lower bound fracture energy value and the lower bound fracture energy value increased by 10%	50
6.4	Series 1, no imperfection: maximum stress, in-plane displacement and out-of-plane displacement difference between the test results and the Abaqus/Standard model for the five different boundary conditions.	52
6.5	Series 1, imperfection size B/100: maximum stress, in-plane displacement and out-of-plane displacement difference between the test results and the Abaqus/Standard model for the five different boundary conditions.	53
6.6	Series 1, imperfection size B/33: maximum stress, in-plane displacement and out-of-plane displacement difference between the test results and the Abaqus/Standard model for the five different boundary conditions.	53
6.7	Series 2, no imperfection: maximum stress, in-plane displacement and out-of-plane displacement difference between the test results and the Abaqus/Standard model for the five different boundary conditions.	54
6.8	Series 2, imperfection size B/100: maximum stress, in-plane displacement and out-of-plane displacement difference between the test results and the Abaqus/Standard model for the five different boundary conditions.	55
6.9	Series 2, imperfection size B/33: maximum stress, in-plane displacement and out-of-plane displacement difference between the test results and the Abaqus/Standard model for the five different boundary conditions.	55
6.10	Average difference in ultimate strength, in-plane displacement and out-of-plane displacement for all six situations	55

6.11 Overview of which type of boundary conditions approximates the test result the closest, for each of the six models	56
6.12 Material properties of the GFRP plate	57
6.13 Model properties for the fracture energy	57
6.14 Numerical results for the critical stress, relative slenderness and reduction factor for the different plate thickness, varying initial imperfection sizes and two types of boundary conditions	59
6.15 Difference in reduction factor for initial imperfection B/1000 and B/125 for clamped boundary conditions	61
6.16 Difference in reduction factor for initial imperfection B/1000 and B/125 for simply supported boundary conditions	61
B.1 Surface-to-surface properties \citep{Lieuwe}	76
C.1 Material properties and buckling coefficients	79
C.2 Numerical and analytical determined critical buckling load and their difference for varying plate thickness with two types of boundary conditions	81

List of Symbols

Uppercase

Symbol	Description	Unit
A	cross-sectional area of a plate	mm ²
D	damage parameter	-
D_{ij}	bending stiffness matrix with element on row 'i' and column 'j'	Nmm
E_1	longitudinal Young's modulus	MPa
E_2	transverse Young's modulus	MPa
G	shear modulus	MPa
G_c	fracture energy	MPa
F_{ij}, F_i	parameters related to the lamina strength in principal direction	-
I_{min}	minimum value of the moment of inertia	mm ⁴
L_0	buckling length of the member	mm
L_c	characteristic length	mm
M	damage operator	-
N_{cr}	critical buckling load	N
N_{Eul}	Eulerian critical load	N
$N_{loc,Rd}$	design value for the compressive force	N
$N_{Rd2,c}$	design force for buckling strength	N
S_6	shear strength in the 12-plane	MPa
X^C	compressive strength in the fibre direction	MPa
X^T	tensile strength in the fibre direction	MPa
Y^C	compressive strength perpendicular to the fibres	MPa
Y^T	tensile strength perpendicular to the fibres	MPa

Lowercase

Symbol	Description	Unit
b	plate width	mm
b_w	width of the web of an I-profile	mm
c	numerical coefficient related to the buckling reduction factor χ	-
d_f	internal damage variable for fibre damage	-
d_m	internal damage variable for matrix damage	-
d_s	internal damage variable for shear damage	-
$f_{c,k}$	characteristic compressive strength	MPa
$f_{c,stab,k}$	critical buckling stress	MPa
p, q	constants related to the critical buckling stress	-
t	plate thickness	mm
t_w	thickness of the web of an I-profile	mm
v_f	fibre volume fraction	%

Greek

Symbol	Description	Unit
α	imperfection factor for plate buckling	-
γ_M	partial material safety factor for buckling resistance	-
δ_{eq}	equivalent displacement	mm
$\dot{\epsilon}$	true strain rate	-
η_c	conversion factor	-
λ	relative slenderness	-
$\tilde{\lambda}_{f,0}$	buckling curve plateau length	-
ν	Poisson's ratio	-
ξ	coefficient of restraint related to critical buckling stress	-
ρ	reduction factor for local wrinkling and imperfections	-
σ	nominal stress	MPa
$\hat{\sigma}$	effective stress tensor	MPa
$\sigma_{cr,c}$	critical stress	MPa
σ_{eq}	equivalent stress	MPa
σ_{ij}	true stress tensor components	MPa
Φ	factor for the determination of reduction factor χ	-
χ	reduction factor for the interaction between local and global buckling	-

Math

Symbol	Description	Unit
\mathbb{C}	damaged elasticity matrix	MPa
$\langle \rangle$	Macaulay bracket operator	-

List of Abbreviations

Abbreviation	Definition
CC	compact compression
CF	fibres in compression
CM	matrix in compression
CT	compact tension
CZM	cohesive zone model
DIC	digital image correlation
DTU	Technical University of Denmark
FEM	finite element method
FRP	fibre-reinforced polymers
GFRP	glass fibre reinforced polymers
MARSTRUCT	Network of Excellence on Marine Structures
MD	multi-directional
NTUA	National Technical University of Athens
TF	fibres in tension
TM	matrix in tension
UD	uni-directional

Introduction

1.1. Introduction

In the past few decades, fibre reinforced polymer (FRP) increased rapidly in popularity. It is a composite material consisting of a polymer resin combined with reinforcing fibres. The material's advantageous properties, such as a high strength-to-weight ratio and low required maintenance, gave rise to its popularity in multiple major engineering branches. One of the main benefits of the material is the option to combine different types of fibres and resin, which gives the designer the possibility to achieve optimal and case-specific objectives and properties. FRP composites have not only been incorporated in new constructions but also for the renovation of existing structures. They are an enhancement or substitute for infrastructure components or systems traditionally constructed from steel or concrete. The enhanced structural performance of FRP composite materials improves innovation, increases productivity, and extends the service life. Applications in the civil industry include bridge decks, formwork, modular structures, and external reinforcement. Additional advantages of the material are a high stiffness-to-strength ratio and low density of the material. As with all materials, there are also disadvantages to using FRP composites: high material costs, a short history of applications, and gaps in the development of established standards.

Due to the relatively recent interest in this type of material, there is a lack of research and, the design codes are still a work in progress compared to more traditional materials as steel and concrete. Design safety requires that design procedures identify and account for all possible failure modes and mechanisms. One of the major concerns for building with FRP is its brittle failure behaviour. The ability to undergo inelastic deformation before failure is an important safeguard against structural engineering failures, and FRP does not exhibit this behaviour. A characterisation of the respective failure modes and preventive measures are needed to develop all-inclusive design standards to continue the rise of FRP as a construction material in structural engineering applications. Current FRP design standards are primarily based on a small set of experimental data of pultruded profiles. Research has focused on the automotive and aircraft industries, and materials more commonly used in the civil sector have been less investigated. Glass fibre reinforced polymers (GFRP) are often used in the infrastructure and building industry.

Buckling, specifically local buckling, is an important issue that needs to be considered when FRP structures are analysed due to the notably low stiffness-to-strength ratio of thin laminates. Besides, the manufacturing process allows for the occurrence of initial imperfections in the material. In combination with the usual high slenderness of FRP, these imperfections make the material susceptible to buckling. For plates made from steel or aluminium, buckling curves have been established that express the strength of the material under in-plane compressive loading as a function of a slenderness parameter. These buckling curves take into account geometric imperfections and are created from extensive numerical, analytical, and experimental studies.

For FRP structures, buckling design is performed in terms of the elastic critical load of an ideal structure combined with a reducing factor based on limited test data. Design codes do not take the influence of initial imperfections into account but mainly focus on the interaction between webs and flanges. Steps have been made to create a Eurocode buckling verification similar to that for steel structures, however, more research is needed to reach such a design format.

Damage to a material will degrade the material properties and eventually lead to failure. Continuum damage mechanics with progressive failure analysis is used to predict this degrading process of a material. For FRP materials, Abaqus/Standard has implemented, by default, the Hashin damage criteria to characterise the damage onset and evolution. These criteria are based on the fracture energy of the material. The assessment of fracture energy properties in composite materials is challenging due to specimen geometry and fibre lay-up, and accurate data of GFRP fracture energy is largely unknown. This report provides numerical research with progressive failure analysis into the non-linear buckling behaviour of a GFRP laminate.

1.2. Scope

This report investigates the non-linear buckling behaviour of a GFRP laminate. Progressive failure analysis is performed based on the Hashin damage criteria. Due to a lack of post-failure data, the lower bound fracture energy is implemented in the model. The focus is on the degradation of the material's mechanical properties rather than micromechanical damage mechanisms.

Attention is given to glass fibre reinforced polymers due to their advantageous properties for application in the civil industry combined with the lack of research data. The laminate used in this study consists of multiple sub-laminates with the following lay-up: $[90/0_3/45/-45/0_2]_S$. This equals a distribution of 62.5% fibres with 0° orientation and 12.5% fibres in the 90° , -45° and $+45^\circ$ orientation each.

The initial imperfections and thickness of the plate are varied to quantify the strength reduction due to geometric imperfections and to create a buckling curve for this specific GFRP laminate. Two types of boundary conditions are applied to validate if the choice of boundary conditions influences the numerical determined load-carrying capacity of the laminate. The numerical results are compared with the current design standards.

1.3. Problem statement

The main problem statement of this research is:

How to predict the non-linear buckling behaviour of a GFRP plate with progressive failure analysis?

The following questions are addressed to reach the primary goal:

1. Can lower bound fracture energy be used for progressive failure analysis for determining non-linear buckling behaviour?
2. What is the influence of initial imperfections on the buckling strength of a GFRP plate?
3. Do the boundary conditions of the numerical model influence the buckling curve of a GFRP plate?

1.4. Aim and objective

For the safe design of Glass Fibre Reinforced Polymer structures, design standards related to FRP plates' stability that account for the influence of initial imperfections on damage behaviour require improvement. This thesis aims to provide a numerical approach to predict the non-linear buckling behaviour of a GFRP laminate. With this aim, the following objectives are defined:

- Part 1: State-of-the-art
 - 1 a) Research static failure mechanisms in FRP composites
 - 1 b) Describe the criteria for the Hashin damage model
- Part 2: Numerical validation
 - 2 a) One-element model
 - Build a one-element model based on fracture energy values found in research and confirm the relationship between the fracture energy and element size
 - 2 b) Uni-directional coupon model
 - Create a finite element analysis of uni-directional coupon tests to obtain the material properties and lower bound fracture energy values
 - 2 c) Multi-directional model
 - Construct a finite element model of multi-directional coupon tests and validate implementation of the lower bound fracture energy for progressive failure analysis
- Part 3: Parametric study
 - 3 a) Component model part 1
 - Recreate experimental buckling tests found in the literature to validate implementation of the lower bound fracture energy for non-linear buckling analysis
 - 3 b) Component model part 2
 - Create a buckling curve for a GFRP plate by varying the plate thickness. Analyse the strength reduction due to initial imperfections and verify if the reduction factor for the buckling strength of the plate depends on the boundary conditions of the numerical model.

1.5. Methodology

The research structure is divided into three parts: a literature study, a numerical validation and a parametric study. In the first part, valuable information about fibre reinforced polymer materials and their general damage behaviour is obtained to understand how to model damage of anisotropic materials.

In the second part, multiple finite element models are created to validate the use of the lower bound fracture energy. The first model consists of one element to understand the mesh dependency of the fracture energy. The next step is to create a numerical model based on the results from previously performed experimental coupon tests, described in the report "Pin Bearing in Glass Fiber-Reinforced Polyester" by Lieuwe Cornelissen ([Cornelissen, 2020](#)). Uni-directional coupon tests are used to obtain the material properties and lower bound fracture energy of the material. Multi-directional coupon tests are modelled to validate the lower bound fracture energy implementation for progressive failure analysis.

The third part of this report, a parametric study, consists of two sections. Experimental buckling tests reported in "Buckling of Imperfect Composite Plates: Parametric Studies" by K. Misirlis et al. ([Hayman et al., 2011](#)) are recreated to validate the use of the lower bound fracture energy for non-linear buckling behaviour. In the second part, a buckling curve is created to study the non-linear buckling behaviour of the GFRP plate. From this, the influence of initial imperfections on the reduction of the buckling strength is analysed and if the boundary conditions of the numerical model influence the buckling curve values.

2

Literature review

This chapter aims to give the reader general background information about fibre reinforced polymers. A description of the material's failure mechanisms is given and how the damage criteria for the numerical prediction of failure can be defined. It explains why it is essential to design against buckling and the current state regarding the design codes for buckling design.

2.1. Introduction

Fibre-reinforced polymer (FRP) is a composite material consisting of fibres and resin with the possible addition of cores and additives. The composites are natural or human-made, consisting of two or more constituent materials with significantly diverse physical or chemical properties, which remain distinctive in the combined product. Most composites consist of strong and stiff fibres surrounded by a weaker matrix that keeps the fibres in place. The fibres have a load-bearing function in the direction of their orientation and provide stiffness to the material. The resin fixates the fibres in place, transfers the forces, prevents buckling of the fibres, provides fibre protection, and increases the material's damage tolerance.

The material properties depend on the properties of the fibres and resin, the volume fraction, V_f , and the orientation of the fibres. The different types of fibres and resin combined with the ability to vary the fibres' direction results in a material with a wide range of material properties; it gives the designer freedom to design the most suitable material for each job. On the downside, it does create a more difficult task in determining the true material properties and choosing the correct design regulations. In this paper, reference is made to material tests performed with E-glass fibres and an unsaturated polyester resin.

2.1.1. Fibres

The most common materials used for the fibres are carbon, aramid and glass fibres. Carbon fibres have the highest strength, stiffness and best fatigue performance. Figure 2.1 shows the strength comparison of carbon fibres compared to other materials. Due to the considerable interest in carbon fibres from the aerospace and automotive industry, extensive research has been performed on those fibres. Aramid fibres can undergo plastic deformation in compression and ductile fracture in tension, and they have extraordinary wear resistance. The high quality of those two types of fibres comes with a higher price compared to glass fibres. Glass fibres are most widely used due to their affordability, good chemical resistance, high tensile strength and impact resistance. The fatigue performance and stiffness are lower than those of carbon fibres. Compared to aramid fibres, glass fibres are more susceptible to humidity and alkaline attack. However, their affordability makes them the most popular type of fibre. The most used glass fibres are E-glass and S-glass. Glass fibres are abrasive and need sizing to prevent damage to their neighbouring fibres. Sizing consists of applying a film former and a coupling agent to the fibres. The coupling agent enhances the fibre-matrix bond; without it, the hydrophilic nature of the glass fibres and hydrophobic properties of the matrix creates a relatively weak bond. The sizing influences the composite materials mechanical properties (Al-Moussawi et al., 1993).

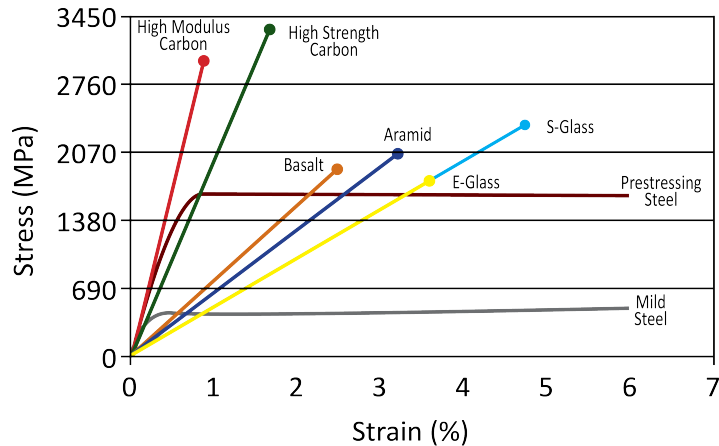


Figure 2.1: Stress-strain behaviour of FRP materials compared to steel [Prince-Lund Engineering \(2011\)](#)

2.1.2. Resin

The polymer resin provides the matrix that surrounds the fibres. Besides the resin's previously mentioned functions, it provides toughness, damage tolerance, impact- and abrasion-resistance. A resin converts into a rigid polymer by curing. Two types of polymers can be distinguished in FRP materials: thermoplastic and thermoset. A thermoplastic polymer softens when heated, while thermoset polymers create cross-links between the molecules and are converted into a rigid structure. They only soften when the glass transition temperature is reached. This temperature differs per resin and affects the stiffness, compressive strength, tensile strength and water resistance ([Ebnesajjad, 2016](#)). Types of resins typically used in FRP materials include epoxy, vinyl ester, polyester thermosetting plastic or phenol-formaldehyde. The most commonly used type of resin for civil engineering is polyester. It consists of a polyester solution in a monomer, usually styrene. The addition of styrene plays an essential role in forming cross-links between the polymer molecules, and it reduces the viscosity of the resin, which makes it easier to handle.

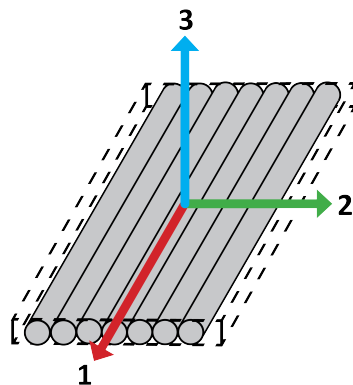


Figure 2.2: Reference axis for an uni-directional ply ([CUR Recommendation 96, 2017](#))

2.2. Material properties

Fibre-reinforced composites are formed by high strength fibres placed in a polymer matrix with distinct interfaces in between. Both the fibres and the resin keep their physical and chemical identities, but their combined properties create a material that cannot be achieved by one of the constituents alone. An FRP laminate has multiple failure mechanisms which depend on the loading direction of the ply. In uni-directional (UD) plies, the reference axis is defined as follows and demonstrated in figure 2.2:

- 1-direction is the axial direction of the fibres;

- 2-direction is the in-plane transverse direction;
- 3-direction is the out-of-plane direction.

For a UD ply, the material's maximum strength and stiffness are reached in the direction of the fibres. When multiple thin layers of uni-directional plies are stacked together, a laminate is created, which is the most common form of composites for structural applications (Uddin, 2013). An overview of the material from the constituents to a structure is depicted in figure 2.3.

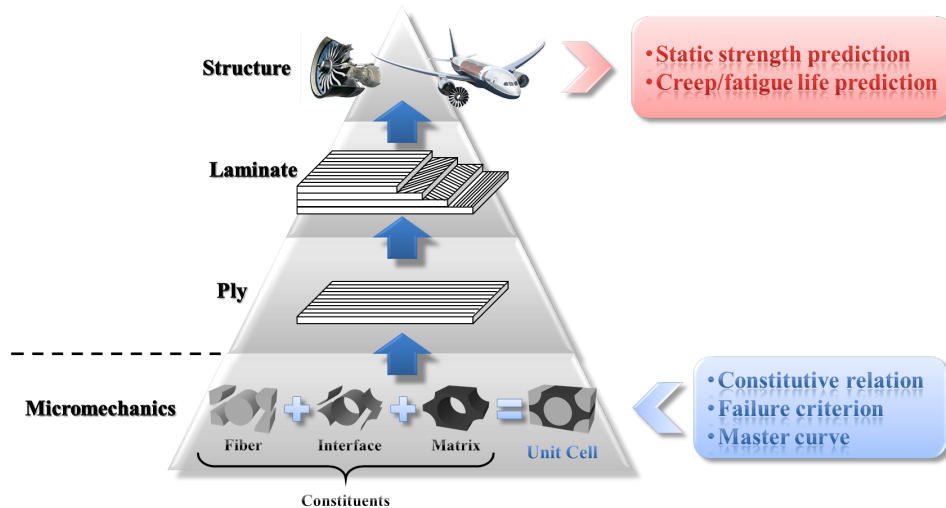


Figure 2.3: Overview of a material from constituents to structure (Sungkha777, 2016)

Varying the direction of the fibres in the stacked laminae gives the material its isotropic properties. The fibres' orientation determines the strength and resistance to deformation of the polymer. Glass polymer fibres parallel to the applied force are the strongest and most resistant compared to fibres in other directions, with fibres in perpendicular direction performing the weakest. The polymer's strength and elasticity are less than that of the matrix when the force is perpendicular to the fibre orientation. The highest stiffness and strength of a laminate occurs if all the fibres are parallel to the loading direction. Such a lay-up is good for resisting axial loading. However, this could also lead to issues during transportation and installation or with load transfer near connections. Fibres in other directions are added to the material to prevent these issues. Fibres can be oriented in two- or three-dimensional constructs. Forces perpendicular to one of the directions will be parallel to fibres in another orientation; weak spots can consequently be eliminated. Perpendicular fibres are a good use for natural hinges and connections. However, an increase in specific properties in the matrix direction decreases the properties in the fibre direction. The choice of an FRP laminate stacking sequence allows for optimising their strength, stiffness, and weight to meet the desired design requirements.

2.2.1. Determination of material properties from coupon tests

Thorough knowledge of the materials' failure modes and mechanisms is needed to design with FRP materials safely. Comprehensive experimental and modelling research needs to be performed to obtain insight into the general and application-specific failure types of structural FRP systems. The laminates' characteristic properties which influence the material's behaviour include Young's modulus, failure strain, and ultimate strength. Different methods are available to obtain these properties. A commonly used method is the flat coupon test, described in ASTM D3039 (2017), due to its ease of testing and interpreting test results. For this test, a specimen of the material is taken and undergoes uni-axial tension, uniaxial compression and shear tests to obtain the parameters related to the kinetic equations. FRP composites behave almost as a linear elastic brittle material. The initiation of fracture occurs when the rupture strain of the fibres is reached. If the strain distribution in a test sample is non-uniform, a lower average rupture strain will be reached. Material testing aims to obtain true material properties, which should be insensitive to the setup. The safety of an FRP structure is obtained by using safety margins on many factors, such as the geometrical- and loading conditions and the material properties.

2.3. Failure behaviour

FRP has three distinct damage mechanisms: damage to the matrix, damage to the fibres or damage to the interface between the matrix and the fibres. These mechanisms relate to the FRP constituents that provide the strength and stiffness: the fibres, the polymer matrix, and the interface in-between. Figure 2.6 illustrates these three constituents. The interface allows for both the fibres and the matrix to retain their physical and chemical identities, even though one of the constituents alone cannot obtain the properties of the composite material (Gunes, 2013). The anisotropic properties of the material generate four different failure modes. The material has the highest strength when the loading is in line with the fibre direction. Figure 2.7 shows the failure modes of a uni-directional laminate loaded in different directions. The normalised strength, corresponding with the tensile strength, decreases for a deviation of the loading direction. Loading in the direction of the fibres leads to fibres failing in tension or compression. Transverse tensile and transverse compressive failure occurs from loading perpendicular to the fibre direction. From loading not parallel or perpendicular to the fibres, shear failure can develop. Four failure modes for FRP composites are defined from the relation between the fibre orientation and type of failure:

- fibre rupture in tension;
- fibre buckling and kinking in compression;
- matrix failure under transverse tension and shear:
- matrix failure under transverse compression and shear.

Failure patterns in composite structures are more complicated compared to isotropic materials. Structural failure can originate from intra-laminar failure modes, including matrix failure, fibre breakage and fibre matrix debonding, or from an inter-laminar failure mode, such as delamination (Ubaid et al., 2014). The finite element method (FEM) with progressive failure analysis can model failure accumulation and propagation. When a composite material is subjected to loading, the load will travel through the matrix, and via the interface, to the fibres (Kuldeep Agarwal et al., 2018). The material generally passes four stages before failure:

1. Fibers and matrix deform linear elastic;
2. Matrix behaves non-linear;
3. Fibers and matrix behave non-linear;
4. Failure is initiated.

Although FRP materials have some very favourable properties, their brittle failure behaviour is a significant concern for structural engineers. Figure 2.1 shows that fibres loaded in the normal direction have a linear elastic stress-strain behaviour followed by brittle failure. In structural engineering, the ability to undergo inelastic deformation is an essential safeguard against failure. It warns before ultimate failure occurs and reduces the dynamic load demand through increased energy dissipation and damage. Fibre-reinforced polymers are very brittle, even more brittle than concrete. A compensating property of FRP is their high ultimate strain, around 1.2% till 2.3%, compared to the 0.35% ultimate strain of concrete.

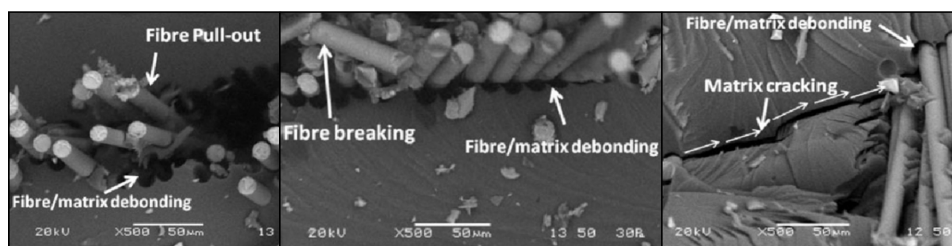


Figure 2.4: Failure modes of a fractured GFRP composite (Beura et al., 2018)

The first cracks tend to appear in the resin. This cracking of the matrix does not immediately endanger structural integrity. After cracks are formed in the resin, delamination can occur. This failure mode is characterised by a separation of the layers in the laminate. After it is initiated, the delamination will continue to grow gradually. The onset of delamination is challenging to predict; the only known is that it will not occur before cracks originate in the resin. When the laminate is subjected to tension, the first fractures occur isolated in weak zones (Maimí et al., 2007). Stress concentrations occur in the material surrounding these fractures, which leads to fibre-matrix debonding and matrix cracking. Eventually, fibre will be pulled out and the material collapses.

In the case of compressive loading, kinking of the fibres will lead to fibre failure. Due to the anisotropic characteristics and the fibres being the load-carrying component, the material is damage tolerant. It will continue to perform even when properties in one or more plies are degraded. Material behaviour after damage initiation can be predicted with progressive failure analysis. The basic concept of this analysis is that plies that undergo damage or failure will have a progressive reduction on the material stiffness matrix. To detect failure, damage initiation and damage propagation criteria are developed. When a ply reaches a failure criterion, certain material properties are reduced, and the ability of further load resistance is lowered. This process is continued until the global stiffness matrix becomes numerically unstable, which denotes total failure. A progressive failure model is based on the type of failure criteria chosen and the implemented material degradation.

2.3.1. Mechanical behaviour in fibre direction

In the fibre direction, the stresses are mainly transmitted through the fibres due to the fibres' high stiffness and strength compared to the matrix material. Transmitted tensile stresses are barely affected by damage to the matrix because the fibres straighten under tension loading. However, straightening of the fibres can contribute to damage to the matrix. When the material is compressed, the fibres' effective stress and strength are highly affected by the surrounding matrix. The matrix behaves similar to an elastic foundation for the fibres in compression (Matzenmiller et al., 1995). Tension in fibre direction can lead to rupture, while compression of the fibres can lead to buckling or kinking of said fibres. All three occurrences cause damage to the matrix. The stiffness components of the constitutive tensor for the damaged uni-directional laminae are degraded to account for this behaviour.

2.3.2. Mechanical behaviour in transverse direction

Normal stresses transverse to the fibres and shear stresses are both endured by the matrix and the fibres. Damage from these stresses occurs mainly in the matrix or the fibre-matrix interface, which leads to debonding. Compared to the other constituents, the bond strength at the interface between the fibres and the matrix generally has the lowest strength. Cracks advance from the matrix into the interface and propagate alongside the fibres without entering the fibre material. Tensile loading in the transverse direction leads to the progressive opening of existing cracks, while compression in transverse loading usually leads to crushing of the matrix material.

2.4. Damage model

Damage to a material will lead to a degradation of its stiffness and strength. This degradation reduces the load-carrying capacity and the service life of the structure. Modelling a material's damage behaviour is essential to make engineering predictions about damage initiation, crack propagation, and fracture. A damage model can be used as a prediction tool suitable for design and provide better insight into damage behaviour. Continuum damage mechanics assumes that damage accumulates within a material, reducing the effective cross-sectional area and eventually leading to rupture. It is based on the concept that cracks or defects imply a reduced capacity to withstand stresses. The rate and direction of damage propagation define the damage tolerance of a structure and the eventual collapse. For the non-linear response of quasi-brittle materials with damage accumulation, non-linear constitutive models have been developed and implemented in finite element methods. Progressive failure analysis can be used in combination with failure criteria to predict the load-carrying capacity and failure propagation.

Damage is an important aspect for many composite materials with brittle properties; it has a destabilising influence and can cause a structure to lose its stability (Akbarov, 2013). *Damage mechanisms* are the underlying processes and changes that initiate a particular failure mode from which fracture can follow. In composite materials, damage develops continuously at a micro-scale and grows from the before mentioned mechanisms: fibre breakage, fibre debonding, matrix micro-cracking and delamination. In figure 2.5 these four types of damage are illustrated. The elastic-brittle behaviour of FRP material is characterised by the formation and evolution of micro-cracks and cavities, which are surface- and volume discontinuities, respectively. These discontinuities result in a degradation of the stiffness and strength of the material (Rahimian Koloor et al., 2020). The different types of fibres and resins combined with the wide range of fibre volume ratios in composites make the study of initiation and propagation of cracks case-specific. A physical discontinuity in a material can occur from an existing flaw or its variation of properties. Damage to composites can occur during initial processing or when the material is in service. Since the complete prevention of damage is not possible, composite structures should be designed to function safely even when flaws are present in the material.

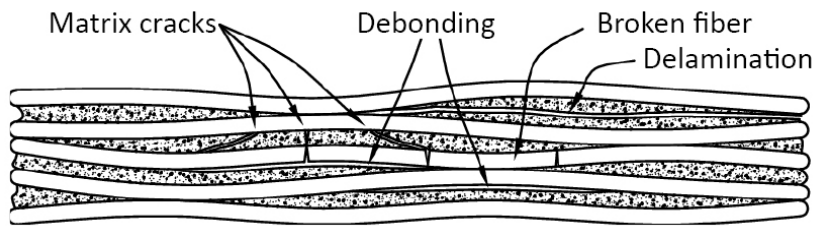


Figure 2.5: Examples of types of damage in FRP (Unnthorsson and Runarsson, 2020)

Fracture mechanics analyses the initiation and propagation of cracks through a solid body. The ultimate stage of the damage process generally responds to a material discontinuity that is relatively large compared to the material's microscopic heterogeneity. The main crack is then assumed to be developed through several layers and shows a sufficient macroscopic homogeneity in the crack's size and direction. The challenging part of understanding fracture behaviour in high-strength material is that cracks modify the local stress to an extreme, and elastic stress analysis is no longer sufficient. Kachanov (KACHANOV, 1958) proposed a macroscopic damage variable in combination with the effective stress concept. The material's microscopic deterioration, which includes voids or micro-cracks, is taken into account by the damage parameter D . It is generally accepted to use $D = 0$ for initially unstressed material and $D = 1$ at material failure.

2.4.1. Development of failure criteria

The determination of material failure from an analytical detection of micro-stress, micro-failure, and coalescence is too complicated. A way to approach failure prediction is to assume a three-dimensional failure criterion with terms consisting of macro variables (Hashin, 1980). Examples of these macro variables are the average stresses or strains, which can be determined from material tests. The problem remains with the initial yield criterion for an elastoplastic material. Tsai (Tsai et al., 1965) assumed that the failure criterion of a UD fibre is composed of the same mathematical form as the yield criterion of an orthotropic ideally plastic material, given by Hill (Hill, 1948).

$$F (\sigma_{22} - \sigma_{33})^2 + G (\sigma_{33} - \sigma_{11})^2 + H (\sigma_{11} - \sigma_{22})^2 + 2L\sigma_{23}^2 + 2M\sigma_{31}^2 + 2N\sigma_{12}^2 = 1 \quad (2.1)$$

σ_{ij} : true stress tensor components

F, G, H, L, M, N : constants that have to be determined from experiments

The one-dimensional uni-axial stresses and shear stresses in this equation can be easily determined. However, it includes the assumption that isotropic stress has no effect, which is not valid for the isotropic tension of a fibre's composite. To account for the unequal failure in tension and compression in composites, Hoffman (Hoffman, 1967) added linear stress terms. Furthermore, Tsai and Wu presented the failure criteria as a general quadratic stress equation and, by doing so, eliminating the dependence on the normal stress.

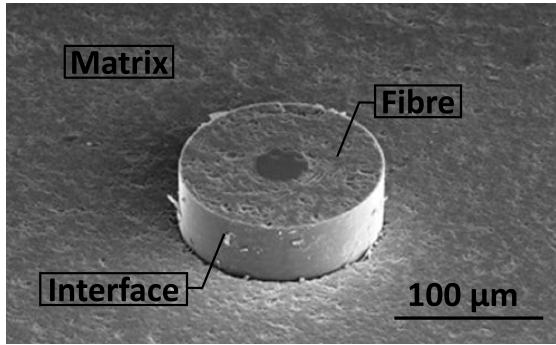


Figure 2.6: A fibre, the interface between the fibres and the matrix [Kalveram \(2015\)](#)

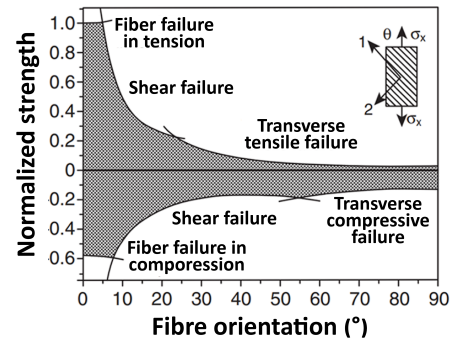


Figure 2.7: Relation between fibre orientation and different failure modes [Gunes \(2013\)](#)

$$F_{ij}\sigma_i\sigma_j + F_i\sigma_i = 1 \quad (2.2)$$

F_{ij} and F_i are parameters provided by analogous expressions that are related to the lamina strength in the principal directions, where $i, j = 1, \dots, 6$ for a 3-D case. For an orthotropic material with unequal strength in tension and compression, the strength variables are defined as follows:

$$F_{11} = \frac{1}{N_1^+ N_1^-}, F_1 = \frac{1}{N_1^+} - \frac{1}{N_1^-}, F_{66} = \frac{1}{S_6^2} \quad (2.3)$$

Tensile and compressive strength in the 1-direction is given by N_1^+ and N_1^- , respectively. The shear strength in the 12-plane is stated as S_6 . Considering that material failure is indifferent to a change of sign of the shear stress, all terms containing shear stress to the first power must disappear. For a uni-directional ply, this results in the following failure criteria:

$$F_{11}\sigma_{11}^2 + F_{22}\sigma_{22}^2 + 2F_{12}\sigma_{11}\sigma_{22} + F_{66}\sigma_{12}^2 + F_1\sigma_{11} + F_2\sigma_{22} = 1 \quad (2.4)$$

The fibre direction is x_1 and the transverse direction is x_2 . For the determination of F_{12} , a variety of bi-axial failure tests is needed: tension-tension, compression-compression or tension-compression. Equation 2.3 provides all other coefficients. The main downside to this failure criteria is that a fibre composite consists of very distinct phases: stiff elastic brittle fibres and a yielding matrix. Consequently, the failure of the material can occur due to multiple different mechanisms.

2.4.2. Damage initiation

Fibre reinforced polymers behave linear elastically with a plane stress orthotropic material stiffness matrix until damage is initiated. Damage initiation indicates the start of material degradation and occurs when the equivalent strain is larger than the damage threshold. Cracks in the material affect the stress and material stiffness of the surrounding integration points. Since the amount of energy stored in the fracture process zone can be relatively high, stable crack growth can occur before failure of the material. For fibre reinforced materials, Abaqus has implemented the damage initiation and evolution criteria based on the theory of Hashin and Rotem (1973) and Hashin (1980). An advantage of this theory is that Hashin differentiates between the different failure modes, while many other damage criteria only describe if a material is damaged or not. The theory considers four different damage initiation mechanisms, one for each of the failure modes, based on an excitation of the strength parameters. The general form of these initiation criteria is as follows:

- Fibre tension ($\hat{\sigma}_{11} \geq 0$):

$$F_f^t = \left(\frac{\hat{\sigma}_{11}}{X^T}\right)^2 + \alpha\left(\frac{\hat{\tau}_{12}}{S^L}\right)^2 \quad (2.5)$$

- Fibre compression ($\hat{\sigma}_{11} < 0$):

$$F_f^c = \left(\frac{\hat{\sigma}_{11}}{X^c}\right)^2 \quad (2.6)$$

- Matrix tension ($\hat{\sigma}_{22} \geq 0$):

$$F_m^t = \left(\frac{\hat{\sigma}_{22}}{Y^t}\right)^2 + \left(\frac{\tau_{12}}{S^L}\right)^2 \quad (2.7)$$

- Matrix compression ($\hat{\sigma}_{22} < 0$):

$$F_m^c = \left(\frac{\sigma_{22}}{2S^T}\right)^2 + \left[\left(\frac{Y^c}{2S^T}\right)^2 - 1\right]\left(\frac{\sigma_{22}}{Y^c}\right) + \left(\frac{\tau_{12}}{S^L}\right) \quad (2.8)$$

The definition of the parameters in the above equations is stated as:

X^T : tensile strength in the fibre direction;

X^C : compressive strength in the fibre direction;

Y^T : tensile strength in the direction perpendicular to the fibres;

Y^C : compressive strength in the direction perpendicular to the fibres;

S^L : longitudinal shear strength;

S^T : transverse shear strength;

α : coefficient that accounts for the contribution of the shear stress for the fibre tensile criteria

$\hat{\sigma}_{11}$, $\hat{\sigma}_{22}$, $\hat{\tau}_{12}$: components of the effective stress tensor, $\hat{\sigma}$.

The effective stress tensor ($\hat{\sigma}$) is computed from the nominal stress (σ) and the damage operator (M):

$$\hat{\sigma} = M\sigma \quad (2.9)$$

The damage operator consists of the internal damage variables d_f , d_m and d_s , that describe the current state of the fibre-, matrix- and shear damage, respectively. They are derived from the damage variables d_f^t , d_f^c , d_m^t , and d_m^c .

$$M = \begin{bmatrix} \frac{1}{1-d_f} & 0 & 0 \\ 0 & \frac{1}{1-d_m} & 0 \\ 0 & 0 & \frac{1}{1-d_s} \end{bmatrix} \quad (2.10)$$

$$d_f = \begin{cases} d_f^t & \text{if } \hat{\sigma}_{11} \geq 0 \\ d_f^c & \text{if } \hat{\sigma}_{11} < 0 \end{cases} \quad (2.11)$$

$$d_m = \begin{cases} d_m^t & \text{if } \hat{\sigma}_{22} \geq 0 \\ d_m^c & \text{if } \hat{\sigma}_{22} < 0 \end{cases} \quad (2.12)$$

$$d_s = 1 - (1 - d_f^t)(1 - d_f^c)(1 - d_m^t)(1 - d_m^c) \quad (2.13)$$

Before any initiation of damage, the effective stress tensor equals the nominal stress, thus $\hat{\sigma} = \sigma$. After the damage is initiated for one or more failure modes, the damage operator will influence the other damage initiation modes' criteria. It has to be noted that the Hashin criteria are claimed to be incapable of predicting the hardening effect under shear stress (Gu and Chen, 2017).

2.4.3. Damage evolution

After one or more damage initiation criteria are met, the damage evolution will define the material's further degradation. Each damage initiation criteria has a form of damage evolution, and multiple forms of damage evolution may act on the material simultaneously. The stress-strain relationship for a stable material is linear and follows from the true strain rate $\dot{\epsilon}$ and the damaged elasticity matrix \mathbb{C} :

$$\dot{\sigma}_{ij} = \mathbb{C}_{ijkl} \dot{\epsilon}_{kl} \quad (2.14)$$

$$\mathbb{C} = \frac{1}{D} \begin{bmatrix} (1-d_f)E_1 & (1-d_f)(1-d_m)v_{21}E_1 & 0 \\ (1-d_f)(1-d_m)v_{12}E_2 & (1-d_m)E_2 & 0 \\ 0 & 0 & (1-d_s)G \end{bmatrix} \quad (2.15)$$

E_1 and E_2 : Young's modulus in fibre- and matrix direction, respectively;

G : shear modulus;

v_{12}, v_{21} : Poisson's ratio

The material is stable and remains in equilibrium when the true stress ($\dot{\sigma}_{ij}$) and strain rate ($\dot{\epsilon}_{ij}$) have a positive stiffness tensor:

$$\dot{\sigma}_{ij} \dot{\epsilon}_{ij} > 0 \quad (2.16)$$

When this condition no longer holds, the material becomes unstable and reaches its bifurcation point. At this point, *strain-softening* occurs; decreasing stress for an increase in strain. Strain-softening is typically observed at a continuum level in damaged quasi-brittle materials, such as concrete and FRP. It is primarily a consequence of brittleness and heterogeneity of the material (Vignjevic et al., 2018). Finite element analysis of strain-softening materials combined with local constitutive models where damage is present leads to deformation localisation. *Localisation* is defined as instability in the macroscopic constitutive description of inelastic deformation of the material Rudnicki and Rice (1975). The imbalance of the material's stress-strain behaviour leads to large deformations, which localises within an infinitely small instability zone and becomes non-uniform. The result is numerical instability in local continuum damage models. The tangent stiffness tensor, which is the slope of the stress-strain curve, loses positive definiteness, which was the criteria for material stability presented in equation 2.16. The result is an infinite number of solutions.

Non-physical results occur with unrealistic energy dissipation due to damage with a zero volume zone (Vignjevic et al., 2014). Issues with boundary conditions arise from the material unloading outside of the localisation zone and the softening area acting as a free boundary. Deformation localises in a narrow zone, which is the fracture process zone. The material properties define the width and direction of such a band. As a result of this localisation, numerical predictions based on continuum damage mechanisms are strongly dependent on the mesh size of the finite element model and are thereby sensitive to mesh density. The amount of energy released by the cracking of the material depends on the mesh size, and for an infinitesimally refined mesh, it tends to zero. To prevent the localisation of smeared cracking into arbitrarily small regions, Bazant and Oh (1983) proposed a crack band model in which fracture is modelled as a band of parallel densely distributed micro-cracks. An adaptation of the crack band model is the smeared crack concept. This non-local damage theory relates the stress at any point to the deformation for a finite volume around that point. This is done by adjusting the energy dissipated by each failure mechanism and defining the fracture energy as a material parameter.

$$G_c = \int_{\bar{\epsilon}_0}^{\bar{\epsilon}_f} L_c \sigma_y d\bar{\epsilon} = \int_0^{\bar{u}_f} \sigma_y d\bar{u} \quad (2.17)$$

The fracture energy is now dependent on a characteristic length (L_c), which estimates to the length of the fracture process zone based on material properties. The definition of the characteristic length is applied, because the direction of the cracks is unknown. As a result, larger elements can have different behaviour, depending on the crack direction. For finite element analysis, the fracture energy is now considered as a model property and not as a material property. The definition of this characteristic length is dependent on the element geometry and element formulation. For a first order element, the

characteristic length is the line across an element and for a second order element it is half of the same length. For a shell, it is a characteristic length in its reference surface. With the introduction of the characteristic length, instead of a stress-strain response, a stress-displacement response is created after damage initiation. This equivalent displacement does not depend on the crack direction. The equivalent displacement (δ_{eq}^{ij}) and equivalent stress (σ_{eq}^{ij}) for the four damage modes are given as follows (Lapczyk and Hurtado, 2007):

- Fibre in tension ($\hat{\sigma}_{11} \geq 0$):

$$\delta_{eq}^{ft} = L^c \sqrt{\langle \epsilon_{11} \rangle^2 + \alpha \epsilon_{12}^2} \quad (2.18)$$

$$\sigma_{eq}^{ft} = \frac{\langle \sigma_{11} \rangle \langle \epsilon_{11} \rangle + \alpha \tau_{12} \epsilon_{12}}{\delta_{eq}^{ft} / L^c} \quad (2.19)$$

- Fibre in compression ($\hat{\sigma}_{11} < 0$):

$$\delta_{eq}^{fc} = L^c \langle -\epsilon_{11} \rangle \quad (2.20)$$

$$\sigma_{eq}^{fc} = \frac{\langle \sigma_{11} \rangle \langle \epsilon_{11} \rangle + \langle -\sigma_{11} \rangle}{\delta_{eq}^{fc} / L^c} \quad (2.21)$$

- Matrix in tension ($\hat{\sigma}_{22} \geq 0$):

$$\delta_{eq}^{mt} = L^c \sqrt{\langle \epsilon_{22} \rangle^2 + \epsilon_{12}^2} \quad (2.22)$$

$$\sigma_{eq}^{mt} = \frac{\langle \sigma_{22} \rangle \langle \epsilon_{22} \rangle + \alpha \tau_{12} \epsilon_{12}}{\delta_{eq}^{mt} / L^c} \quad (2.23)$$

- Matrix in compression ($\hat{\sigma}_{22} < 0$):

$$\delta_{eq}^{mc} = L^c \sqrt{\langle -\epsilon_{22} \rangle^2 + \epsilon_{12}^2} \quad (2.24)$$

$$\sigma_{eq}^{mc} = \frac{\langle -\sigma_{22} \rangle \langle -\epsilon_{22} \rangle + \tau_{12} \epsilon_{12}}{\delta_{eq}^{mc} / L^c} \quad (2.25)$$

The $\langle \cdot \rangle$ -signs represent the Macaulay bracket operator defined for every $\alpha \in \mathfrak{R}$ as $\langle \alpha \rangle = (\alpha + |\alpha|)/2$. The damage variable depends on the initial equivalent displacement (δ_{eq}^0) for which the initiation criteria for that mode is met. The equivalent displacement (δ_{eq}^f) is for the completely damaged stage of a the respective failure mode. The relation between the damage variable (d) and the equivalent displacement is presented in figure 2.9.

$$d = \frac{\delta_{eq}^f (\delta_{eq} - \delta_{eq}^0)}{\delta_{eq} (\delta_{eq}^f - \delta_{eq}^0)} \quad (2.26)$$

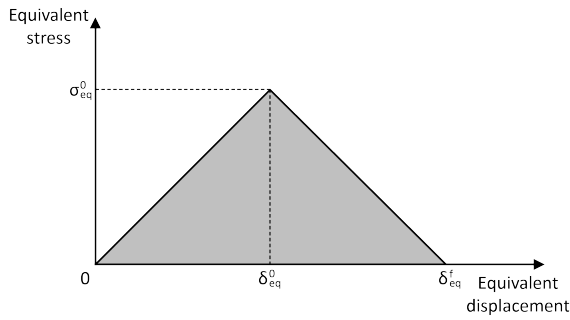


Figure 2.8: Equivalent stress versus equivalent displacement for each of the failure modes

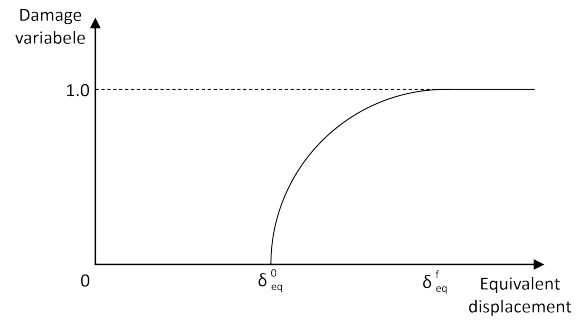


Figure 2.9: The damage variable as a function of the equivalent displacement

The toughness of a material is a measure of the amount of energy a material can absorb before it breaks. Due to the different fracture modes of the composite material, the characterisation of the fracture toughness of the material is still in development. Different tests are available for the determination of the interlaminar and intralaminar fracture toughness. Most research on the intralaminar fracture energy is conducted with Compact Tension (CT), Compact Compression (CC) or Three-Point Bend tests. For all three tests, an initial notch is made in a square or rectangular specimen. At the root of the notch, a starter crack has to be introduced, after which the specimen is loaded. The fracture toughness is determined from the relationship between the load initiating crack growth and the dimensions of the crack. Due to the wide range of FRP materials, different resin and fibres combination and lay-up options, the fracture toughness needs to be determined for each laminate specifically. Table 2.1 shows an overview of a view fracture energy values found in literature.

	G_{Ft} (N/mm)	G_{Fc} (N/mm)	G_{Mt} (N/mm)	G_{Mc} (N/mm)	E1 MPa	E2 MPa	σ_{Ft} MPa	σ_{Fc} MPa	σ_{Mt} MPa	σ_{Fc} MPa
Almeida-Fernandes et al. (2019)		20.2			29600	11900	322	70.7		
Barbero et al. (2013)				11.5	44700	12700	1020	620	40	140
Nunes et al. (2016)	2.38	5.28	0.424	0.948	36633	10754	365	468	86	110
Nunes et al. (2017)				9.48						
Xin et al. (2017)	12.5	12.5	5	5	39630	11670	1159	908	49	97

Table 2.1: Overview of fracture energy values found in literature for pultruded GFRP laminates

An option to approximate the fracture toughness of a material is from the area under the corresponding stress-strain curve. The height and width of this curve equal the strength and strain of the material. The strength of a material is equal to the force needed to break it, and the strain is the distance the material is stretched. Energy is force times distance, which is proportional to strength times strain. The fracture energy of a fibre reinforced polymer material in the normal direction is thus defined by the area under the normal traction-displacement curve (Tan et al., 2016).

Suppose the boundary conditions of a model are such that displacement is allowed only in the normal direction. In that case, the unloading follows a linear path after the initial equivalent displacement is reached, as shown in figure 2.8. The grey triangle-shaped area is equal to the specified fracture energy (G^c) dissipated due to failure; the values of δ_{eq}^f for the different modes depending on the corresponding G^c values. An accurate implementation of the fracture energy is necessary, because the fracture energy of each failure mode influences the damaged area, state of damage of the finite element, the ultimate load prediction and the post-failure behaviour (Barbero et al., 2013).

2.5. Buckling behaviour

Buckling is the phenomenon of thin-walled structures, such as plates and shells, that under certain levels of in-plane compressive loading or shear loading exhibit large out-of-plane deflection. Thin elastic plates can easily bend and are prone to rotations, even when subjected to relatively small loads. When a plate buckles, a sudden deviation occurs from a flat state into an out-of-plane state. It is an effect that occurs in structures with high stiffness in one direction and low stiffness in the other. Due to its anisotropic behaviour, fibre reinforced polymer composites are prone to buckling and deform relatively easily. Plates may, however, have a significant post-buckling capacity. The buckling and post-buckling behaviour lead to important design criteria for FRP structures. The possibility to modify the layer orientation and stacking sequence of an FRP laminate provides the option to find optimal structural configurations. Plate buckling behaviour can be determined analytically, from tests or with the use of FEM models.

2.5.1. Buckling design

The design of plates is usually dominated by stability (Bažant and Cedolin, 2010). To realise an exact analysis of a thin-walled member, the member needs to be treated as a continuous folded plate. Due to the high mathematical complexity of such a problem, most analyses consider an element as an assembly of individual plates with certain boundary- and loading conditions, such that the individual plates define the behaviour of the complete element. Figure 2.10 demonstrates this relation. Profiles are such an assembly in which flanges and webs are considered as separate plates with boundary conditions that take into account the interaction between each other. It is important to notice that idealised boundary conditions can not be realised in practice. The analysis of the non-linear static stability behaviour of composite plates and shells is based on governing differential equations.

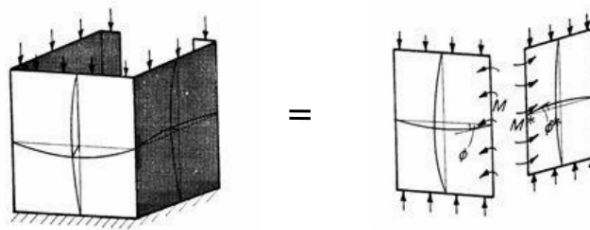


Figure 2.10: An element can be treated as a continuous folded plate which can be modelled as an assembly of individual plates (Landolfo, 2008)

When a plate buckles, it experiences a sudden deviation from a flat state under in-plane loading to a new state where the plate bends in the direction normal to the plane of the plate. Figure 2.11 demonstrates how a simply supported rectangular plate (a) deflects when the compressive load exceeds the critical buckling load (b). The critical buckling load, N_{cr} , is the load at which the plate buckles and can be determined with a linear eigenvalue analysis. This value depends on the geometry of the plate, the material properties, the type of boundary- and loading conditions.

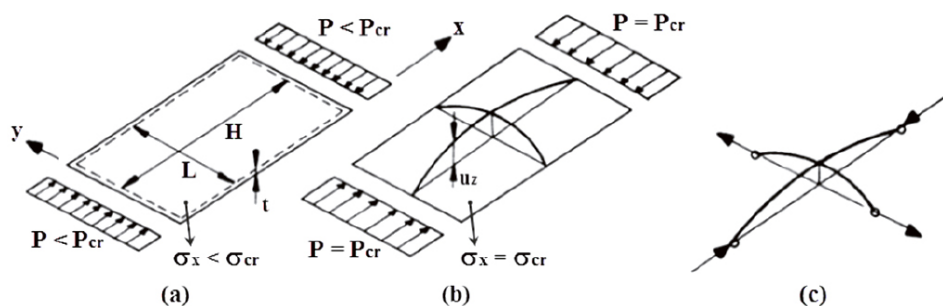


Figure 2.11: For loading below the critical buckling load, a perfect plate remains flat (a), but when the load reaches the critical buckling load, the plate buckles (b) and experiences out-of- plane deformation (c) (Helbig et al., 2016)

Plates exhibit post-buckling behaviour; the plate continues to carry the load after buckling. Figure 2.12 illustrates the post-buckling behaviour of a perfect plate and an imperfect plate. An imperfect plate has initial out-of-plane deformations, while a perfect plate is entirely straight. In the case of a perfect plate, for an increasing load below the buckling load, the plate shows no out-of-plane deflection and only shortens in the in-plane direction. When the critical buckling load is reached, the plate buckles and takes on a new shape and equilibrium state. The point at which a perfectly flat plate buckles under in-plane loading is known as the bifurcation point. Load eccentricities and geometric imperfections are initial imperfections that will result in an 'imperfect plate'. The plate will deviate from its flat state before the critical buckling load is reached. After the critical buckling load is reached, an increased out-of-plane displacement will occur, and the plate will approach the response of a 'perfect plate'. Bifurcation buckling analysis, asymptotic analysis and full non-linear analysis are methods available to analyse the geometrical non-linearity.

2.5.2. Initial imperfections

The buckling behaviour of a plate is influenced by geometrical imperfections, which signifies the importance of the manufacturing process on the material- and structural properties (Greenhalgh, 2009). Structural composite elements can have internal and external imperfections. Internal imperfections are material imperfections and occur within the material. Examples of this type of imperfections are voids, local waviness of the fabrics and initial delamination. External imperfections are geometrical imperfections. These arise from the deviations of the element's intended geometry—variations in thickness, flatness or straightness of the element and eccentricities within the loads or supports. The magnitude of the initial displacement and the load on the plate influences the magnitude of the out-of-plane deformation.

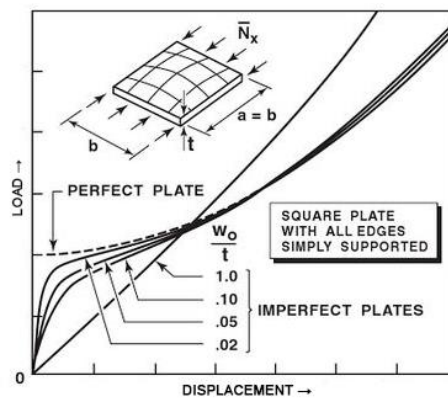


Figure 2.12: Buckling of a square plate with initial imperfections (Kaskovits, 2018)

Fibre misalignment, porosity and delamination are material defects that influence the strength and stiffness of the material and, therefore, the structural buckling and post-buckling behaviour. After the material has cured, residual stresses and residual deformations can occur, affecting the static response characteristics. The uncertainties of the material defects and geometrical imperfections make them important parameters for research. Post-buckling behaviour is a decisive aspect, both for the design of plate-type and shell-type composite structures (Degenhardt et al., 2014). Shell design and analyses aim to take the imperfection sensitivity into account for each specific situation and at the same time not be over-conservative.

Design codes, as mention in the subsection 2.5.3 and 2.5.4, describe that appropriate allowances should be considered in the structural analysis to cover the effects of imperfections. These imperfections include residual stresses due to curing, and geometrical imperfections, such as out-of-plane straightness, misalignment, unevenness, inaccuracies of fit in the area of joints and connections, and eccentricities. Effects of bow and other local geometrical imperfections, including pre-existing effects, need to be considered for analysis if they result in significant geometrical non-linear effects. The effects are significant if the internal forces and moments from the least favourable imperfection are more than 10% of the design loads on the member without imperfections.

A buckling reduction factor for members in compression in the direction of the fibres takes the effect of initial imperfections into account for the elastic buckling stage. For flat laminates, this factor is larger than 1.0 and can be conservatively taken as 1.0. The post-buckling capacity of an element is defined by the buckling and material strength. The design codes do not consider the influence of initial imperfections on the post-buckling capacity.

2.5.3. JRC - Prospect for new guidance in the design of FRP

A design procedure for local instability under longitudinal compression for pultruded double symmetric elements is provided in Annex C of the [Joint Research Centre \(2016\)](#). Calculation procedures are given for box, I-, C-, Z-, and L-sections. A structure is analysed as a set of plates. The design value for the compressive force is the design value of the local critical stress over the cross-sectional area, which is the minimum design value for the local critical stresses in the flanges or web under compression loading. The critical stresses are calculated depending on their boundary conditions, which describe the connection between the web and the flanges. The element with the lowest critical stress will buckle first. Due to the interaction between the elements, the other elements will restrain the part with the lowest critical buckling stress. The critical stress is evaluated with the restraining part and an additional stiffness as a rotational constraint.

This procedure is combined in a set of formulas for rectangular plates with different boundary conditions under compression loading or bending. A detailed insight into the background of the procedures in JRC can be found in the research paper "Local buckling of Fiber Reinforced Plastic Composite Structural Members with Open and Closed Cross Sections" by L.P. Kollar ([Kollar, 2003](#)). For a simply supported plate, critical stress calculation in case of compression, $\sigma_{cr,c}$, is presented in equation 2.27 and for a clamped plate in equation 2.28. These questions depend on D_{ij} , which are the element on row 'i' and column 'j' of the bending stiffness matrix, the thickness of the plate, t , and the width of the plate, b .

$$\sigma_{cr,c} = \frac{\pi^2}{tb^2} \left[2\sqrt{D_{11}D_{22}} + 2(D_{12} + 2D_{66}) \right] \quad (2.27)$$

$$\sigma_{cr,c} = \frac{\pi^2}{tb^2} \left[4.53\sqrt{D_{11}D_{22}} + 2.44(D_{12} + 2D_{66}) \right] \quad (2.28)$$

The influence of initial imperfections on buckling behaviour is implicitly taken into account by the interaction between local and global buckling modes under axial compression. Due to the linear behaviour of FRP for large strains, the local and global critical buckling stress can be in close range. When both buckling modes interact, a combined buckling mode can occur with a failure load below the predicted load for the separate buckling modes. In buckling design, this behaviour is taken into account by a reduction factor χ . The design force taking buckling into account, $N_{Rd2,c}$, is:

$$N_{Rd2,c} = \chi \cdot N_{loc,Rd} \quad (2.29)$$

- χ reduction factor for the interaction between local and global buckling
- $N_{loc,Rd}$ design value for the compressive force causing instability of the element

$$\chi = \frac{1}{c \cdot \lambda^2} \left(\Phi + \sqrt{\Phi^2 - c \cdot \lambda^2} \right) \quad (2.30)$$

- c numerical coefficient of 0.65 in the absence of more accurate tests
- λ relative slenderness
- Φ factor for the determination of reduction factor χ

$$\lambda = \sqrt{\frac{N_{loc,Rd}}{N_{Eul}}} \quad (2.31)$$

- N_{Eul} Eulerian critical load

$$N_{Eul} = \frac{\eta_c}{\gamma_M} \cdot \frac{\pi^2 \cdot E_{LC} \cdot I_{min}}{L_0^2} \quad (2.32)$$

- η_c correction factor for the shape of the beam cross-section
- γ_M partial material safety factor for buckling resistance
- I_{min} minimum value of the moment of inertia
- L_0 buckling length of the member

2.5.4. CUR96 - Dutch design guidance for infrastructure

Annex E of [CUR Recommendation 96 \(2017\)](#) provides a set of analytical formulas to determine the characteristic buckling strength for which wrinkling is taken into account, but imperfections are not. The flange's critical stress depends on factors that take the type of cross-section and loading conditions into account. These factors consist of the coefficient of restraint ξ , which is defined by the ratio between the width of the web and the width of the flange. Different material properties between the flanges and the web of a profile are not considered in these equations. When the material properties differ, the expression for the restraint coefficient should be calculated in line with the background document "Step-by-Step Engineering Design Equations for Fiber-reinforced Plastic beams for Transportation Structures" ([Davalos et al., 2002](#)). The critical buckling stress of the web is assumed as a plate with simply supported connections to the flanges. CUR96 provides formulas to calculate the critical local buckling stress of a profile. The resulting stress is the Euler buckling stress, which needs to be reduced to take imperfections into account. The resulting stress may also be determined from numerical models.

Critical buckling stress for the flange

$$f_{c,stab,k,f} = \frac{\pi^2}{12} \cdot \left(\frac{t_f}{b}\right)^2 \cdot \left[\sqrt{q} \cdot \left(2 \cdot \sqrt{E_x \cdot E_y}\right) + p \cdot (y \cdot v_{xy} + 2 \cdot G_{xy}) \right] \quad (2.33)$$

The constants p and q are defined by the coefficient of restraint ξ . This coefficient for restraint is as follows for I- and H-shaped cross-sections:

$$p = 0.3 + \frac{0.004}{\xi - 0.5}; \quad q = \frac{0.025 + \frac{0.065}{\xi + 0.4}}{\theta_{corr}^2}; \quad \xi = \frac{2 \cdot b_w}{b_f}; \quad b = \frac{b_f}{2}; \quad \theta_{corr} = 1.1 \quad (2.34)$$

Critical buckling stress for the web

$$f_{c,stab,k,w} = \frac{\pi^2}{t_w b_w^2} \left[2\sqrt{D_{11}D_{22}} + 2(D_{12} + 2D_{66}) \right] \quad (2.35)$$

- $f_{c,stab,k,w}$ characteristic compressive strength of the web taking wrinkling and plate imperfections into account
- t_w thickness of the web
- b_w width of the web

The characteristic value of the critical buckling force, $N_{b,Rd}$, is calculated as follows:

$$N_{b,Rd} = \chi \cdot \frac{\eta_c \cdot A \cdot \rho \cdot f_{c,k}}{\gamma_M} \quad (2.36)$$

- η_c conversion factor
- A area of the cross-section
- ρ reduction factor for local wrinkling and imperfections
- $f_{c,k}$ characteristic compressive strength
- γ_M partial factor that accounts for initial imperfections

Initial imperfections are taken into account by a partial factor γ_M , that consists of a factor for the uncertainties in obtaining the correct material factors, γ_{M1} and a factor for uncertainties in material properties due to the nature of the constituent parts and depends on the production method, γ_{M2} .

$$\gamma_M = \gamma_{M1} \cdot \gamma_{M2} \quad (2.37)$$

- $f_{c,stab,k}$ characteristic compressive strength considering wrinkling and plate imperfections

$$X = \frac{1}{\Phi + \sqrt{\Phi^2 - \bar{\lambda}_f^2}} \quad (2.38)$$

$$\Phi_{LT} = 0.5 \left[1 + \alpha_f (\bar{\lambda}_f - \bar{\lambda}_{f,0}) + \bar{\lambda}_f^2 \right] \quad (2.39)$$

- α_f imperfection factor
- $\bar{\lambda}_{f,0}$ plateau length of the buckling curve

Parameters α_f and $\bar{\lambda}_f$ depend on the shape of the considered cross-section and were determined experimentally and numerically.

$$\bar{\lambda}_f = \sqrt{\frac{A \cdot \rho \cdot f_{c,k}}{N_{cr}}} \quad (2.40)$$

CUR96 gives an additional guideline for plate buckling:

$$f_{x,Rd,c} = \alpha \cdot \frac{\eta_c \cdot \sigma_{cr,c}}{\gamma_M} \quad (2.41)$$

The critical buckling load can be determined from the supplied plate formulas. Imperfection factor, α must be determined in consultation with the supplier but can be taken conservative as the maximum value of allowed bow imperfection of B/125, with B being equal to the smallest value of the width or length of the plate.

2.6. Conclusion

Fibre-reinforced composites are formed by high strength fibres placed in a polymer matrix with distinct interfaces in between. The three constituents of the material result in three distinct damage mechanisms: damage to the matrix, damage to the fibres and damage to the interface. FRP's brittle failure behaviour is a significant concern for structural engineers. The ability to undergo inelastic deformation is an essential safeguard against failure in structural engineering. To safely design with FRP materials, a thorough knowledge of the failure modes and mechanisms is needed. To detect the failure of the material, initiation and propagation failure criteria are developed, which describe the materials damage. Progressive failure analysis can be used in combination with these failure criteria to predict the load-carrying capacity and failure propagation.

Continuum damage mechanics assumes that damage accumulates within a material, reducing the effective cross-sectional area and eventually leading to rupture. It is based on the concept that cracks or defects imply a reduced capacity to withstand stresses. The damage behaviour of a GFRP plate can be described with damage initiation and damage evolution criteria. Damage initiation criteria predict the failure of the material, and the damage evolution criteria describe the post-failure behaviour. Abaqus implemented the Hashin damage criteria as the default criteria for FRP material. The Hashin damage criteria differentiate between the four different failure modes: fibres in tension, fibres in compression, the matrix in tension and the matrix in compression. When the material reaches the ultimate strength for that failure mode, damage of a failure mode is initiated. After one or more damage initiation criteria are met, the damage evolution will define the material's further degradation.

Finite element analysis of strain-softening materials combined with local constitutive models where damage is present leads to deformation localisation. Localisation is defined as instability in the stress-strain relation of inelastic deformation of the material, which leads to numerical instability. The deformation localises in a narrow zone and is thereby sensitive to the mesh density. A finer mesh will decrease the amount of energy dissipated. [Bazant and Oh \(1983\)](#) proposed a crack band model to prevent this localisation into small regions. Fracture is modelled as a band of parallel densely distributed micro-cracks. This non-local damage theory relates the stress at any point to the deformation for a finite volume around that point. This is done by adjusting the energy dissipated by each failure mechanism and defining the fracture energy based on a characteristic length. For finite element analysis, the fracture energy is now considered as a model property and not as a material property.

The design of plates is usually dominated by stability. Structural composite elements can have internal and external imperfections, which influence the buckling behaviour of a plate. Fibre misalignment, porosity and delaminations are material defects influencing the strength and stiffness of the material and, therefore, the structural buckling and post-buckling behaviour. Load eccentricities and geometric imperfections are initial imperfections that will result in an 'imperfect plate'. An imperfect plate has initial out-of-plane deformations, and as a result, the plate will deviate from its flat state before the critical buckling load is reached. Post-buckling behaviour is a decisive aspect for the design of plate- and shell-type composite structures. Shell design and analyses aim to take the imperfection sensitivity into account for each specific situation and try not to be over-conservative. A buckling reduction factor for members in compression in the direction of the fibres takes the effect of initial imperfections into account for the elastic buckling stage. The design codes do not consider the influence of initial imperfections on the post-buckling capacity. Progressive failure analysis is used to include the effect of damage and determine the load-carrying capacity for structures with post-buckling behaviour, which is only possible with a proper damage model that characterises the onset and evolution of damage.

3

One-element model

The previous chapter established that damaged quasi-brittle materials experience strain-softening behaviour at a continuum level. Finite element analysis of damage behaviour for materials with strain-softening experience mesh sensitivity: a more refined mesh will decrease the amount of energy dissipated. To reduce this mesh dependency for numerical analysis, a stress-displacement response is created instead of a stress-strain response after the damage is initiated. This stress-displacement response creates a dependency between the fracture energy and the element size of the finite element model. A model consisting of one element is built to verify the relation between the fracture energy and the element size and to evaluate how a change in element size influences the material's failure behaviour.

3.1. Equivalent displacement model

The equivalent displacement theory described in the previous chapter is illustrated by comparing the failure behaviour of a numerical model, created with Abaqus/Standard, consisting of one element with the defined definitions for the initial equivalent displacement and the equivalent displacement at the completely damaged stage. The mesh size is chosen equal to the element size to prevent mesh dependency, which is then, by definition, equal to the characteristic length. The characteristic length is dependent on the element geometry and element formulation. Different sized models are built, and both conventional shells with S4R elements and continuum shells with SC8R elements are created.

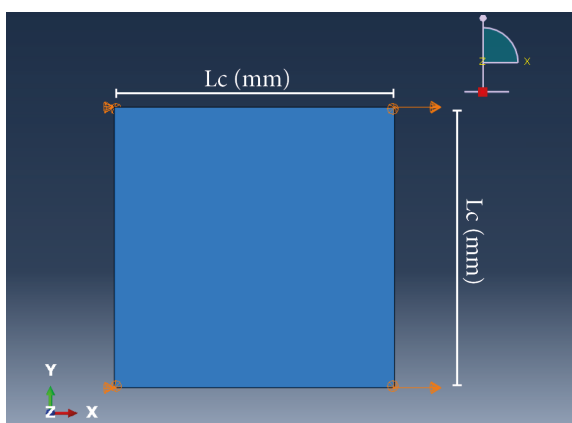


Figure 3.1: Conventional shell model

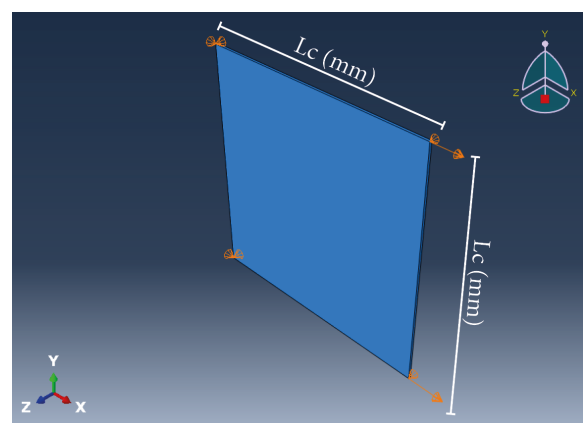


Figure 3.2: Continuum shell model

A conventional shell element is a 2D element with displacement and rotational degrees of freedom. Solid elements are 3D elements with only displacements as degrees of freedom (Asicone et al., 2012). Conventional shell elements are a good choice to define the orthotropic behaviour for analysis on ply level. Solid elements offer the option to model delamination, out-of-plane shear and through-thickness behaviour. A third type of elements is continuum shell elements, also referred to as 2.5D elements. The continuum shell element is a three-dimensional continuum solid with kinematic and constitutive behaviour similar to conventional shell elements. Figure 3.2 shows the difference in finite element modelling between the two types of shell bodies. An advantage of conventional shell elements is that the material's composite lay-up can be easily defined as a cross-section property. However, stresses and stiffness in the through-thickness direction and out-of-plane shear properties are not exact. It is not possible to model delamination if the member consists of one element in the through-thickness direction.

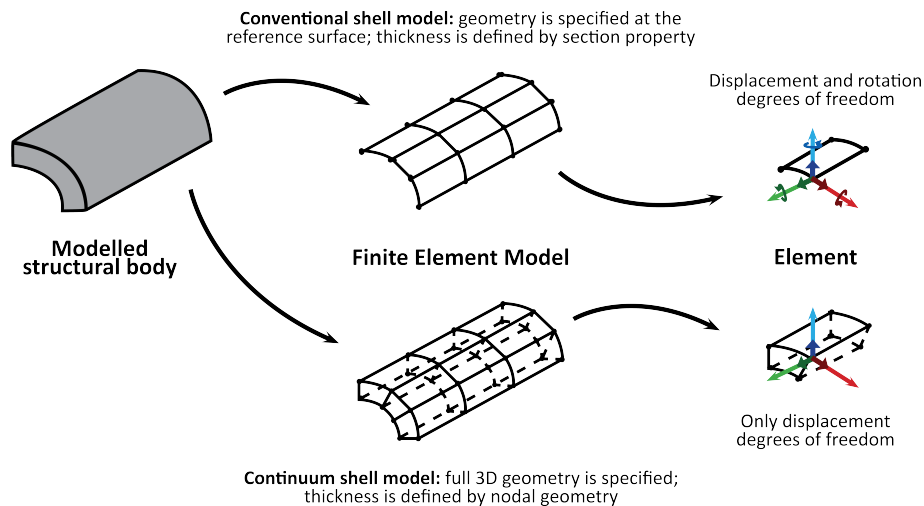


Figure 3.3: Difference between a conventional shell and continuum shell model (Systèmes, 2011)

In this chapter, the numerical models consist of one layer of a GFRP material, loaded until failure. Loading is applied in four directions, which correspond with the four failure modes. Figure 3.4 illustrates the relation between the loading direction and failure mode.



Figure 3.4: Schematization of the four different loading directions

The values for the fracture energy are implemented as stated in the report "Pin Bearing in Glass Fiber-Reinforced Polyester: An experimental and numerical study on the static and fatigue response of a GFRP laminate" (Cornelissen, 2020). In this report, the GFRP laminate is subjected to flat coupon tests to determine the material's strength, stiffness, and ultimate strain. The area under the resulting stress-strain curves is used to calculate the fracture energy for each failure mode. It has to be noted that flat coupon tests not intended to determine the actual fracture energy of the material. No minimum element

size restriction applies, and the discreteness of any method can be increased with mesh refinement, however, this may lead to high computational costs. The equivalent displacement equations prescribe that the mesh size of the model can be increased up to the maximum characteristic length, $L_{c,max}$.

$$L_{c,max} = \frac{2EG_c}{\sigma_c^2} \quad (3.1)$$

- E stiffness in the direction of the loading
- σ_c^2 ultimate stress for the respective loading direction

If this equation is not satisfied, the numerical analysis will produce inaccurate results; the fracture energy provided is less than the energy needed to open a unit area of crack. As a result, damage will not be initiated. The maximum mesh size for each of the four models is as follows:

- Tension in fibre direction: 2.35 mm
- Compression in fibre direction: 2.08 mm
- Tension in matrix direction: 42.6 mm
- Compression in matrix direction: 2.00 mm

3.2. Material properties

The material properties for the numerical model are from the beforementioned report (Cornelissen, 2020). The material properties for each of the failure modes are provided in table 3.1 and 3.2. The expected equivalent displacement is calculated according to equations 3.2 till 3.5. Displacement is applied to obtain failure of the models.

	Strength (N/mm^2)	Fracture Energy (N/mm^2)	Viscosity coefficient (–)
Longitudinal Tensile	845.8	20.1354	0.001
Longitudinal Compressive	486	5.832	0.001
Transverse Tensile	25.8	1.1	0.005
Transverse Compressive	116.1	1.045	0.005
Longitudinal Shear	73.45		
Transverse Shear	73.45		

Table 3.1: Material properties for the four failure modes

E_1	E_2	E_3	ν_{12}	ν_{13}	ν_{23}	G_{12}	G_{13}	G_{23}
41700	12900	12900	0.28	0.28	0.28	3560	3560	3560

Table 3.2: Input values for the engineering constants

$$\epsilon_{eq}^0 = \frac{\sigma_c}{E_c} \quad (3.2)$$

$$\delta_{eq}^0 = \epsilon_{eq}^0 L_c \quad (3.3)$$

$$\epsilon_{eq}^f = \frac{G_c}{0.5\sigma_c L_c} \quad (3.4)$$

$$\delta_{eq}^f = \frac{G_c}{0.5\sigma_c} \quad (3.5)$$

3.3. Conventional shell element results

The numerical results are compared to the results from equation 3.2 up to and including 3.5. The Abaqus/Standard models are created with conventional shell elements. The equations in the plots referenced with 'Eq.' are in good agreement with the FEM models. Three of the four graphs show that the numerical models align with the equivalent displacement theory. The ultimate strength of the material is equal to the maximum stress in the model. When the material reaches the ultimate strength, damage is initiated, and failure occurs.

The material strength is equal to the maximum stress, and when the material reaches its ultimate strength, the material damages and eventually fails. Graph 3.5c with the result from the stress-displacement for tension loading in matrix direction shows a higher peak than expected. This behaviour is explained at the end of this section. For each of the four models, only failure in the respective failure mode developed. The damage variables for failure of the models can be found in appendix A.

Figure 3.7 shows the stress-strain curve of the same four models for each of the four failure modes. The area under the curve increases for a smaller element size. This increase relates to the indication of mesh dependency due to strain-softening behaviour, which results in a finer mesh decreasing the amount of energy dissipated. The ultimate strain is a material property and is not influenced by the mesh size; the behaviour until damage initiation remains the same.

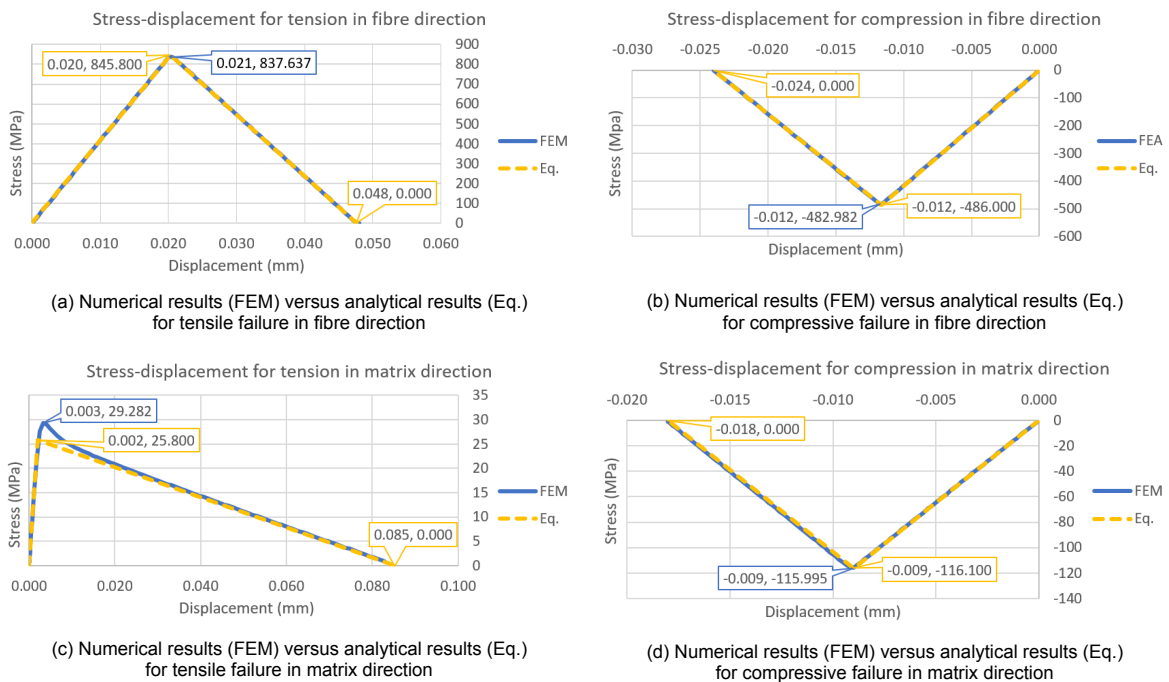


Figure 3.5: Stress-displacement comparison of the analytical results (Eq.) and the numerical output of the Abaqus/Standard conventional shell element model (FEM) for an element of 1.0 by 1.0 mm for each of the four failure modes

The area under the stress-displacement curve is equal to the fracture energy input in the FEM model for each respective failure mode. Figure 3.6 shows that the area under the curve remains the same for a change in element size. Smaller elements require less displacement to reach the materials ultimate strain, at which damage is initiated. These results show that the stress-displacement response of the material depends on the mesh size of the FEM model.

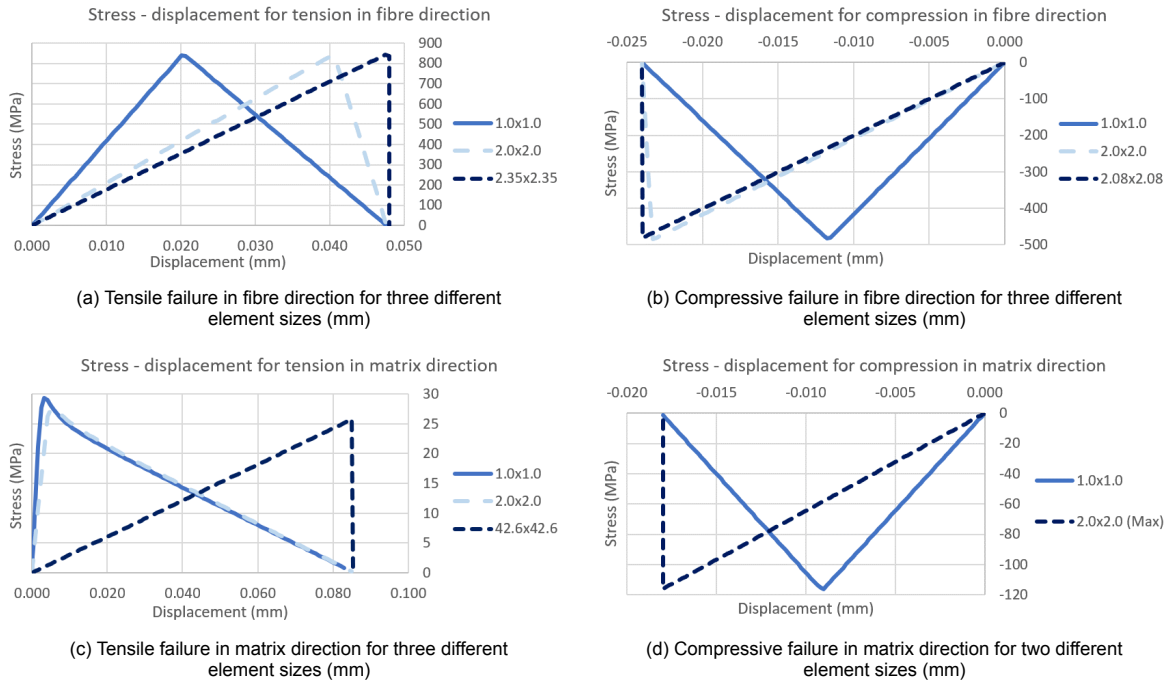


Figure 3.6: Numerical determined stress-displacement curves for the four failure modes with an element size of 1.0 by 1.0 mm, 2.0 by 2.0 mm and the maximum characteristic element size. For figure d, the maximum characteristic element size equals 2.0 by 2.0 mm.

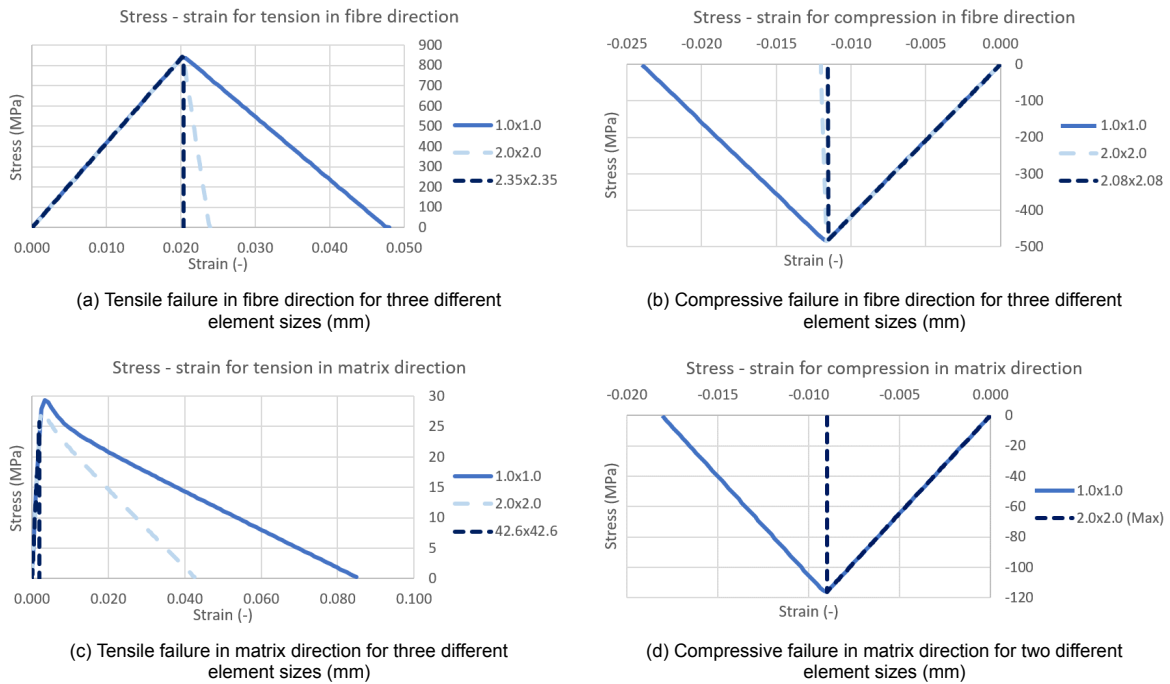


Figure 3.7: Numerical determined stress-strain curves for the four failure modes with an element size of 1.0 by 1.0 mm, 2.0 by 2.0 mm and the maximum characteristic element size. For figure d, the maximum characteristic element size equals 2.0 by 2.0 mm.

Peak occurrence for tensile failure in matrix direction

The stress-displacement and stress-strain curves for tensile failure in matrix direction show a higher peak than expected. The material's maximum stress exceeds the material's ultimate strength for the failure mode tension in fibre direction. This peak disappears when the element size is increased to the maximum element size of 42.6 mm, which is shown in figure 3.6 (c) and 3.7 (c). When the maximum element size is 40 and 20 times higher than the studied element sizes of 1.0 by 1.0 and 2.0 by 2.0, it is plausible that the fracture energy is too high for the model to capture the failure behaviour accurately.

Stress-displacement comparison of the four failure modes

Figure 3.8 shows the numerical results for the stress-displacement failure behaviour of the 1.0 by 1.0-millimetre elements in each of the four loading directions. The area under each of the four triangles is equal to the input fracture energy for the related failure mode. The initial equivalent displacement is defined as $D_{eq,0}$ and the equivalent displacement at the completely damaged stage as δ_{eq}^f . The initial equivalent stress (σ_{eq}^0) equals the strength of the material respective to their loading direction.

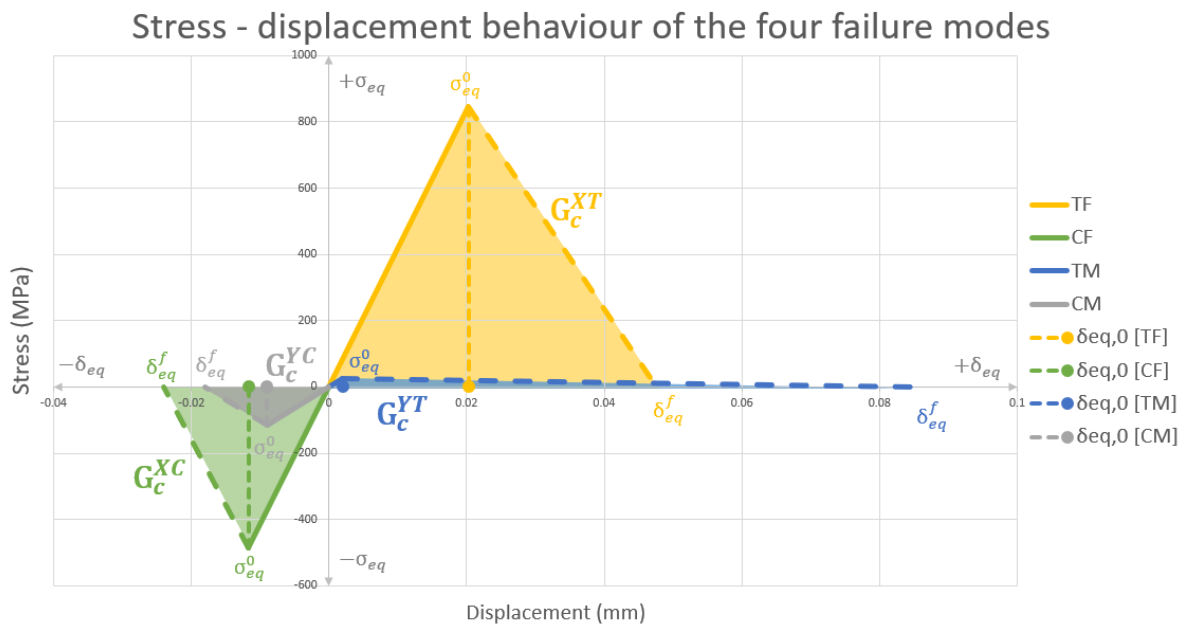


Figure 3.8: Numerical results for the stress-displacement behaviour of the four failure modes

3.4. Continuum shell element results

The choice of element type influences the mesh dependency of the FEM models. Four continuum shell models are created in Abaqus/Standard. The output of those four models is compared to the results from equations 3.2 till 3.5, similar as for the conventional shell models. The same four failure modes are analysed: compression and tension in fibre and matrix direction. The size of the models is 1.0 by 1.0 millimetres, and they all consist of one element. Figure 3.9 demonstrates that the numerical output is in agreement with the analytical result from the equivalent displacement theory. For each of the four models, only failure in the respective failure mode developed. The damage variables for failure of the models can be found in appendix A. The conventional- and continuum shell models result in the same stress-displacement curves.

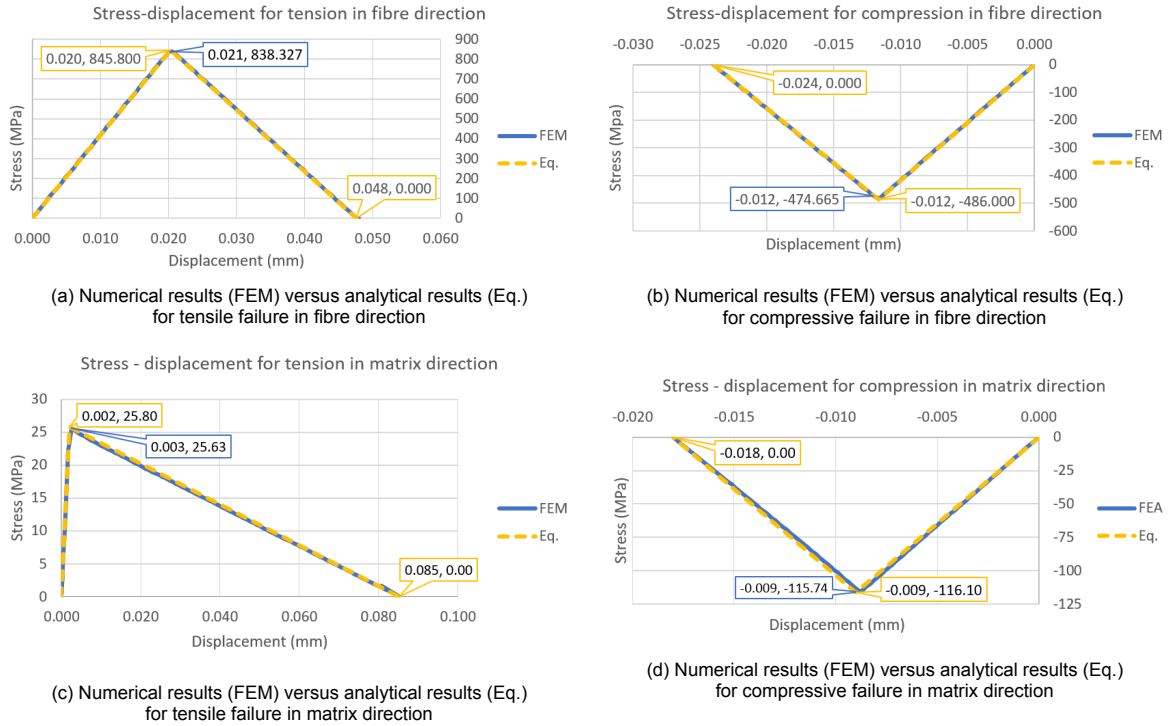


Figure 3.9: Stress-displacement comparison of the analytical results (Eq.) and the numerical output of the Abaqus/Standard continuum shell element model (FEM) for an element of 1.0 by 1.0 mm for each of the four failure modes

3.5. Conclusion

The one-element models follow an elastic loading and unloading path. When the material's ultimate strength is reached for its respective loading direction, the damage initiation criteria for the corresponding failure mode are met. For the stress-displacement output, the equivalent displacement at failure is independent of the mesh size, but the displacement at which damage is initiated changes. Smaller elements require less displacement to reach the materials ultimate strain, at which damage is initiated. After that, the evolution of damage proceeds more gradual and the different sized models are completely failed for equal applied displacement. The larger elements withstand a higher displacement until the materials ultimate strain is reached and damage is initiated, followed by a more immediate damage evolution. The area under the stress-displacement curve remains the same and is equal to the implemented fracture energy value.

The stress-strain graphs show that the element size influences the material's behaviour after damage initiation. A decrease in element size for a constant fracture energy results in a more graduate damage development. Consequently, the area under the curve increases for a smaller element size. This increase relates to the indication of mesh dependency due to strain-softening behaviour, which results in a finer mesh decreasing the amount of energy dissipated. The ultimate strain is a material property and is not influenced by the mesh size; the behaviour until damage initiation remains the same. The one-element models created in Abaqus/Standard show that stress-strain and stress-displacement results are mesh-size dependent. The equivalent displacement response is observed for both conventional and continuum shell elements.

4

Uni-directional model

The Hashin damage criteria can be used to model the damage of an FRP component. These criteria differentiate between the four failure modes and require the fracture energy of the material as input. One method to obtain these values is by calculating the area under the stress-strain curve of experimental flat coupon tests. In this chapter, fracture energy values determined from such tests are implemented in a numerical model of four uni-directional plies. The numerical outcome is compared to the coupon experiments. The influence of the dependency between the fracture energy and the model's mesh size on the failure behaviour of the model is evaluated by varying both the fracture energy input and element size.

4.1. Uni-directional coupon tests

A series of experimental flat coupon tests were performed by Lieuwe Cornelissen and reported in the paper "Pin Bearing in Glass fiber-Reinforced Polyester" (Cornelissen, 2020). For this research, uni-directional panels were manufactured to create specimen with 0° and 90° orientations. The specimens were loaded in tension and compression in the longitudinal and transverse direction, which aligns with the four failure modes as discussed in chapter 3, figure 3.4. For each direction, seven specimens were created. The specimens were made from E-glass fibres with a silane coating and a dicyclopentadiene-modified unsaturated polyester resin, with a fibre volume ratio of 0.54. The coupons were tested until failure. From the experimental test results, the material properties and geometry for a representative Abaqus/standard model are defined and used to calculate the materials' fracture energy.

4.1.1. Model properties

Coupon testing was performed according to ISO 527 (Normcommissie:310061, 2012) for tensile tests and according to ISO 14126 (Normcommissie:310061, 1999) for compression tests. The tested coupons' geometry is presented in figure 4.1 till 4.4.

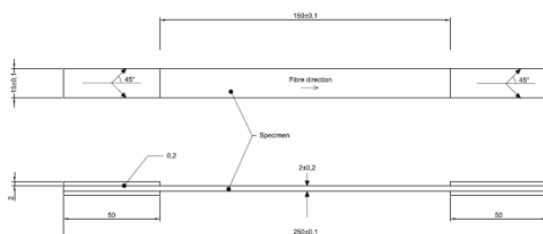


Figure 4.1: Coupon geometry for 0° tensile testing (ISO527-5 type A)

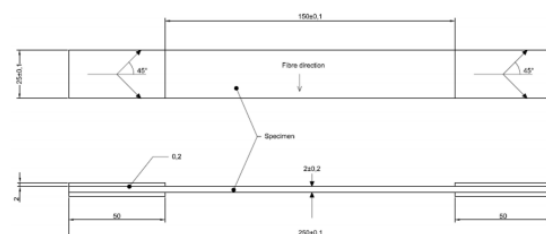


Figure 4.2: Coupon geometry for 90° tensile testing (ISO527-5 type B)

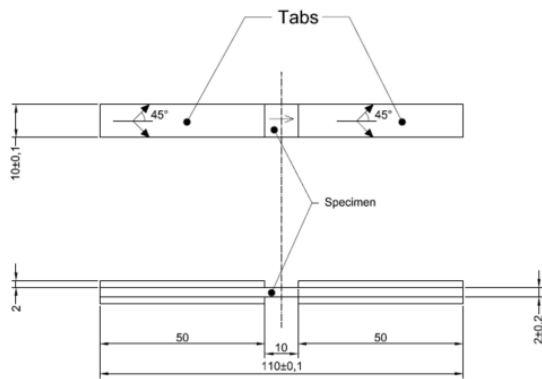


Figure 4.3: Coupon geometry for 0° compressive testing (ISO14126)

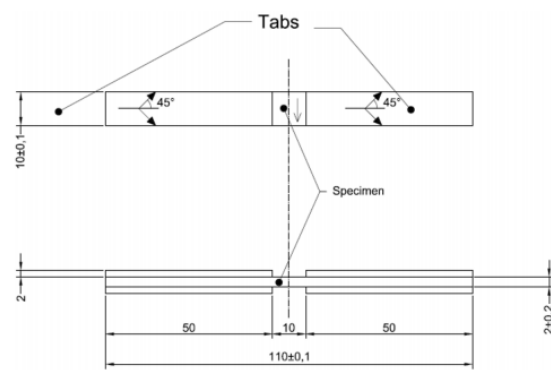


Figure 4.4: Coupon geometry for 90° compressive testing (ISO14126)

The material properties of the models are determined from the experimental test results. The plate geometry and boundary conditions for the four models are shown in figures 4.5 and 4.6 and stated in table 4.1. The plates are loaded by a displacement in the x-direction. For the models loaded in the longitudinal direction, this aligns with the direction of the fibres. For transverse loading, the material orientation is rotated 90 degrees. The opposite side of the displacement restraints movement in the x-direction. In one node, all degrees of freedom are fixed.

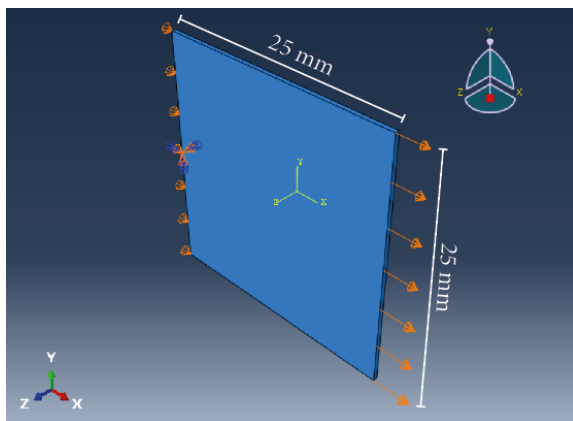


Figure 4.5: Geometry for the models loaded in tension

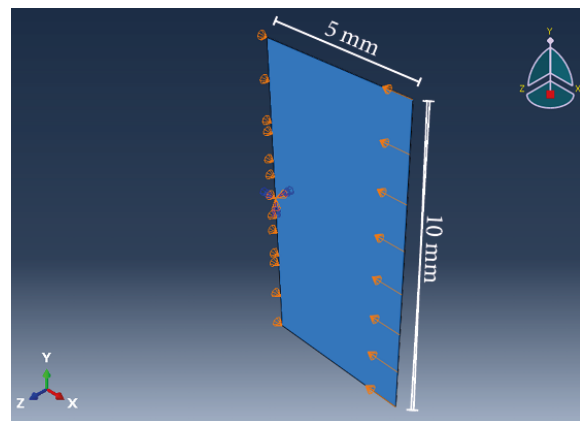


Figure 4.6: Geometry for the models loaded in compression

The clip length of the coupons loaded in the longitudinal direction is 50.00 millimetres, while the width and thickness are 25.00 and 1.72 millimetres, respectively. Due to symmetry, the Abaqus/Standard model is a 25.00 by 25.00-millimetre plate. The specimens consist of four layers of fibres, each with 0.43-millimetre thickness. The numerical model is created with one layer of fibres. For the coupons loaded in the transverse direction, the length between the test machine's clamps is 10.00 millimetres, which is the same size as the coupon's width. The numerical mode is a 5.00 by 10.00-millimetre plate with a thickness of 0.43 millimetre. A static general analysis is performed.

In chapter 3 it was determined that both conventional and continuum shell elements can be used. Preference is given to the continuum shell elements, which will be used for the numerical models, due to the inclusion of transverse shear deformation and changing thickness. The models consist of continuum shell elements with an SC8R mesh: an 8-node quadrilateral in-plane general-purpose continuum shell with reduced integration with hourglass control and finite membrane strains. Distribution of the elements is as demonstrated in figure 4.7 and figure 4.8.

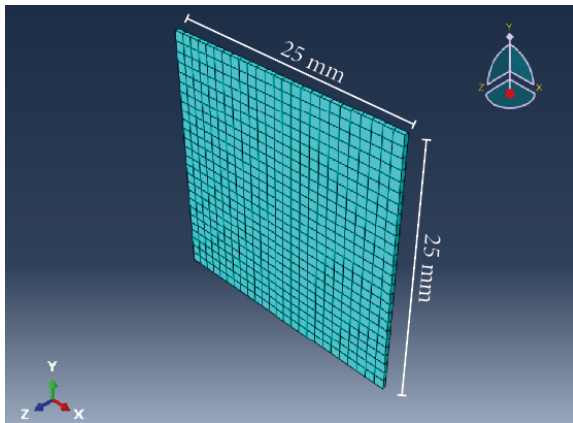


Figure 4.7: Mesh size of 1.0 by 1.0 mm for tension models

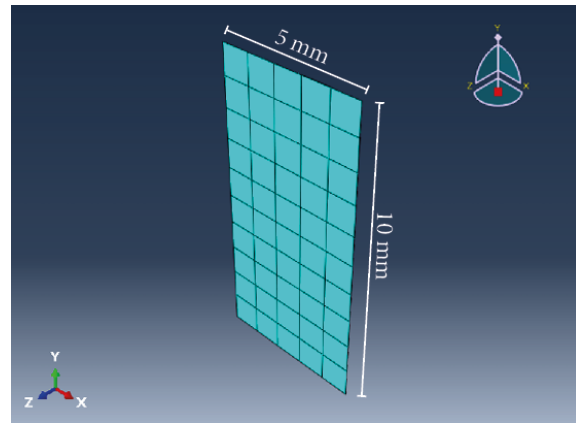


Figure 4.8: Mesh size of 1.0 by 1.0 for compression models

4.1.2. Post-failure behaviour experiments

The results of the four experimental flat coupon tests are shown in figure 4.9 up to and including 4.12. The data is acquired from the aforementioned report (Cornelissen, 2020). Capturing the post-failure behaviour of the specimens turned out to be complicated. The results show a large scatter of data. For the uni-axial tensile test in fibre direction, the ultimate strain showed large amount of scatter at the end of the elastic region, with a coefficient of variation of 7.36%. A possibly explanation could be the explosive nature of the failure mode, which shifted the clips of the extensometer. For the specimen under uni-axial tensile loading in matrix direction, the fibres continued to carry the loading after the matrix failed. In case of compressive loading in fibre direction, failure between the tabs, buckling of the specimen and unusable DIC data led to three unsuccessfully performed tests. Three specimens loaded in compression in matrix direction were successfully tested. Others experienced cracking when placed in the test set-up and technical difficulties with the DIC measurements occurred.

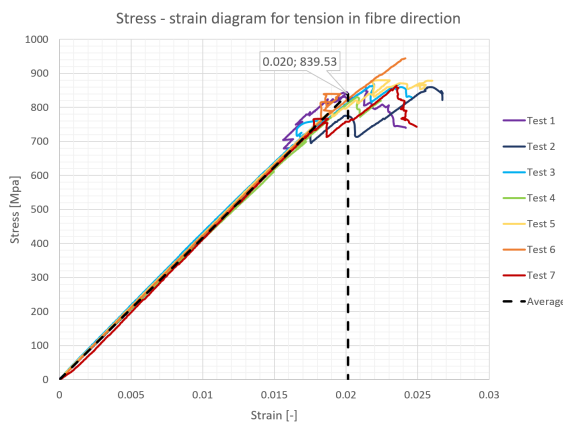


Figure 4.9: Experimental results for 0° tensile model (UDT0)

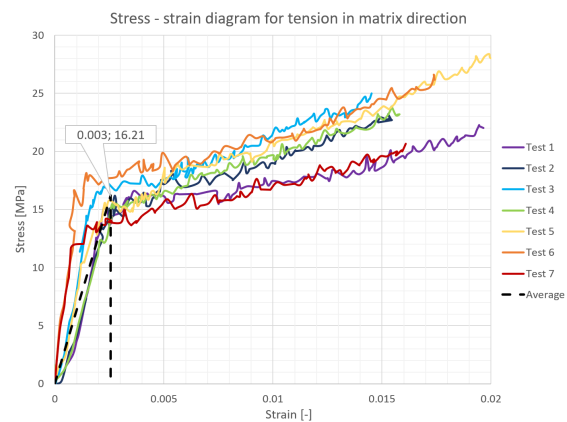


Figure 4.10: Experimental results for 90° tensile model (UDT90)

4.1.3. Lower bound fracture energy

The material properties are determined from the average results of the coupon tests. These properties include the strength, stiffness and ultimate strain of the material. The average test results for each loading direction is plotted onto the actual test results with a black dotted line. The first part of this line represents the elastic behaviour of the coupons until the ultimate strength of the material is reached. After this point, the black dotted line shows abrupt failure of the material, even though not all experimental results show this behaviour. When the material fails abruptly, it equals the lower bound fracture energy, considering that the fracture energy does not influence the elastic behaviour. A more gradual failure, where the material can experience more strain before complete failure, equals a higher fracture energy; more fracture energy can be absorbed before the material is completely damaged.

The lower bound fracture energy is a conservative option for modelling failure of a material, abrupt failure means that there is no post-failure load carrying capacity in the material. However, when the actual fracture energy of the material is lower than the determined lower bound value, the fracture toughness of the material is overestimated. Due to the beforementioned lack of post-failure data, the choice has been made to implement the materials lower bound fracture energy. The lower bound values can be calculated from the stress-strain curve with abrupt failure after the materials ultimate strength is reached. Hence, the fracture energy, G_c depends on the material strength (σ_{max}) and the ultimate strain (ϵ_f), which for the lower bound value equals the strain at damage initiation. To implement the fracture energy in the numerical model it was determined in chapter 3, that the experimental determined value needs to be multiplied by the mesh size. The fracture energy input value is thus calculated as follows:

$$G_{c,lowerbound} = 0.5 * \sigma_{max} * \epsilon_f * L_c \quad (4.1)$$

4.1.4. Material properties

The average test results for tensile loading in the fibre direction and tensile loading in the matrix direction are shown with a black dotted line in figure 4.9 and 4.10, respectively. The stress-strain curve of the second situation shows bi-linear behaviour, which originates from the stitching fibres that continue to carry the ply's strength after the resin has failed. A numerical model including the bi-linear behaviour could not be obtained with implicit analysis. The numerical model will approach the stress-strain curve without the bi-linear behaviour and only displays the behaviour of the resin's strength in the transverse direction.

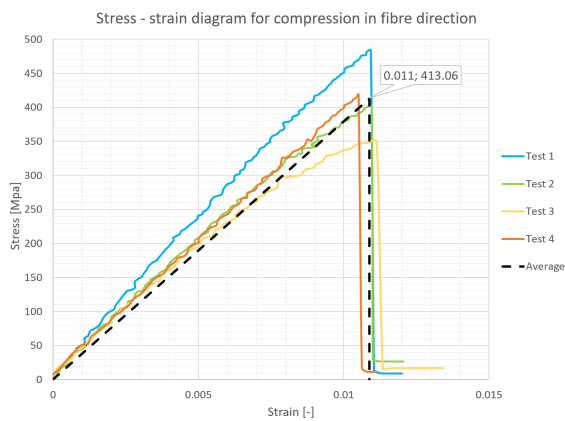


Figure 4.11: Experimental results for 0° compression mode (UDC0)

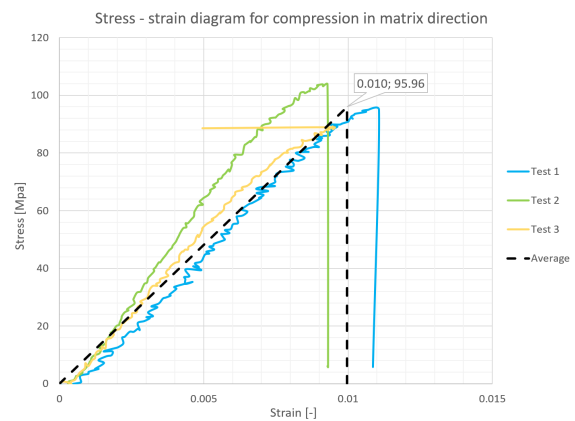


Figure 4.12: Experimental results for 90° compression model (UDC90)

The results of the uniaxial compressive tests are shown in figure 4.11 and 4.12. As mentioned in subsection "Lower bound fracture energy", due to various reasons, not all specimens were tested successfully. Table 4.1 provides an overview of the geometry and material parameters obtained from the tests.

	Length (mm)	Width (mm)	Thickness (mm)	Strength (MPa)	Stiffness (MPa)	Ultimate strain (-)
UDT0	25.00	25.00	0.43	839.53	41700	0.0201
UDT90	25.00	25.00	0.43	16.21	6317	0.0026
UDC0	5.00	10.00	0.43	413.06	37939	0.0109
UDC90	5.00	10.00	0.43	95.98	9634	0.0100

Table 4.1: Geometry and material properties of the four different models

4.1.5. Models loaded in tension

First, the numerical results of the specimens loaded in tension are discussed. A model with a characteristic element length of 1.00 millimetre is given a positive displacement in the fibres' direction. For this case, the lower bound value of the fracture energy is 8.45 N/mm. Figure 4.13 shows that the resulting stress-strain curve, the green line, is similar to the average test result, the black dotted line. A slightly more accurate result occurs for a fracture energy input of 8.40 N/mm, displayed by the yellow line. Table 4.2 displays the difference between the lower bound fracture energy input value and the numerical results. The output fracture energy value is the area below the numerical created stress-strain graph.

	σ_c (N/mm ²)	ϵ_0 (-)	L_c (mm)	G_c (N/mm)	Difference (%)
Input	839.53	0.02013	1.0	8.45	
Output	835.55	0.02009	1.0	8.39	-0.70%
Input	839.53	0.02013	2.5	21.13	
Output	838.46	0.02011	2.5	21.07	-0.27%

Table 4.2: UDT0: difference between the lower bound fracture energy (input) and numerical stress-strain area (output)

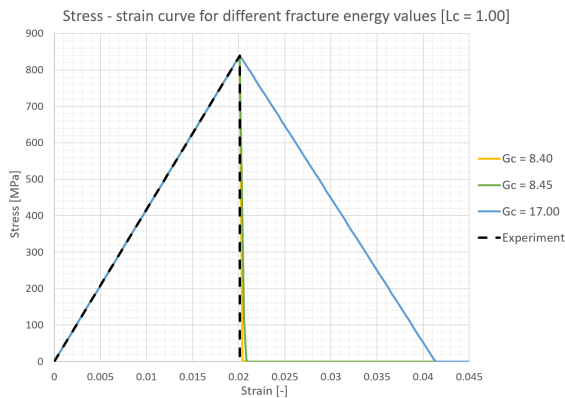


Figure 4.13: UDT0 stress-strain curve for different fracture energy values and element size of 1.00 mm

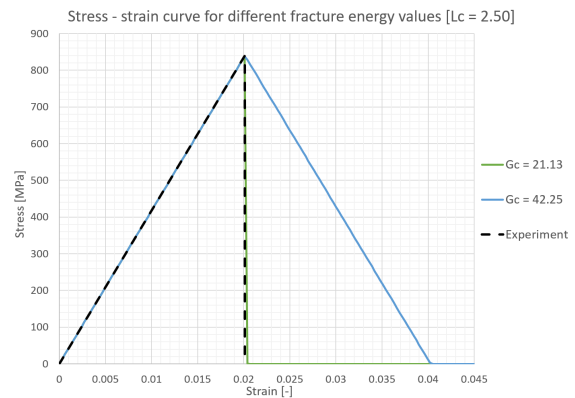


Figure 4.14: UDT0 stress-strain curve with different fracture energy values and element size of 2.50 mm

When the fracture energy input is increased by a factor of two, and no other parameters are changed, the area under the resulting stress-strain curve also doubles in size. The blue line indicates the stress-strain curve for the fracture energy input equal to twice the lower bound value. When the element size increases, the related lower bound fracture energy value needs to be increased proportionately.

Figure 4.14 demonstrates the results for an element size of 2.50 by 2.50-millimetres, with a fracture energy input of 17.00. The material properties of the model remain the same. The lower bound fracture energy value gives an accurate result; the value under the stress-strain curve multiplied by 2.5 equals the fracture energy input value. For this situation, increasing the fracture energy input by a factor of two also results in the area under the stress-strain curve increasing by the same factor.

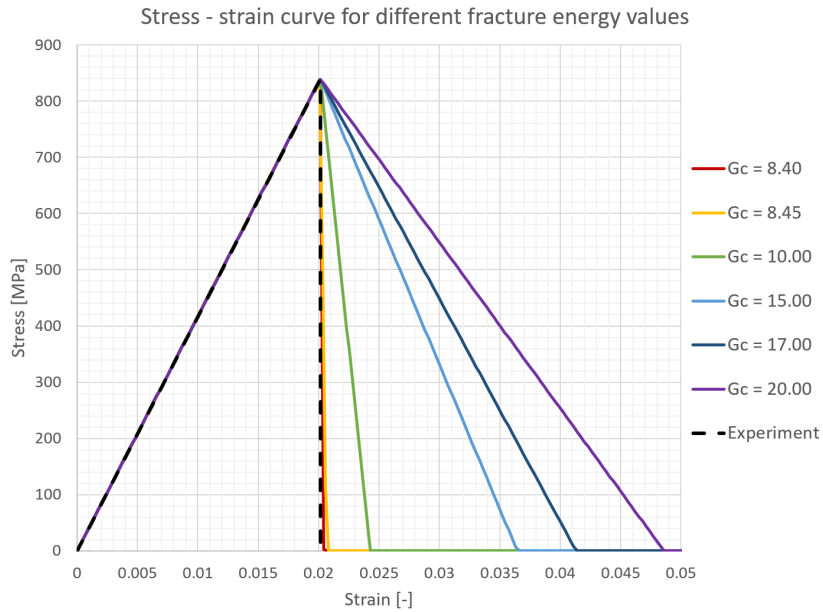


Figure 4.15: UDT0 stress-strain curve with different fracture energy values and an element size of 1.00 mm

When a material has a higher fracture energy it means that more energy can be absorbed before ultimate failure of the material is reached. For the numerical model, a higher fracture energy input relates to a more gradual degradation after damage is initiated in the material. To demonstrate this behaviour, the previous model, with a characteristic element length of 1.00 millimetre, is given a positive displacement in the direction of the fibres. The fracture energy input is varied between 8.4 N/mm and 20 N/mm. Figure 4.15 shows the results and demonstrates that the slope after damage initiation degrades more gradually for a higher fracture energy input.

Additionally, the corresponding fracture energy input values are plotted against the resulting area under their stress-strain curves. As shown in figure 4.16, the fracture energy input values and the area under the curves are similar. As expected, a linear relationship can be identified, which relates to the established linear relationship between the fracture energy and mesh size. The lower bound value of 8.45 N/mm for the fracture energy and the smallest possible area under the stress-strain curve is presented in vertical and horizontal directions. The area's under the curves are within a 4% difference of the fracture energy input values.

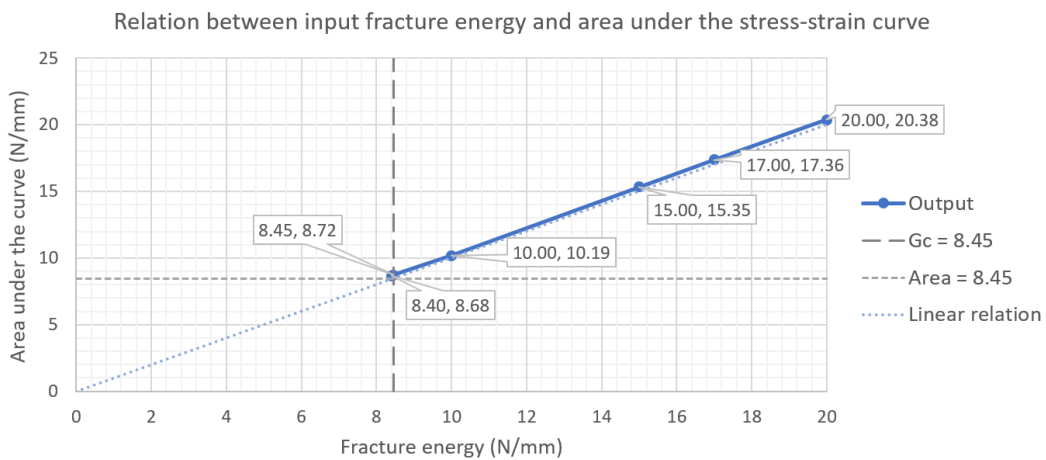


Figure 4.16: Relation between the fracture energy input and area under the stress-strain curve

The stress-strain curves for the model loaded in tension in the transverse direction are depicted in figure 4.17 and 4.18. For an element size of 1.00 by 1.00-millimetre, the lower bound fracture energy value is 0.021 N/mm. The resulting stress-strain curve, the green line, is almost identical to the average result from the coupon tests, indicated by the black dotted line. The blue line shows that a fracture energy input of twice the lower bound value results in a doubling of the area under the stress-strain curve. When the element size is increased to 2.50 by 2.50-millimetre, the lower bound value of 0.052 N/mm is not returning the predicted results. A slight increase to 0.053 N/mm, a change of less than 2%, provides the desired outcome. Table 4.3 shows the difference between the fracture energy input values and numerical results.

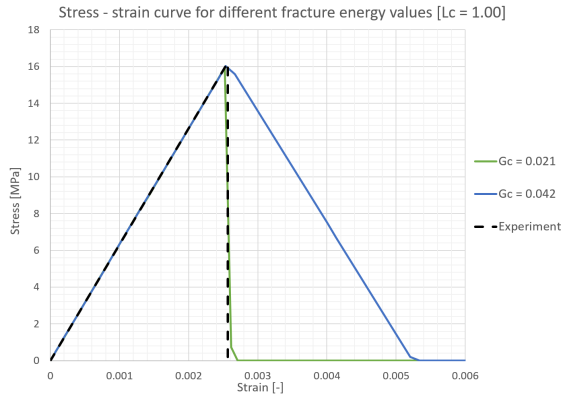


Figure 4.17: UDT90 stress-strain curve with different fracture energy values and an element size of 1.00 mm

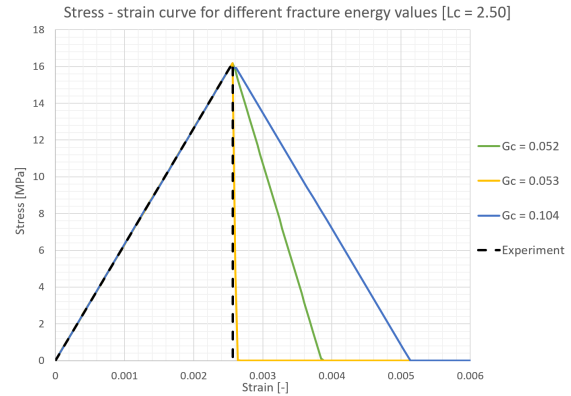


Figure 4.18: UDT90 stress-strain curve with different fracture energy values and an element size of 2.50 mm

The numerical determined fracture energy value for the larger element size is slightly higher than the model input value. In some cases, Abaqus/Standard returns incorrect results for fracture energy values below the lower bound. Abaqus/Standard calculates the minimal required fracture energy based on the ultimate strength and failure strain of the material, which are computed with incremental steps. The required fracture energy is also dependent on the element’s actual characteristic length, which is the square root of the area. When the plate deforms even the slightest, the characteristic length will change, which results in a higher or lower value for the lower bound. The original value of 0.052 N/mm was below the lower bound value, and the resulting stress-strain curve was inaccurate. This behaviour is explained more in detail in subsection 4.1.7.

	σ_c (N/mm ²)	ϵ_0 (-)	L_c (mm)	G_c (N/mm)	Difference (%)
Input	16.21	0.002567	1.0	0.021	
Output	15.93	0.002522	1.0	0.020	-4.32%
Input	16.21	0.002567	2.5	0.05200	
Output	16.19	0.002572	2.5	0.05204	0.08%
Input	[increase fracture energy by 2%]			0.05300	
Output	16.18	0.002561	2.5	0.05179	-2.29%

Table 4.3: UDT90: difference between the lower bound fracture energy (input) and numerical stress-strain area (output)

4.1.6. Models loaded in compression

The numerical process is repeated for the models loaded in compression. Figure 4.19 and 4.20 show the stress-strain curves for the model loaded in compression in the longitudinal direction with different fracture energy input values, with an element size of 1.00 and 2.50 millimetre, respectively. In both cases, the lower bound fracture energy values return the expected stress-strain curves, and a doubling of the input value results in a doubling of the area under the stress-strain curve. Table 4.4 shows that the input lower bound fracture energy is larger than the numerical fracture energy for both element sizes.

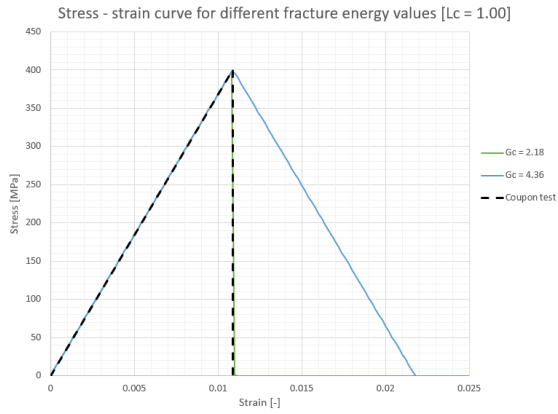


Figure 4.19: UDC0 stress-strain curve with different fracture energy values and element size of 1.00 mm

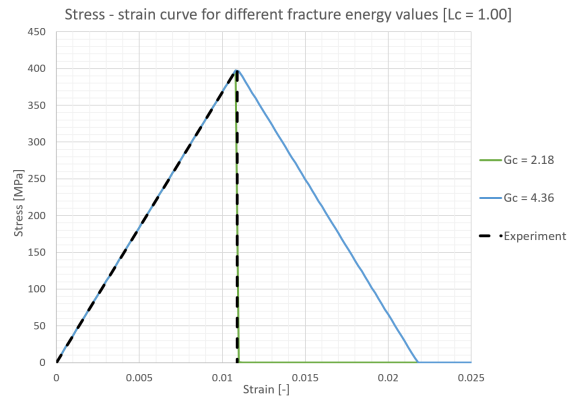


Figure 4.20: UDC0 stress-strain curve with different fracture energy values and element size of 2.50 mm

	σ_c (N/mm ²)	ϵ_0 (-)	L_c (mm)	G_c (N/mm)	Difference (%)
Input	400.67	0.0109	1.0	2.18	
Output	397.6093	0.0108	1	2.15	-1.52%
Input	400.67	0.0109	2.5	5.45	
Output	397.61	0.0108	2.5	5.37	-1.52%

Table 4.4: UDC0: difference between the lower bound fracture energy (input) and numerical stress-strain area (output)

For the two models loaded in compression in the transverse direction, the experimentally determined lower bound values do not return the desired outcome, as shown by the green lines in figure 4.21 and 4.22. The first figure demonstrates the stress-strain curve for a characteristic element length of 1.00 millimetre and the second figure for a characteristic element length of 2.5 millimetres. In both cases, the stress does not drop-down immediately after damage is initiated. When the lower bound values are slightly increased, the expected stress-strain curves are obtained.

Table 4.5 demonstrates that for both element sizes the experimentally determined lower bound input value is less than the numerically determined area under the stress-strain curve. When the input values are increased to be larger than the output area, the resulting stress-strain curves are as expected. Subsection 4.1.7 gives an indepth explanation for the unexpected outcome. For the model with an element size of 1.00-millimetre, the fracture energy needs to increase from 0.480 to 0.484 N/mm. For the element size of 2.50-millimetres, an increase from 1.20 to 1.21 N/mm is needed. In both situations, this is an increase of less than 1%.

	σ_c (N/mm ²)	ϵ_0 (-)	L_c (mm)	G_c (N/mm)	Difference (%)
Input	95.960	0.0100	1.0	0.480	
Output	95.947	0.0101	1.0	0.485	0.99%
Input	[increase fracture energy by 1%]			0.484	
Output	95.957	0.0100	1.0	0.480	-0.87%
Input	95.960	0.0100	2.5	1.200	
Output	95.947	0.0101	2.5	1.211	0.99%
Input	[increase fracture energy by 1%]			1.210	
Output	95.954	0.0100	2.5	1.199	-0.87%

Table 4.5: UDC90: difference between the lower bound fracture energy (input) and numerical stress-strain area (output)

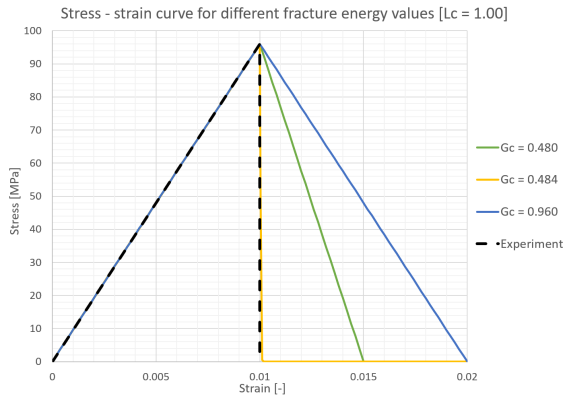


Figure 4.21: UDC90 stress-strain curve with different fracture energy values and element size of 1.00 mm

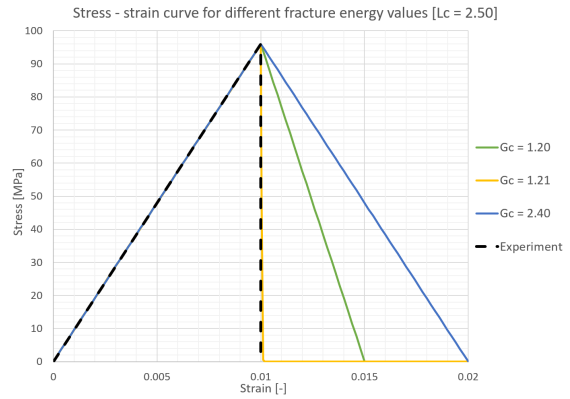


Figure 4.22: UDC90 stress-strain curve with different fracture energy values and element size of 2.50 mm

4.1.7. Fracture energy input below the lower bound value

In some cases, the stress-strain curve showed a gradual stress decrease after damage initiation, instead of the expected abrupt drop in strength. To analyse this behaviour, a range of low fracture energy input values is applied to the first model. This model was given a positive displacement in the direction of the fibres. The characteristic element length is 1.0 millimetres, and the experimentally determined lower bound fracture equals 8.45 N/mm.

The expected outcome from the stress-strain curves would be a straight drop-down after damage is initiated, as a low fracture energy value equals a small capacity to absorb the energy before damage of the material. Contrary to this expectation, figure 4.23 shows that input values below the lower bound value return a gradual stress decrease after damage is initiated. The stress-strain curve widens, similarly as it does for fracture energies values higher than the lower bound value. Figure 4.24 demonstrates that fracture energy input values below and above the lower bound value return the same stress-strain curves. This behaviour occurs because Abaqus/Standard is programmed to automatically increase the fracture energy input when this value is below the lower bound value it numerically determines from the elastic failure behaviour. When this increase does not occur, and the input value is too low, numerical issues can occur.

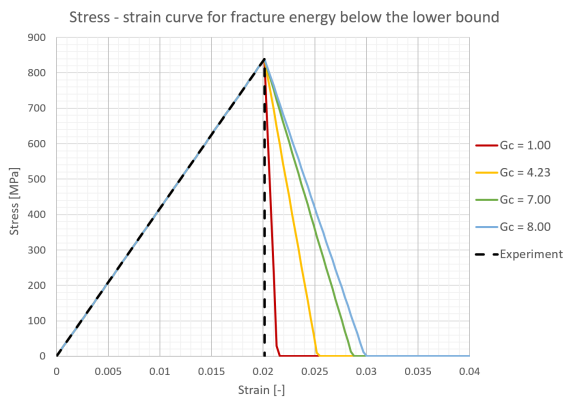


Figure 4.23: UDT0 stress-strain curve with fracture energy values below the lower bound and an element size of 1.00 mm

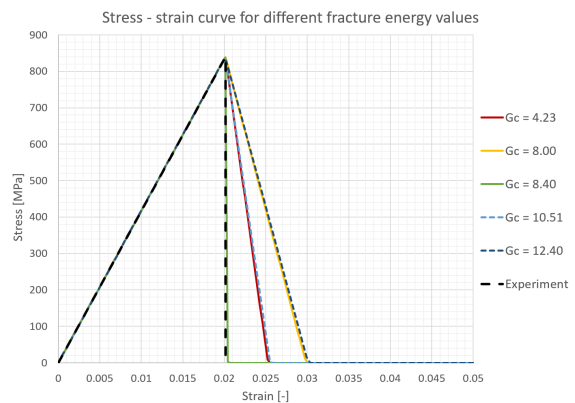


Figure 4.24: Different fracture energy values result in the same stress-strain curves before coefficient is updated

4.1.8. Larger mesh size

To verify if the equivalent displacement theory also applies to larger mesh sizes, the mesh size of the model is increased. The plate loaded in uniaxial tension is modelled with a mesh size of 5.00 and 25.00 millimetres. The resulting stress-strain curves are shown in figure 4.25 and 4.26. As can be seen, the curves deviate from the expected result, which is indicated by the black dotted line. For elements larger than 2.50 millimetres, a lower fracture value input is needed to obtain the desired stress-strain curve. Figure 4.27 demonstrates the relation between the fracture energy input and the area under the curve for element sizes up to 25.00 millimetres.

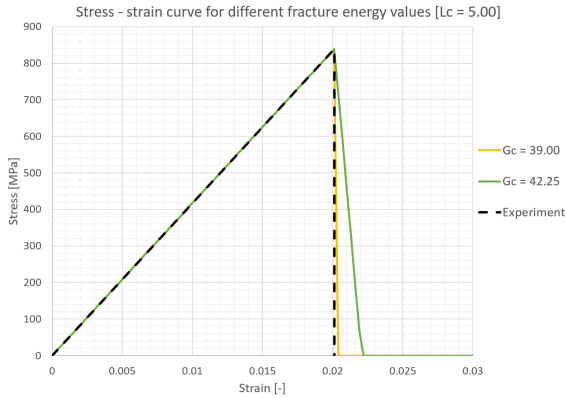


Figure 4.25: Stress-strain curves of an UDT0 plate with element size of 5.00 mm

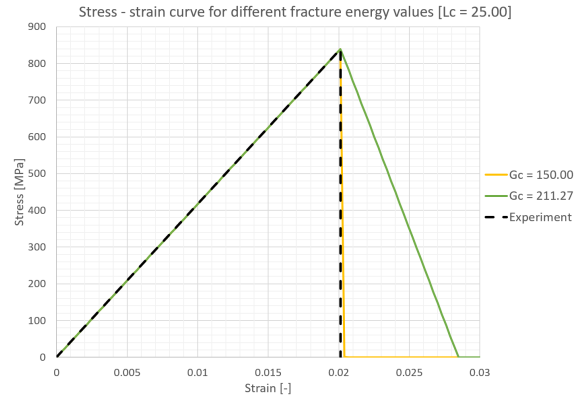


Figure 4.26: Stress-strain curves of an UDT0 plate with element size of 25.00 mm

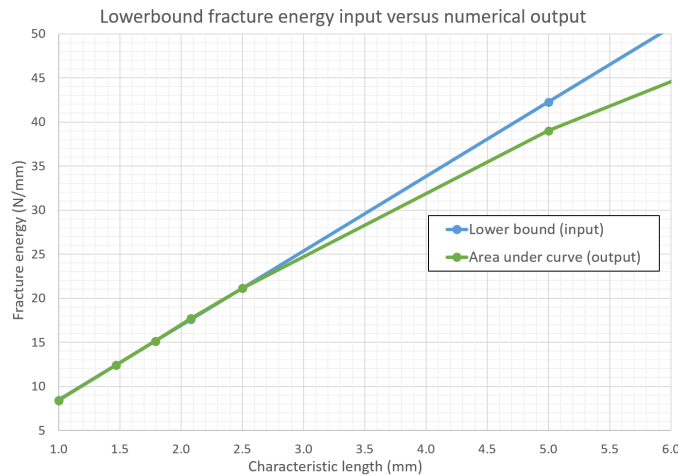


Figure 4.27: Fracture energy lower bound values (input) versus the area under the curve (output)

The reason for this behaviour could be the low number of elements in the model. To validate this statement, the area of the plate is increased, as shown in figure 4.28 and 4.29. For an element size of 25.00 millimetres and fracture energy input equal to the lower bound value, three of the four resulting stress-strain curves show the abrupt drop in stress when the material’s ultimate strength is reached.

In the case of tension in the longitudinal direction, a slight decrease of 3.2% of the fracture input yields a better result. In this case, the mesh size could be too large to accurately capture the damaged area or the incremental step size is too large to accurately determine failure properties. For the models loaded in tension in the transverse direction and compression in the longitudinal direction, the lower bound value gives the desired result. A small increase is needed to improve the plate’s stress-strain output for the model under compression loading in the transverse direction. For this situation, it seemed that the fracture energy input is too low, as discussed in section 4.1.7.

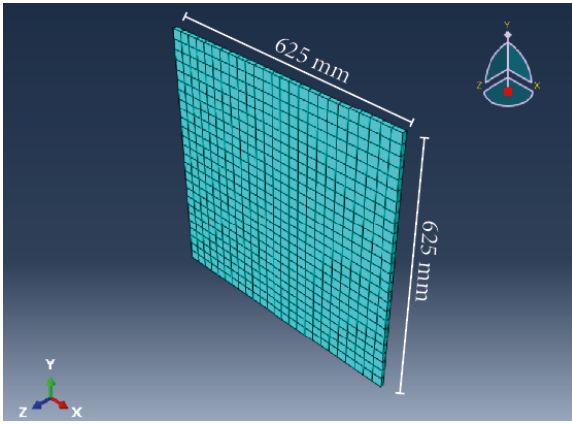


Figure 4.28: Mesh size of 25.00 by 25.00 mm for tension models

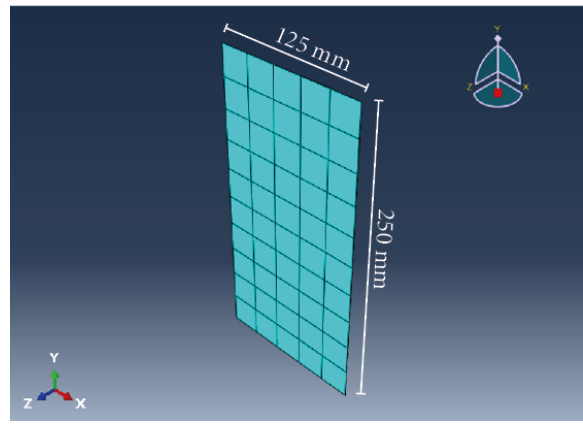


Figure 4.29: Mesh size of 25.00 by 25.00 for compression models

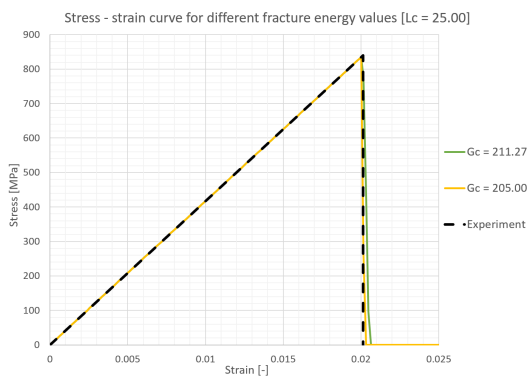


Figure 4.30: Stress-strain curve UDT0 for fracture energy related to the lower bound value

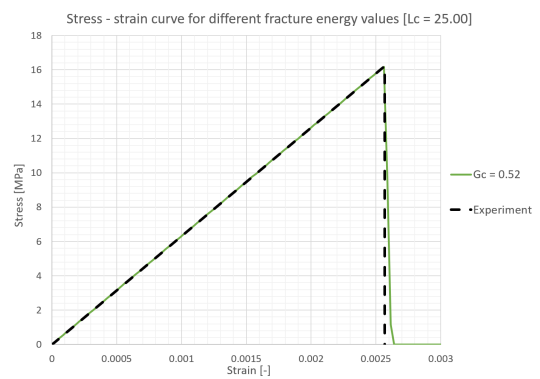


Figure 4.31: Stress-strain curve UDT90 for different fracture energy values

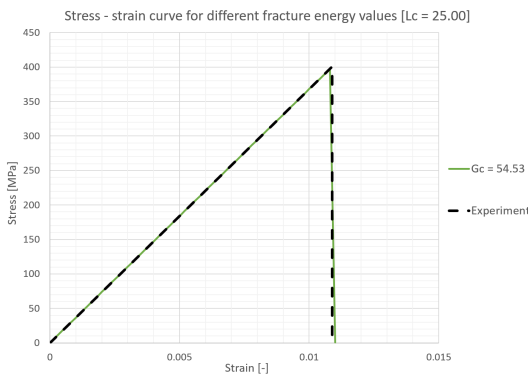


Figure 4.32: Stress-strain curve UDC0 for fracture energy related to the lower bound value

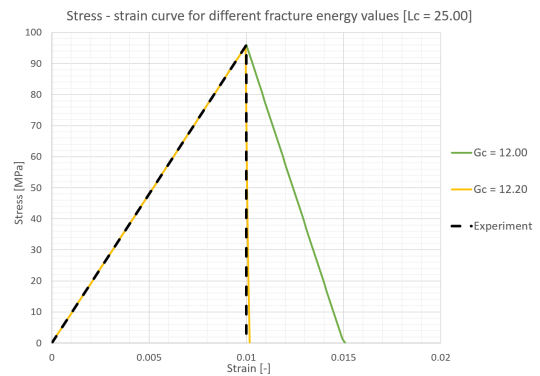


Figure 4.33: Stress-strain curve UDC90 for different fracture energy values

4.2. Conclusions

The fracture energy of a material can be approximated from flat coupon experiments, as it equals the area under the stress-strain curve. To model the damage behaviour of FRP material with the Hashin damage criteria, the fracture energy is required as an input parameter to describe the damage evolution of the material. The fracture energy does not influence the elastic failure behaviour of the material. Due to large scatter in the experimental data, the post-failure behaviour of the coupon could not be determined. Instead, the lower bound value is used, which is determined from the strength of

the material and the strain at damage initiation. The lower bound value equals an abrupt drop after the strength of the material is reached. The lower bound fracture energy is a conservative option for modelling failure of a material, abrupt failure means that there is no post-failure load carrying capacity in the material. However, when the actual fracture energy of the material is lower than the determined lower bound value, the fracture toughness of the material is overestimated.

Implementing the lower bound value in the numerical models should, in theory, result in this abrupt drop after damage initiation. In practice, this was not always the case. Abaqus/Standard calculates the minimal required fracture energy based on the material's ultimate strength and failure strain, which are computed with incremental steps. When the increment step is too large, it can underestimate the material's stress and calculate that more fracture energy is left for the progression of damage.

The required fracture energy is also dependent on the element's actual characteristic length, which for a shell element is the square root of the area of the element. Deformation of the elements can lead to a change in the characteristic element length—consequently, the energy required to reach failure increases or decreases. Abaqus/Standard is programmed to increase the implemented fracture energy when the input value is below the numerical lower bound value to prevent modelling issues. This increase results in a more gradual decrease in stiffness and strength, which means that a low fracture value input is not always a conservative solution. Adding a minimum of two % to the fracture energy lower bound value prevented this problem.

5

Multi-directional model

A common type of fibre-reinforced polymer structures are laminates: multiple uni-directional layers with different fibre directions stacked together. In this chapter, three GFRP multi-directional (MD) flat coupon experiments are modelled with Abaqus/Standard to determine if lower bound fracture energy can be used for progressive failure analysis.

5.1. Multi-directional coupon tests

Similar to the uni-directional flat coupon experiments modelled in the previous chapter, three MD-coupon experiments will be created with Abaqus/Standard. The MD-coupon tests were performed and reported in the paper "Pin Bearing in Glass fiber-Reinforced Polyester" (Cornelissen, 2020). This paper can be consulted for an elaborated version of the test methods and results. The MD coupons consist of the same material as the UD coupons. Multiple plies with different fibre directions are stacked together. The lay-up of the laminate is $[90/0_3/45/-45/0_2]_s$, which is schematically shown in figure 5.1. This lay-up results in a distribution of 62.5% of the fibres in the 0° -direction, and the other directions each account for 12.5% of the fibres. The 0° -direction is indicated as the primary fibre direction or x-direction.

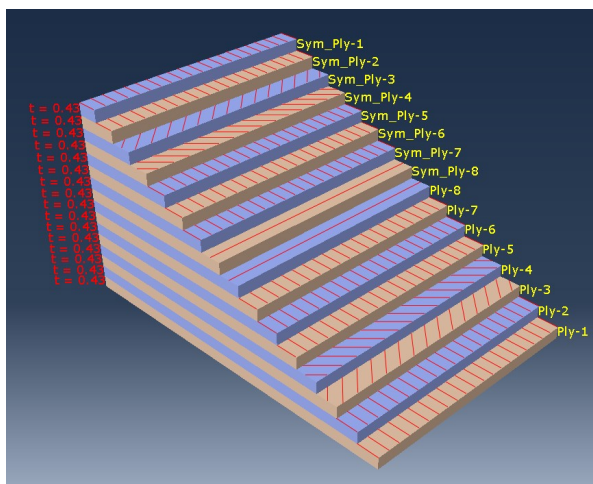


Figure 5.1: Lay-up of the multi-directional laminate

The coupon tests are performed for each failure mode. Seven specimens were manufactured for each test. The specimens were loaded until material failure, with the testing procedures performed as described in ISO527-1 and ISO527-5 (Normcommissie:310061, 2012). The tabs, used to facilitate load introduction from the clamps of the test machine onto the material, are a glass-fabric/polyester

laminate bonded to both flat surfaces of the coupon at two opposite edges. The tests for the coupons loaded in compression in the longitudinal direction failed, and no results are available. For the coupons loaded in tension, the engineering strain was measured by a clip-on extensometer that determined the displacement over the gauge length. The surface of the coupons loaded in compression was too small to fit an extensometer, and the strains were measured with Digital Image Correlation (DIC). The tests were performed on the Schenk 600 kN test machine in the TU Delft Stevin II Laboratory in a dry environment at room temperature. The tensile and compressive test specimens' geometry is in agreement with ISO527-5 and ISO14126 (Normcommissie:310061, 1999), respectively, and presented in figure 5.2 and 5.3.

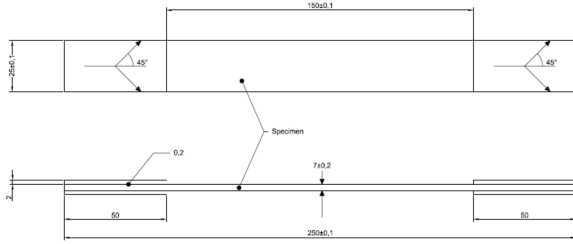


Figure 5.2: Coupon geometry for 0° and 90° tensile testing (ISO527-4 type 3)

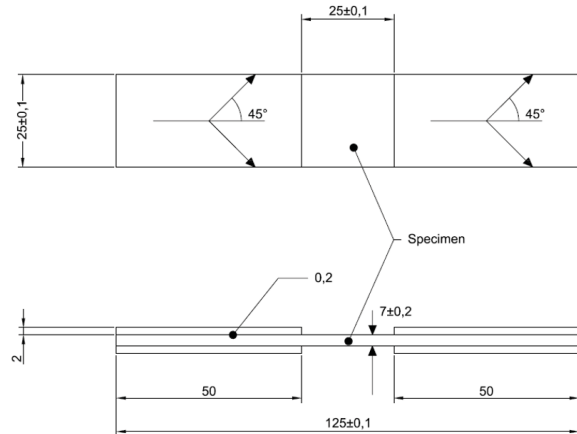


Figure 5.3: Coupon geometry for 0° and 90° compressive testing (ISO14126 type B2)

5.1.1. Modelling approach

The first choice for the model was a stacked continuum shell model with cohesive zone modelling (CZM) because it has been demonstrated that this method is able to capture the failure behaviour of FRP in good agreement with the test results Csillag et al. (2019). However, the solver failed to reach the ultimate strength, as shown in Appendix B, figure B.4. In implicit analyses, as used in Abaqus/Standard, strain-softening of materials often leads to convergence issues. For this reason, instead of a stacked shell approach with CZM, the laminate was modelled with continuum shell elements and one continuum shell element in the through-thickness direction.

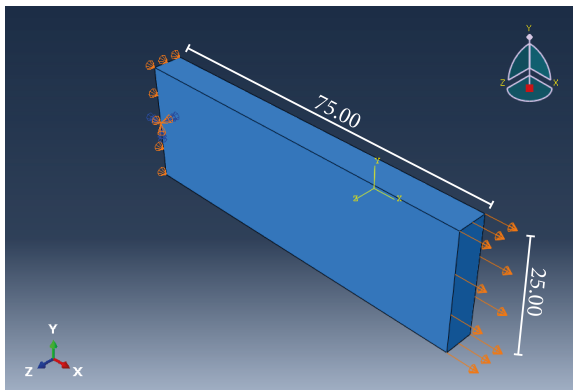


Figure 5.4: Geometry of the model for tensile loading

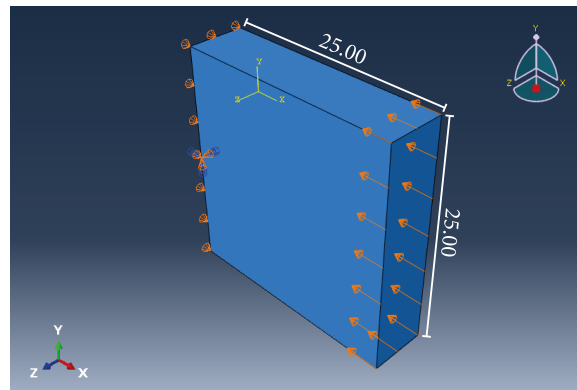


Figure 5.5: Geometry of the model for compressive loading

The geometry and the boundary conditions for the models are shown in figures 5.4 and 5.5. The width of the coupons loaded in the longitudinal direction is 25 millimetres, and the clip length between the test tabs is 150 millimetres. Due to symmetry, the length and width of the finite element model are 75.00 by 25.00 millimetres. For the coupons loaded in compression, the clip length is 25.00 millimetres, which is equal to the plate's width. The dimensions of the model are the same. The compression- and

tension-loaded models have equivalent boundary conditions. A displacement is applied to one face of the laminate, with the global positive x-axis as normal. The opposite face constrains displacement in the x-direction and consists of one nodal point where all rotations and displacements are zero. These boundary conditions are chosen to allow displacement for the non-loading directions to prevent unrealistic stress concentrations in the model. The coupons are modelled with an SC8R mesh: an 8-node quadrilateral in-plane general-purpose continuum shell with reduced integration with hourglass control and finite membrane strains. Element stiffness degradation is set at a value of 1, which means that an element is removed from the mesh if all integration points reach the maximum stiffness degradation value of 1. In the case of tensile loading, none of the integration points is in compression. Static general analysis is performed.

5.1.2. Material properties

Plies, from the same material as the UD-coupons in chapter 4, are stacked together in different directions to create the MD-laminate. The material properties of this laminate have thus the same properties as the UD plies. Table 5.1 states the material properties that are obtained from the four different UD-coupon models. The stiffness properties in tension and compression for both directions differ. For the input properties of the MD models, the average stiffness is used, which is shown in table 5.2.

	σ (MPa)	E (MPa)	ϵ (-)
T0	839.53	41700	0.0201
T90	25.17	9634	0.0026
C0	413.06	37939	0.0109
C90	95.98	9634	0.0100

Table 5.1: Material properties of the UD-models

	σ (MPa)	E (MPa)	ϵ (-)
T0	839.53	39820	0.0211
T90	25.17	9634	0.0020
C0	413.06	39820	0.0104
C90	95.98	9634	0.0120

Table 5.2: Material properties of the MD-models

5.2. Test results

MD-coupon models are created for three of the four failure modes: the three coupons for which the MD-coupon experiments succeeded. These are tensile loading in the longitudinal and transverse direction and compressive loading in the transverse direction. The average result of each set of experiments is compared with the numerical results obtained from the Abaqus/Standard models.

5.2.1. Lower bound fracture energy

Similar to the UD-coupon tests, the MD-coupon tests did not provide enough accurate data about the post-failure behaviour. The modelled post-failure behaviour is limited to the abrupt failure when the plate reaches its ultimate strength. The lower bound fracture energy value is implemented to verify the predicted drop in strength and significant stiffness degradation after the material strength of the plate is reached. As determined, this fracture energy depends on a characteristic length, which is equal to the length of the element for a continuum shell element. Numerical issues occurred for the UD-coupon models, which led to inconsistent output. These issues occurred when the fracture energy input was below the model's lower bound fracture energy value. It was established that to prevent this behaviour, the lower bound fracture energy value needed to be increased by at least 2%. For the MD-coupon models, the lower bound fracture energy value was increased by 5% and 10% to verify that an increased lower bound value would not change the expected outcome and thus be a reliable method for progressive failure analysis.

5.2.2. MDT0 model

Figure 5.6 shows the results of seven MD-coupon experiments under longitudinal tensile loading obtained from the before mentioned report (Cornelissen, 2020). The jump in the strain level near the point of failure indicates that one or multiple plies have failed, but the damage zone is outside the extensometer's range. From this jump, the strength and failure strain of each coupon is determined.

The black dotted line presents the average stress-strain curve of the coupon test. The following figure 5.7 shows the results of the numerical model. Four different plots are visible.

- The black dotted line is the average stress-strain curve obtained from figure 5.6;
- The blue line shows the numerical result with the UD-coupon material properties as stated in table 5.2;
- The orange line shows the numerical result for the MD-material properties and the lower bound fracture energy
- The yellow line shows the numerical result for the MD-material properties and an increased fracture energy value of 5%;
- The green line shows the numerical result for the MD-material properties and an increased fracture energy value of 10%.

The results with the material properties from the UD-coupon models differ from the test results, as shown by the blue line in figure 5.7. The decreased strength of the MD-coupon experiments could be explained due to an incorrect set-up of the boundary conditions or due to corner effects. A difference in volume fraction between the UD- and MD-coupons can cause an increase in stiffness: a higher volume fraction results in a higher stiffness. The input values are adjusted to obtain a numerical result in agreement with the experimental results, as shown by the orange line. Table 5.3 states the UD-values that were implemented for the first model and the MD-values, were the strength is decreased.

	σ_{FT} (MPa)	E_1 (MPa)	ϵ_{FT} (-)
UD-values	839.53	39820	0.0211
MD-values	705.41	47000	0.0144

Table 5.3: Original (UD-values) and updated material properties (MD-values) for MDT0-coupon model

After decreasing the strength and increasing the stiffness of the laminate, failure of the fibres occurs around 1.4% strain. Around 0.35%, a small change in the slope can be seen, where the matrix fails in tension. The stress-strain curve is similar compared to the average experimental results. The material strength is around 460 MPa, and when this strength is reached, a significant drop in stress and stiffness can be seen. A slight increase in the fracture energy of 5% and 10% returns approximately the same result. After the failure of the coupon, a small amount of stiffness remains, and abnormal strain hardening occurs. For Abaqus to consider the complete loss of the material's stiffness, every ply of the laminate needs to fail. Even though the plies loaded in the longitudinal direction fail, as can be seen by the peaks at 0.35% and 1.4% strain, some plies in the other direction continue to carry the loading.

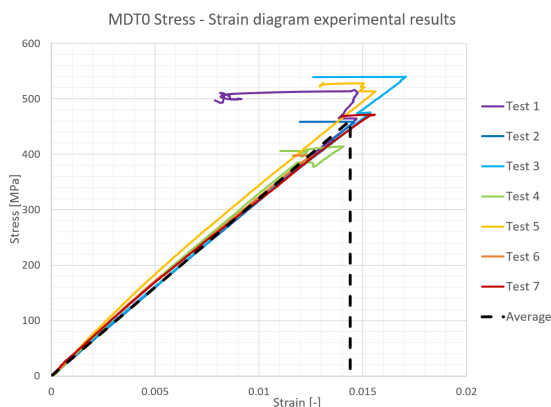


Figure 5.6: Stress-strain curves for the test results from the MDT0-coupon tests and their average value

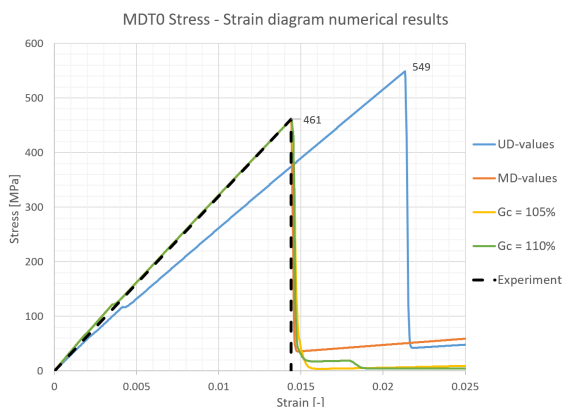


Figure 5.7: Stress-strain curves of the numerical results for the MDT0-coupon

5.2.3. MDT90 model

Six of the seven specimens, loaded in tension in the transverse direction, resulted in a proper stress-strain curve, shown in figure 5.8. One of the specimens failed, and no data was obtained. At around 0.2% strain, a kink can be observed in the curves. This kink corresponds with the failure strain of a UD-ply loaded in transverse tension. Failure of these plies results in a stiffness loss in the laminate, corresponding to the graphs' change in slope. Around 2.1%, failure of the fibres in the longitudinal direction is indicated, resulting in the complete failure of the coupons. The numerical results in figure 5.9 show roughly the same behaviour. The model with the original UD-values, stated in table 5.4, has a kink around 0.2% and fails at 2.1% strain. For the updated values displayed in the same table, equivalent kinks occur, slightly shifted to the right of the graph.

	σ_{FT} (MPa)	E_1 (MPa)	E_2 (MPa)	ϵ_{FT} (-)	ϵ_{MT} (-)
UD-values	839.53	39820	7976	0.0211	0.0020
MD-values	995.53	42500	9634	0.0234	0.0026

Table 5.4: Original (UD-values) and updated material properties (MD-values) for MDT90-coupon model

A curvature in the coupons can explain the difference in strength and transverse stiffness between the numerical and the test results. FiberCore Europe, the producer of the coupons, noted a curvature in the plates due to thermal effects during infusion, which affects the measured elasticity, strength and ultimate strain. In addition, the UDT90-coupons did not have the correct geometry for testing at 90°. The coupons' width was different, which could lead to edge effects influencing the material properties obtained from these tests.

The updated stiffness is the same as for the UD-coupons under compressive loading in the transverse direction. Similar to the MDT0-model, a remaining stiffness is apparent. Due to the large drop in stiffness, the coupon is considered to have failed. The model with the updated properties and the 5% and 10% increase in fracture energy show the same kink at 0.2% strain, with a change of slope and failure around 0.023% strain. After the strength of the material was reached, the expected abrupt drop in stress can be noted.

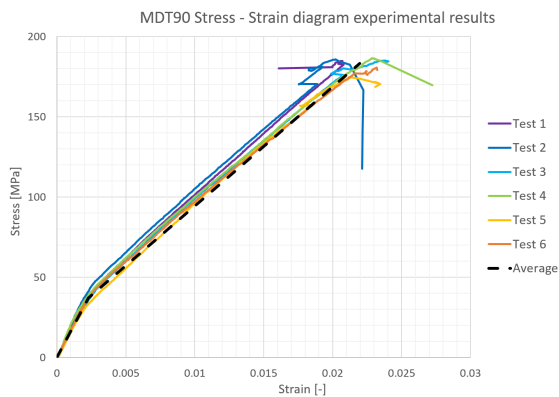


Figure 5.8: Stress-strain curves for the test results from the MDT90-coupon tests and their average value

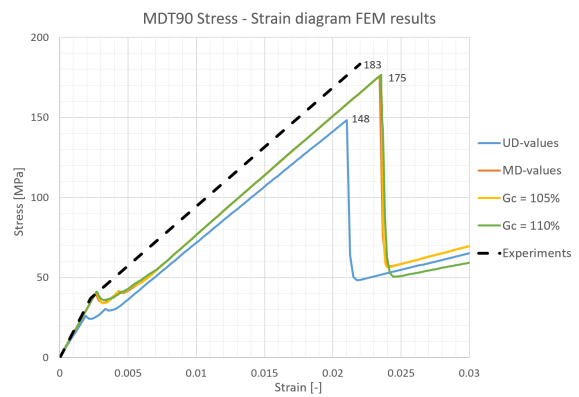


Figure 5.9: Stress-strain curves of the numerical results for the MDT90-coupon

5.2.4. MDC90 model

The third set of specimens was loaded in compression in the transverse direction. The UD-coupons' material properties result in a stress-strain curve with lower ultimate stress than the average experimental results. Additionally, around 0.012 % strain, the plies loaded in compression in matrix direction fail. The transverse strength properties are increased proportionally. The previously mentioned curvature of the coupons can explain the lower material strength of the UD coupons. After updating the material properties, both the fibres and the matrix in compression fail around a strain of

1%. Furthermore, figure 5.11 also shows residual stiffness for each of the models. This lower bound fracture energy is increased with 5% and 10% to provide some certainty. The returned stress-strain curves are as expected: a large drop-down when the plies in the transverse direction fail. The analysis with increased fracture energy shows a slightly more gradual stress decrease. The material's ultimate strength remains the same, and the fracture energy increase does not significantly affect the test results.

	σ_{FC} (MPa)	σ_{MC} (MPa)	E_1 (MPa)	E_2 (MPa)	ϵ_{FC} (-)	ϵ_{MC} (-)
UD-values	413.06	95.98	39820	7976	0.0104	0.012
MD-values	425.89	111.56	41700	9634	0.0102	0.0102

Table 5.5: Original (UD-values) and updated material properties (MD-values) for MDC90-coupon model

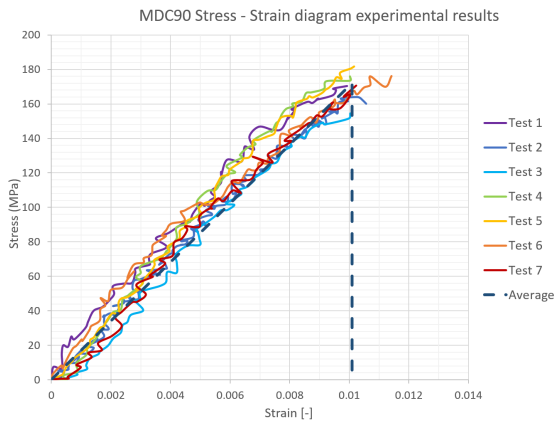


Figure 5.10: Stress-strain curves for the test results from the MDC90-coupon tests and their average value

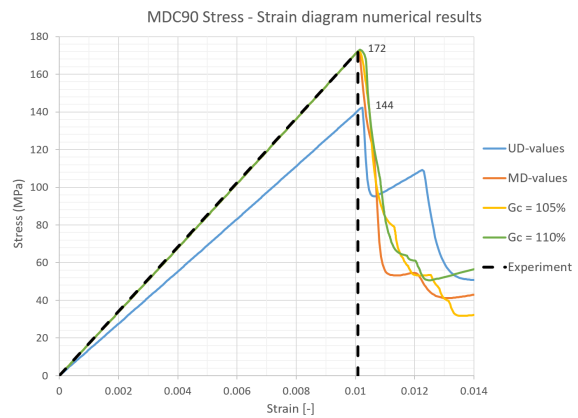


Figure 5.11: Stress-strain curves of the numerical results for the MDT90-coupon

5.2.5. Difference in material properties between UD- and MD-coupons

The numerical results for the MD-coupon tests were different compared to the experimental results. The tensile strength in the direction of the fibres needed to be decreased for the MDT0-model and increased for the MDT90-model. For the final laminate, the result from the UD-coupon test is used, as it is roughly the average value as used for the MDT0- and MDT90-model. The rest of the MD coupons has a slight strength increase ranging between 1% and 4%.

		MDT0	MDT90	MDC90	Average
UDT0	σ_{T0}	-16%	19%		1%
UDT90	σ_{T90}		1%		1%
UDC0	σ_{C0}			3%	3%
UDC90	σ_{C90}			4%	4%
UDT	E_1	15%	6%	5%	9%
UDC	E_2		17%	19%	18%

Table 5.6: Strength and stiffness difference between UD-coupons and MD-coupons

A possible explanation could be the curvature of the UD-coupons, while the MD-coupons remained flat. This curvature was most noticeable for the specimen oriented in the 90-degrees. In addition to the curvature, a higher fibre volume fraction of the MD specimens could be the reason for the increased stiffness of the laminate. This increase is an assumption as no additional verification can be performed. Due to the notable curvature of the UD specimens, the choice has been made to apply a slight strength and stiffness increase, except for the tensile strength in the fibres' direction. Uncertainties about the laminate material properties will remain, which is less significant for the non-linear buckling analysis, as for the time being, only numerical analyses will be performed.

5.3. Conclusion

Stacking multiple uni-directional plies on top of each other and varying the direction of the fibres creates a laminate. Experimental coupon tests performed on a GFRP laminate were modelled in this chapter. The properties for the modelled were obtained from the UD models. Even though the MD-coupons were manufactured from the same material as the UD-coupons, the numerical results of the MD models differ from the experimental results.

Curvature issues with the UD specimens which developed during manufacturing, and a possibly increased fibre volume fraction for the MD coupons, could explain the differences. Due to the notable curvature of the UD specimens, the choice has been made to apply a slight strength and stiffness increase, except for the tensile strength in the fibres' direction. The stress-strain curves obtained with progressive failure analysis are in good agreement with the test results. When the material reached the ultimate strength, a significant drop in stress was observed, as expected from implementing the lower bound fracture energy.

The numerical results of the UD-coupon models produced modelling issues, which led to inconsistent output. These issues occurred when the fracture energy input was below the model's lower bound fracture energy value. To prevent this behaviour, it was concluded that the lower bound fracture energy value needs to be increased by at least 2%. For the MD models, the lower bound fracture energy input was additionally increased by 5% and 10% to verify that an increased lower bound value would not change the expected outcome. Similar to the models without an increased lower bound fracture energy value, the numerical results for the increased values showed the expected significant drop in strength and stiffness degradation after the ultimate strength was reached.

6

Component model

6.1. Introduction

In the previous chapter, it has been concluded that progressive failure analysis with lower bound fracture energy returns the expected results: a significant decrease in stress after the material strength has been reached. This chapter aims to extend the previous analysis to determine if the lower bound fracture energy can be used for non-linear buckling behaviour. This is executed by performing progressive ply failure analysis with lower bound fracture energy on experimental buckling tests reported in "Buckling of Imperfect Composite Plates: Parametric Studies" by [Hayman et al. \(2011\)](#).

In the second part of this chapter, progressive failure analysis is used to predict the buckling strength of the GFRP plate studied in chapter 5. The goal is to obtain a buckling curve and analyse the influence of initial imperfections on the strength reduction of a GFRP plate. Different initial imperfection sizes are implemented for varying plate thicknesses, and two types of boundary conditions are applied to study if the boundary conditions change the resulting buckling curve.

6.2. Part 1: Buckling model

A wide-ranging series of studies have been performed for the Network of Excellence on Marine Structures (MARSTRUCT) ([Hayman et al., 2011](#)). One of the studies focused on the buckling behaviour of GFRP plates under in-plane compression loading. For this research, three series of square laminated panels with different initial imperfections were fabricated by two universities: the National Technical University of Athens (NTUA) and the Technical University of Denmark (DTU). In this chapter, two series of plates that are produced by the same university are studied. The material properties of the plates were obtained by a round-robin study in which both universities independently tested the plates. Each plate was clamped in a test rig and uniformly compressed until failure to stimulate buckling of the plates. The test rig was set up to allow displacements in the in-plane direction only; however, some unintentional movement was detected during the buckling tests.

6.2.1. Material

The NTUA produced two series of plates with different thicknesses. The plates are an E-glass/epoxy composite laminate fabricated using a wet lay-up vacuum bag process. The fibre reinforcement consists of 623 g/m² Uni-directional glass fabric, with 50 g/m² in the weft direction, combined with a 306 g/m² ± 45° biaxial, non-crimp fabric and an epoxy resin with low viscosity (600-750) MPa·s at 25°C). The first series is considered as a thin plate with a thickness of 9.7 millimetres and the second series as a mid-thick plate of 15 millimetres. The lay-up for both plates is symmetric:

- Series 1: $[\pm 45 / 0_4 / \pm 45 / 0_3]_s$
- Series 2: $[\pm 45 / 0_4 / \pm 45 / 0_4 / \pm 45 / 0_3]_s$

The area of each plate is 400 by 380 millimetre. After mounting a plate in the test rig, the unsupported area of the plate is 320 by 320 millimetres. The shape of the geometric imperfection is the first buckling mode of a corresponding fully clamped plate. The initial imperfection of the plate is created with a convex mould, numerically machined from an aluminium plate. The glass fibres are placed on top of the mould and impregnated with resin by hand. Both series consisted of 9 plates with three imperfection sizes:

- 3 plates: no imperfection;
- 3 plates: small built-in imperfection of $B/100$, which equals $\delta_0 = 0.01 * 320 = 3.2$ mm;
- 3 plates: large built-in imperfection of $B/33$, which equals $\delta_0 = 0.03 * 320 = 9.6$ mm.

A round-robin material characterisation test programme was performed to determine the material properties of the plates. Both DTU and NTUA tested an UD-specimen created identical to the specimen used during the buckling test. The average ply thickness of this specimen was 0.55 millimetre, with a fibre volume fraction of 0.43. Performed tests determined the tensile, compressive and shear strength and moduli. The tests were performed according to the following standards: ASTM D3039M standard for the tensile properties at 0° and 90° , ISO 14126 for the compressive properties at 0° and 90° , and ASTM D5379 for the shear properties. The two universities had different test equipment at their disposal. Table 6.1 displays the material properties as determined by both universities. The MARSTRUCT study recommended the use of the material properties as determined by the NTUA.

Material property	NTUA test	DTU test
E_{1t}	29658 MPa (11)	33170 MPa (4)
E_{1c}	38671 MPa (3)	37238 MPa (6)
E_{2t}	6563 MPa (23)	9338 MPa (7)
E_{2c}	8501 MPa (14)	9536 MPa (7)
G_{12}	2034 MPa (7)	2169 MPa (22)
ν_{12}	0.290 (37)	0.268 (8)
X_t	559 MPa (21)	698 MPa (10)
X_c	253 MPa (23)	191 MPa (21)
Y_t	60 MPa (20)	43 MPa (14)
Y_c	59 MPa (17)	69 MPa (12)
S	31 MPa (3)	30 MPa (3)

Table 6.1: Average material properties from NTUA test and DTU test

6.2.2. Buckling test set-up

The buckling tests were performed at the DTU with an Instron 8508 5 MN servo-hydraulic testing machine combined with a special test rig. The plates were placed between the side flanges and fixed with bolts between the top and bottom flange. The plate is free to move in the x- and y-direction between the two vertical towers. Out-of-plane displacements and rotations are restricted. The deformations during testing were monitored with an ARAMIS 4M, a non-contact DIC system.

6.2.3. Test-results

All specimens, independent of the size of imperfection, experienced out-of-plane deformations before failure, as was concluded by the DIC out-of-plane measurements. The bending deformations occurred due to a combination of specimen imperfections, test rig deformations and instability or buckling behaviour of the plates. For series 1, a decrease of compressive strength occurs when imperfections are introduced. However, this decrease is almost the same for the small and large imperfection, indicating only a minor imperfection sensitivity. It should be noted that the number of results is too low to give definitive conclusions. For series 2, a consistent decrease in compressive strength can be observed with increased imperfection size. The test rig deformations introduced displacements and rotations of the panel boundaries and created additional geometric imperfections.

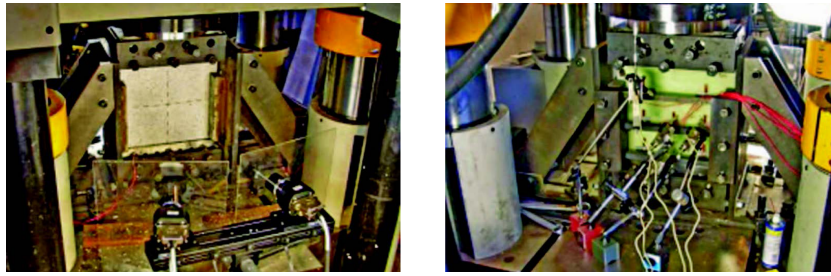


Figure 6.1: The front side (left) and the back side (right) of a plate specimen installed in the test rig, ready for testing (Hayman et al., 2011)

Imperfection (mm)	Series 1 (kN)	Series 2 (kN)
0	N/A	1218
	415	1092
	390	1170
3.2	294	906
	213	882
	309	930
9.6	294	750
	320	780
	N/A	792

Table 6.2: Ultimate failure load for each plate

6.3. Finite element model

The lay-up of series 1 and series 2 is shown in figure 6.2. The 0.36-millimetre thick layer of 45° degrees represents two 0.18 millimetre thick layers of 45° and -45°. A progressive failure analysis using implicit finite element method is performed. The applied number of elements is similar as used in the MARSTRUCT research, where a mesh refinement study was performed, which determined the number of elements to be 46x46 elements for the 320x230 millimetre plates. Table 6.3 states the material properties, the characteristic element length and the numerical values for the fracture energy, which are taken as the lower bound value with an increase of 10%.

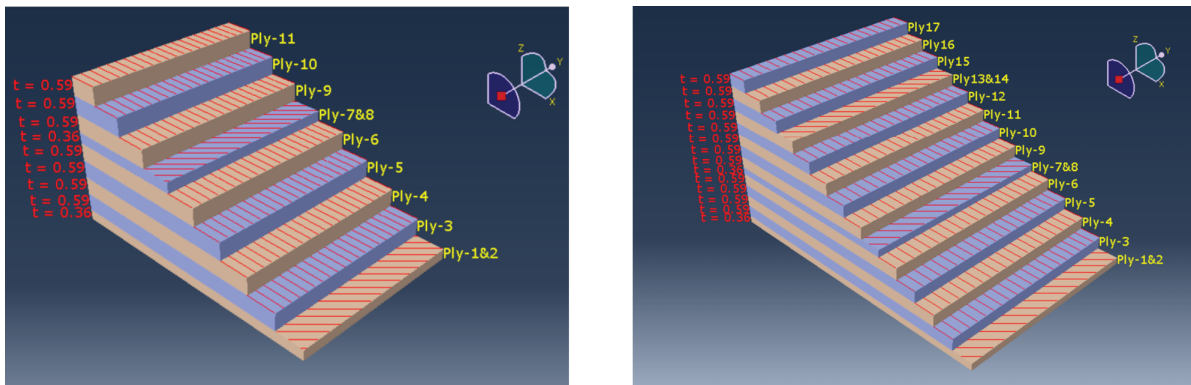


Figure 6.2: Lay-up for series 1 with a thickness of 9.7 mm (left) and lay-up for series 2 with a thickness of 15.14 mm (right)

	$\epsilon_0(-)$	σ_c (N/mm ²)	L_c (mm)	G_c (N/mm)	$G_c + 10\%$ (N/mm)
Longitudinal tensile	0.016	559	6.96	31.81	34.99
Longitudinal compression	0.007	253	6.96	6.52	7.17
Transverse tensile	0.008	60	6.96	1.66	1.83
Transverse compression	0.008	59	6.96	1.61	1.77

Table 6.3: Material properties for the component model, including the lower bound fracture energy value and the lower bound fracture energy value increased by 10%

6.3.1. LBA

Linear buckling analysis is performed to obtain the critical buckling mode shape of the plate with clamped boundary conditions, shown in figure 6.3. The mode shape is scaled to the pre-determined imperfection size and inserted as an initial stress-free imperfect condition, equal to the initial geometric imperfection built into the test panels during fabrication. For the plates without initial imperfections, an imperfection magnitude equal to 5% of the thickness of the plates is implemented to nucleate buckling.

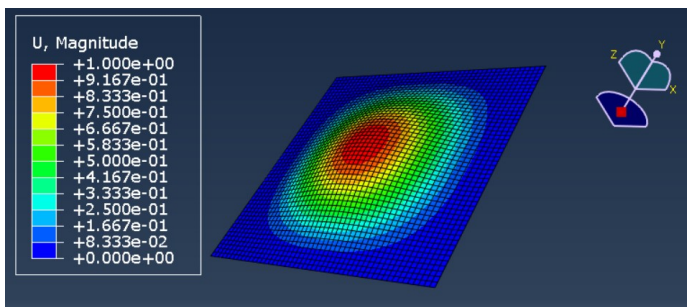


Figure 6.3: Shape of the geometric imperfection

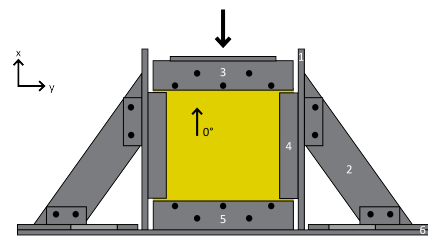


Figure 6.4: Schematization of the test rig (Hayman et al., 2011)

6.3.2. Boundary conditions

Figure 6.4 shows the set-up of the plate. The plate is bolted to the top and bottom of the test rig. On the sides, no bolts are used, which allows for some degree of movement. Compression to the plate is applied from the top. Due to the detected unwanted movement of the plate in the test rig, five different types of boundary conditions are applied to determine an accurate representation of the test set-up. The applied boundary conditions range from a clamped plate with no degree of freedom to a simply supported plate with rotation allowed at the edges and are presented in figure 6.6 up to and including 6.10. Figure 6.5 shows the six degrees of freedom of the conventional shell models. The different boundary conditions also cover the possible horizontal and vertical movement at the sides of the test rig. The numerical model is turned 90 degrees, and a displacement is given from the right side, in the x-direction, instead of from the top as it was done with the test rig.

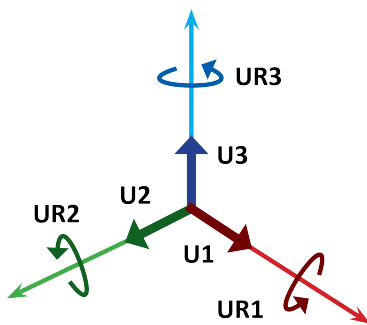


Figure 6.5: Schematic view of the six degrees of freedom

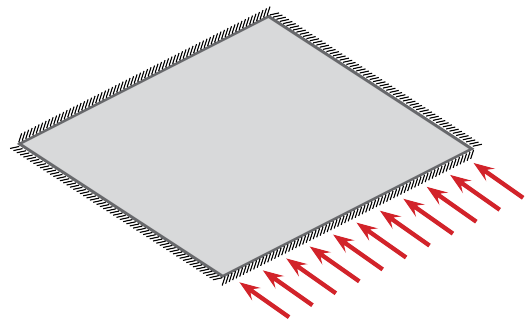


Figure 6.6: Boundary conditions for 'CC/CC'

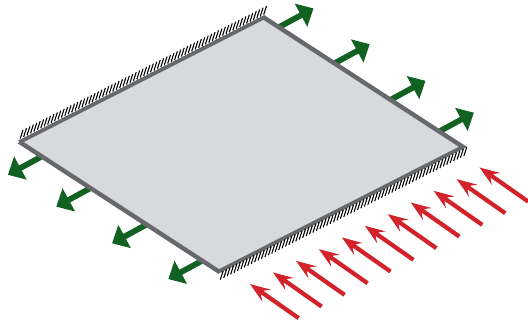


Figure 6.7: Boundary conditions for 'CC/CC, U2=free'

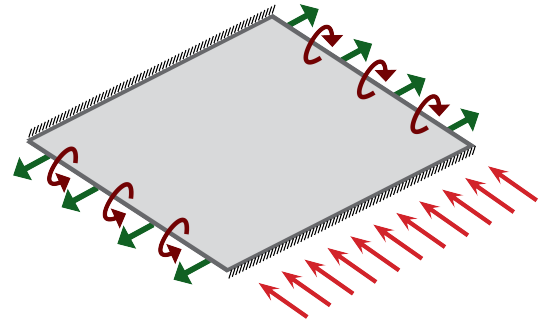


Figure 6.8: Boundary conditions for 'CC/SS, U2=free'

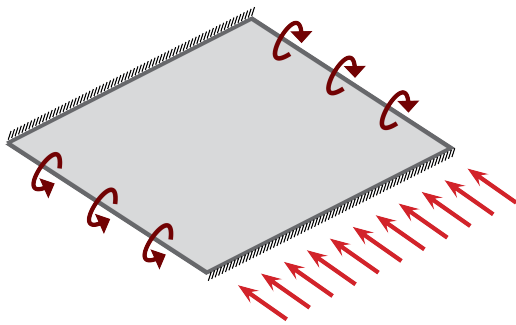


Figure 6.9: Boundary conditions for 'CC/SS'

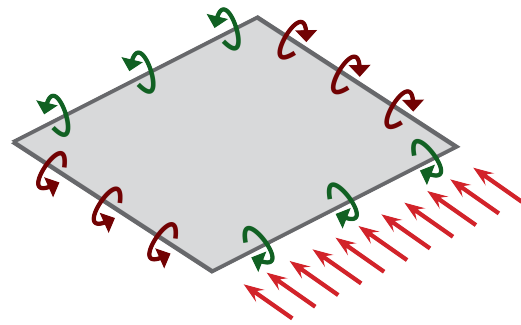


Figure 6.10: Boundary conditions for 'SS/SS'

6.4. Numerical results

The stress-displacement curves for the six different plates are presented in figure 6.11 up to and including 6.21. Series 1 represents the thin plates with a thickness of 9.7 millimetres, and series 2 embodies the mid-thick plates with a thickness of 15.14 millimetre. The end shortening is determined at the side of the plate where the load is applied. All models, independent of the type of boundary condition applied, show a significant drop in strength and large stiffness reduction after the ultimate strength is reached. This abrupt decrease in strength is as expected with the lower bound fracture energy value implemented in the models. The deflection is the out-of-plane deformation at the plate's mid-centre, where the out-of-plane deformation is the largest.

6.4.1. End-shortening and deflection graphs for series 1

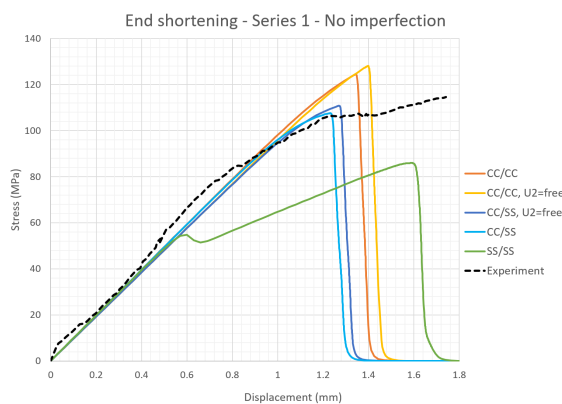


Figure 6.11: Stress-end shortening curves for series 1 with zero imperfection

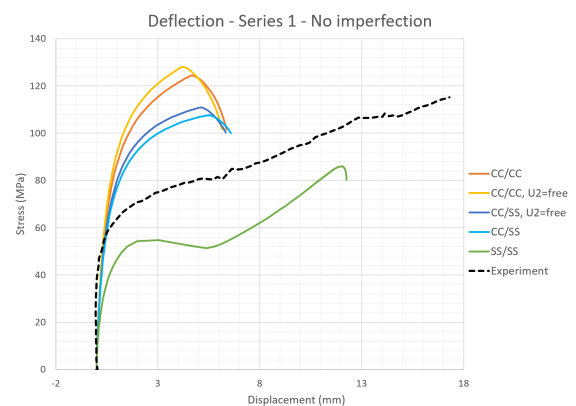


Figure 6.12: Stress-central deflection curves for series 1 with zero imperfection

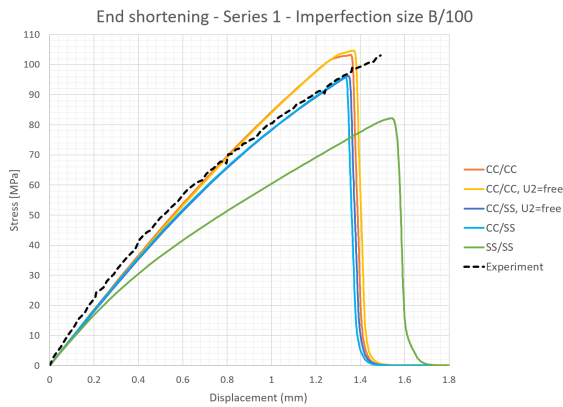


Figure 6.13: Stress-end shortening curves for series 1 with imperfection size B/100

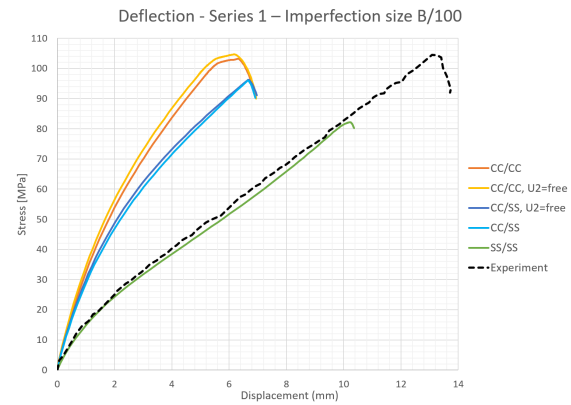


Figure 6.14: Stress-central deflection curves for series 1 with imperfection size B/100

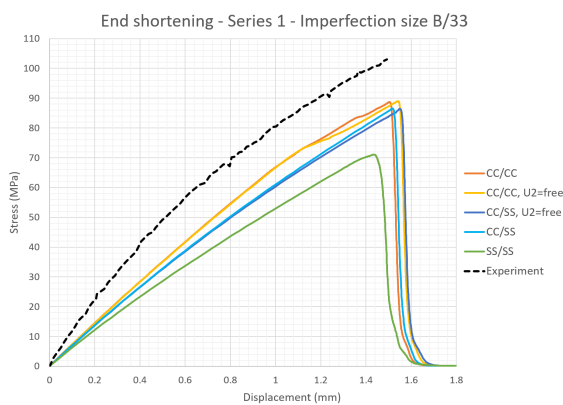


Figure 6.15: Stress-end shortening curves for series 1 with imperfection size B/33

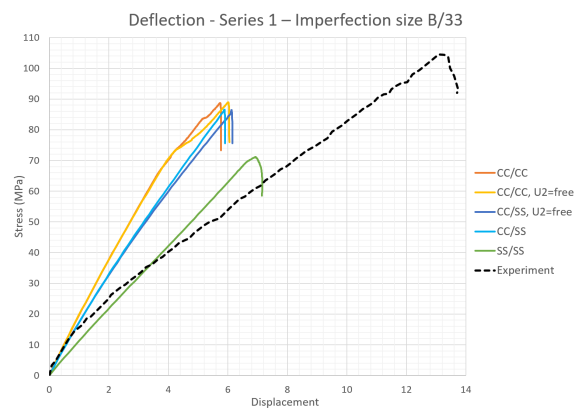


Figure 6.16: Stress-central deflection curves for series 1 with imperfection size B/33

Results for series 1: No imperfection

For the plates with 'no imperfection', an initial imperfection of B/640, which equals an imperfection of 0.5 millimetres, is applied to nucleate buckling. The 'CC/CC' and 'CC/CC, U2=free' models overestimate the ultimate strength by roughly 10%, while the other three models underestimate this value. The 'SS/SS' curve provides the best approximation for the in-plane and out-of-plane displacement.

Model	Maximum stress (MPa)	Difference (%)	In-plane displ. (mm)	Difference (%)	Out-of-plane displ. (mm)	Difference (%)
Test	114.63		1.74		17.31	
CC/CC	124.42	8.5%	1.34	-22.8%	4.67	-73.0%
CC/CC, U2=free	128.06	11.7%	1.40	-19.7%	4.23	-75.6%
CC/SS, U2=free	110.85	-3.3%	1.27	-27.0%	5.12	-70.4%
CC/SS	107.55	-6.2%	1.23	-29.3%	5.51	-68.1%
SS/SS	85.94	-25.0%	1.59	-8.6%	12.06	-30.3%

Table 6.4: Series 1, no imperfection: maximum stress, in-plane displacement and out-of-plane displacement difference between the test results and the Abaqus/Standard model for the five different boundary conditions.

Results for series 1: Imperfection size B/100

An initial imperfection of B/100, which equals 3.2 millimetres, is applied. The 'CC/CC' and 'CC/CC, U2=free' models are a good approximation of the ultimate strength, of which the first one reaches the exact value of 103 MPa. The other models underestimate the ultimate strength by at least 6%.

The overall in-plane displacement is relatively accurate: the first four boundary conditions undervalue the displacement by 10%, and the 'SS/SS' boundary condition overestimates by 3%. All models underestimate the out-of-plane displacement by at least 25%.

Model	Maximum stress (MPa)	Difference (%)	In-plane displ. (mm)	Difference (%)	Out-of-plane displ. (mm)	Difference (%)
Test	103.02		1.49		13.74	
CC/CC	103.21	0.2%	1.36	-9.2%	6.31	-54.1%
CC/CC, U2=free	104.65	1.6%	1.37	-8.2%	6.18	-55.0%
CC/SS, U2=free	96.23	-6.6%	1.35	-9.8%	6.68	-51.4%
CC/SS	96.02	-6.8%	1.33	-10.7%	6.66	-51.5%
SS/SS	82.20	-20.2%	1.54	3.4%	10.23	-25.5%

Table 6.5: Series 1, imperfection size B/100: maximum stress, in-plane displacement and out-of-plane displacement difference between the test results and the Abaqus/Standard model for the five different boundary conditions.

Results for series 1: Imperfection size B/33

An initial imperfection of B/33, which equals 9.6 millimetres, is applied. All models underestimate the ultimate strength, of which 'CC/CC' and 'CC/CC, U2=free' provide the best result with an underestimation of 13%. The 'CC/CC' and 'CC/SS' model have an in-plane displacement difference of only 0.8% and 1.7%, respectively. The other three models have a maximum displacement difference of 4% in the in-plane direction. All boundary conditions underestimate the out-of-plane displacement by at least 50%.

Model	Maximum stress (MPa)	Difference (%)	In-plane displ. (mm)	Difference (%)	Out-of-plane displ. (mm)	Difference (%)
Test	103.02		1.49		13.74	
CC/CC	88.71	-13.9%	1.50	0.8%	5.74	-58.2%
CC/CC, U2=free	88.98	-13.6%	1.54	3.4%	6.01	-56.2%
CC/SS, U2=free	86.45	-16.1%	1.55	4.0%	6.12	-55.4%
CC/SS	86.50	-16.0%	1.52	1.7%	5.89	-57.2%
SS/SS	71.10	-31.0%	1.44	-3.7%	6.93	-49.6%

Table 6.6: Series 1, imperfection size B/33: maximum stress, in-plane displacement and out-of-plane displacement difference between the test results and the Abaqus/Standard model for the five different boundary conditions.

6.4.2. End-shortening and deflection graphs for series 2

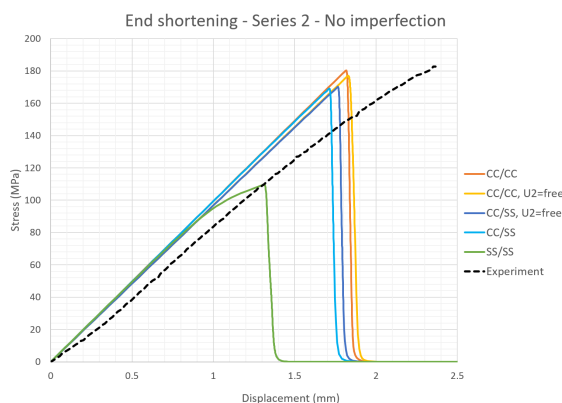


Figure 6.17: Stress-end shortening curves for series 2 with zero imperfection

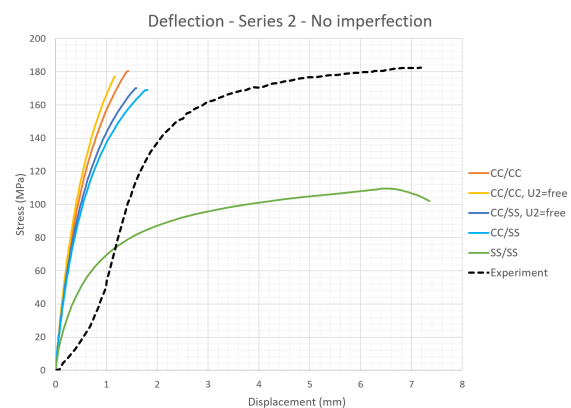


Figure 6.18: Stress-central deflection curves for series 2 with zero imperfection

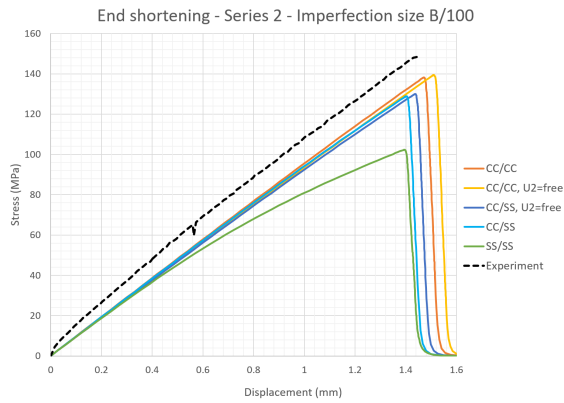


Figure 6.19: Stress-end shortening curves for series 2 with imperfection size B/100

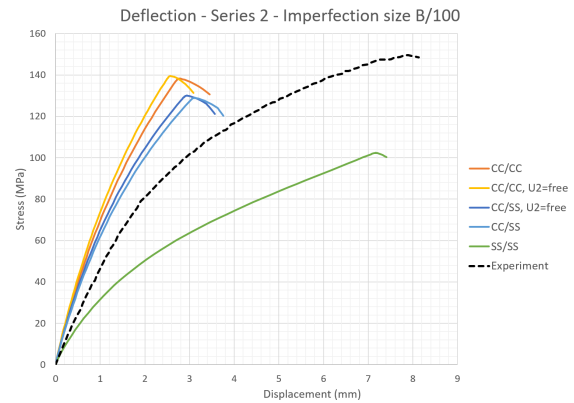


Figure 6.20: Stress-central deflection curves for series 2 with imperfection size B/100



Figure 6.21: Stress-end shortening curves for series 2 with imperfection size B/33

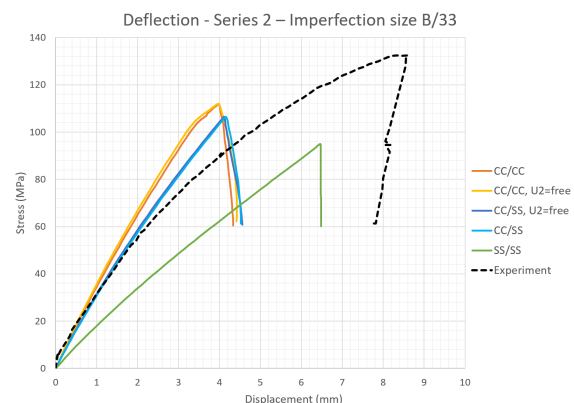


Figure 6.22: Stress-central deflection curves for series 2 with imperfection size B/33

Results for series 2: No imperfection

For the plate without initial imperfections, the 'CC/CC' and 'CC/CC, U2=free' model underestimate the ultimate strength by respectively 1.2% and 3%. The top four boundary conditions in the graph undervalue the out-of-plane displacement by roughly 25%. The 'SS/SS' boundary condition underestimates the out-of-plane displacement by 45%, but this model gives the best approximation for the in-plane displacement, with a difference of 9%.

Model	Maximum stress (Mpa)	Difference (%)	In-plane displ. (mm)	Difference (%)	Out-of-plane displ. (mm)	Difference (%)
Test	182.56		2.36		7.18	
CC/CC	180.29	-1.2%	1.82	-23.2%	1.43	-80.1%
CC/CC, U2=free	177.11	-3.0%	1.83	-22.7%	1.16	-83.9%
CC/SS, U2=free	170.09	-6.8%	1.77	-25.3%	1.59	-77.9%
CC/SS	169.03	-7.4%	1.71	-27.6%	1.79	-75.1%
SS/SS	109.65	-39.9%	1.31	-44.5%	6.52	-9.3%

Table 6.7: Series 2, no imperfection: maximum stress, in-plane displacement and out-of-plane displacement difference between the test results and the Abaqus/Standard model for the five different boundary conditions.

Results for series 2: Imperfection size B/100

An initial imperfection of B/100, which equals 3.2 millimetres, is applied to the plates. The ultimate strength is best approached by the first two models, 'CC/CC' and 'CC/CC, U2=free', with an underestimation of 6%. All models have an in-plane displacement difference below 5% with 'CC/CC,

U2=free' providing the most accurate result with a difference of 0.4%. The first four models have an out-of-plane difference of around 65%, while the fifth model, 'SS/SS', has an underestimation of 12%.

Model	Maximum stress (Mpa)	Difference (%)	In-plane displ. (mm)	Difference (%)	Out-of-plane displ. (mm)	Difference (%)
Test	148.36		1.44		8.13	
CC/CC	138.18	-6.9%	1.47	2.0%	2.76	-66.0%
CC/CC, U2=free	139.40	-6.0%	1.51	4.7%	2.57	-68.4%
CC/SS, U2=free	129.96	-12.4%	1.44	-0.4%	2.93	-64.0%
CC/SS	128.88	-13.1%	1.40	-2.8%	3.10	-61.9%
SS/SS	102.33	-31.0%	1.39	-3.3%	7.17	-11.8%

Table 6.8: Series 2, imperfection size B/100: maximum stress, in-plane displacement and out-of-plane displacement difference between the test results and the Abaqus/Standard model for the five different boundary conditions.

Results for series 2: Imperfection size B/33

An initial imperfection of B/33, which equals 9.6 millimetres, is applied to the plates. The first two models approximate the ultimate strength the best, with an underestimation of around 15%. The in-plane and out-of-plane displacement are most accurate for the 'SS/SS' model with an underestimation of 6% and 25%, respectively. The other four models undervalue the in-plane and out-of-plane displacement by roughly 11% and 50%, respectively.

Model	Maximum stress (Mpa)	Difference (%)	In-plane displ. (mm)	Difference (%)	Out-of-plane displ. (mm)	Difference (%)
Test	132.19		1.66		8.60	
CC/CC	111.82	-15.4%	1.48	-11.1%	3.98	-53.7%
CC/CC, U2=free	111.96	-15.3%	1.49	-10.4%	3.97	-53.8%
CC/SS, U2=free	106.51	-19.4%	1.46	-12.1%	4.12	-52.1%
CC/SS	106.40	-19.5%	1.45	-12.7%	4.16	-51.7%
SS/SS	94.89	-28.2%	1.56	-6.0%	6.46	-24.9%

Table 6.9: Series 2, imperfection size B/33: maximum stress, in-plane displacement and out-of-plane displacement difference between the test results and the Abaqus/Standard model for the five different boundary conditions.

6.4.3. Numerical agreement with experimental results

Table 6.10 presents the average values of the six situations for the five types of boundary conditions. The simply supported boundary condition 'SS/SS' gives the overall best result for the in-plane and out-of-plane displacement of the plate. However, the essential factor for buckling is the ultimate strength of the material. The model with the simply supported boundary conditions returns a significant underestimation of on average 29% of the strength of the plate. The ultimate strength is best approximated by the first model with the clamped boundary conditions 'CC/CC' which an average difference of 7.7%. Even though the test rig allowed some degree of movement and rotation, the model with all degrees of freedom restricted performs the best when modelling the ultimate strength of the plate. When additional degrees of freedom are introduced in the model, the underestimation of the material's ultimate strength is increased. Table 6.11 shows the best model for each of the six cases.

Model	Difference ultimate strength (%)	Difference in-plane displacement (%)	Difference out-of-plane displacement (%)
CC/CC	7.7%	11.5%	64.2%
CC/CC, U2=free	8.5%	11.5%	65.5%
CC/SS, U2=free	10.8%	13.1%	61.9%
CC/SS	11.5%	14.1%	60.9%
SS/SS	29.2%	11.6%	25.2%

Table 6.10: Average difference in ultimate strength, in-plane displacement and out-of-plane displacement for all six situations

Series	Size of imp. (mm)	Maximum stress (Mpa)	Diff. (%)	In-plane displ. (mm)	Diff. (%)	Out-of-plane displ. (mm)	Difference (%)
S1	No imp.	CC/SS, U2=free	-3.3%	SS	-8.6%	SS	-30.3%
S1	3.2	CC	0.2%	SS	3.4%	SS	-25.5%
S1	9.6	CC/CC, U2=free	-13.6%	CC	0.8%	SS	-49.6%
S2	No imp.	CC	-1.2%	CC/CC, U2=free	-23.2%	SS	-9.3%
S2	3.2	CC/CC, U2=free	-6.0%	CC/SS, U2=free	-0.4%	SS	-11.8%
S2	9.6	CC/CC, U2=free	-15.3%	SS	-6.0%	SS	-24.9%

Table 6.11: Overview of which type of boundary conditions approximates the test result the closest, for each of the six models

6.5. Part 2: Initial imperfections

The first part of this chapter has verified that the lower bound fracture energy can be used for progressive failure analysis to determine non-linear buckling behaviour. In the second part, the influence of initial imperfections on the buckling strength of a GFRP laminate is studied, for which the lower bound approach will be applied. Current design codes define the elastic buckling strength as an upper bound value and consider strength reduction due to initial imperfections via partial safety factors, and other factors, to characteristic strength values. There is a lack of data regarding the buckling strength reduction of GFRP plates, and it is unsure if the design code recommendations are too conservative or even underestimating the strength reduction for certain situations.

The influence of initial imperfections on the ultimate compressive strength of an anisotropic GFRP plate are investigated. Progressive failure analysis is applied to include the effect of damage and determine the load-carrying capacity for structures with post-buckling behaviour. A buckling curve is created by varying the thickness of the plate. The influence of geometric imperfections on the strength reduction is analysed by applying different sizes of initial imperfections. The material of the plate is as discussed in chapter 5. Plate geometry and boundary conditions are similar to the analysis performed in the first part of this chapter. Two types of boundary conditions are applied to the model: clamped and simply supported. In practice, most structures are in between such boundary conditions. In the last part, it was determined that those two types best replicate the strength and deformability of the plate. The goal is to quantify the influence of the initial imperfections on the plate's strength reduction and determine if the boundary conditions alter the resulting buckling curve.

6.5.1. Model properties

Progressive failure analysis of a GFRP plate requires the following parameters to be specified:

- The linearly elastic response of the undamaged material
- Damage initiation criteria
 - Hashin's failure criteria
 - Ultimate stresses
- Damage evolution response
 - Choice of element removal
 - Fracture energy for each of the four failure modes

The stiffness parameters of the material describe the linearly elastic response of the undamaged material. Hashin's damage initiation and evolution criteria are enforced as described in chapter 2. Linear degradation is chosen for element removal, as it is the only available option in Abaqus/Standard for the progressive failure of anisotropic materials. The material properties, presented in table 6.12, are concluded in chapter 5. The lay-up of the multi-directional laminate is used: $[90/0_3/45/-45/0_2]_S$. A regular mesh of 96 by 46 conventional shell elements is applied, as was recommended in the mesh refinement study by Hayman et al. (2011), which results in a characteristic element length of 6.95 millimetres. A 10% increase of the lower bound fracture energy is implemented, for which the model properties are stated in table 6.13.

	σ (MPa)	E (MPa)	ϵ (-)	G_c N/mm ²
Tension in fibre direction (TF)	839.53	41700	0.0201	8.44
Compression in fibre direction (CF)	425.89	41700	0.0102	2.17
Tension in matrix direction (TM)	25.17	12000	0.0021	0.03
Compression in matrix direction (CM)	122.56	12000	0.0102	0.63

Table 6.12: Material properties of the GFRP plate

	TF	CF	TM	CM
$G_c + 10\%$ (N/mm)	64.50	16.60	0.20	4.78

Table 6.13: Model properties for the fracture energy

6.5.2. Geometry and boundary conditions

The size of the plate is 320 by 640, which is equal to the width and twice the length as for the buckling models discussed in part I of this chapter. The thickness is varied from 6.88 millimetres, the thickness of the MD specimens, to 48.00 millimetres, which equals a plate slenderness of approximately 0.5.

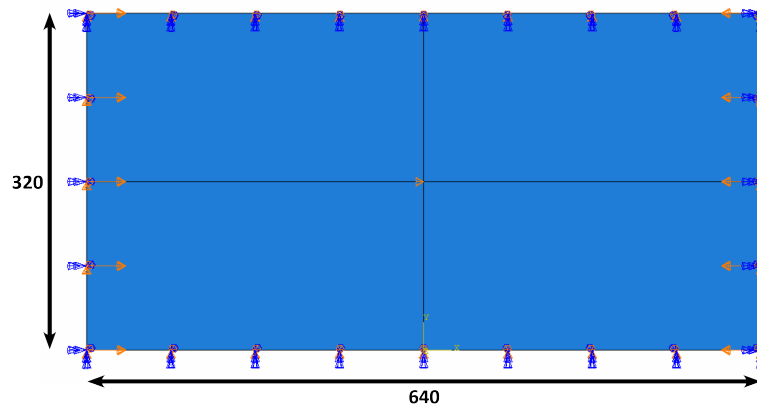


Figure 6.23: Dimensions of the plate

Two types of boundary conditions are applied to evaluate the dependency of the buckling curve on the boundary conditions of the numerical model. The degrees of freedom for both the simply supported and clamped boundary conditions are shown in figure 6.25 and 6.26. Figure 6.24 displays the degrees of freedom of a conventional shell element. In both cases, displacement is applied in the x-direction on the two shorter sides of the plate. The edges are allowed to rotate for the simply supported boundary conditions, while all degrees of freedom are restricted for the clamped boundary conditions.

6.23.

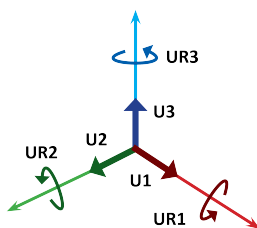


Figure 6.24: Schematic view of the six degrees of freedom

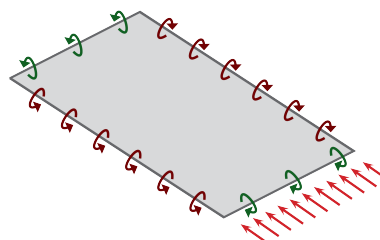


Figure 6.25: Simply supported boundary conditions

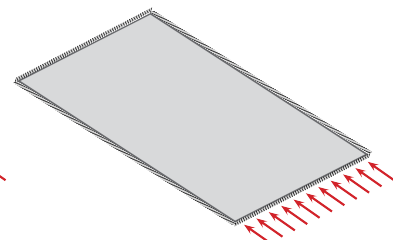


Figure 6.26: Clamped boundary conditions

6.5.3. Initial imperfection

Six different initial imperfections are applied to the plate. These imperfections are created by scaling the size of the first buckling mode shape in relation to the width of the plate 'B'. The applied sizes are as follows: B/1000, B/640, B/320, B/240, B/160 and B/125. These ratios equal imperfections ranging from 0.32 to 2.56 millimetres. The value of B/125 equals the limiting value of L/125, as stated in CUR96 (CUR Recommendation 96, 2017), with L equal to the smallest dimension of width or length of the plate.

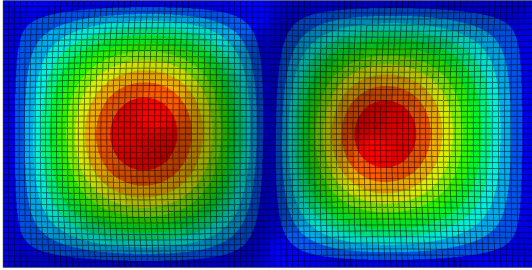


Figure 6.27: Shape of the geometric imperfection for the simply supported model

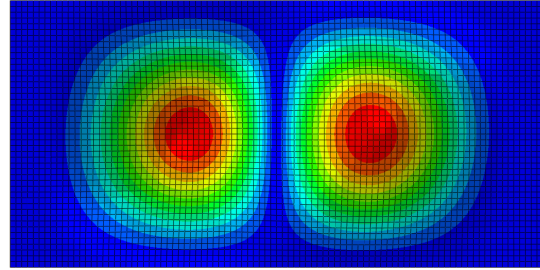


Figure 6.28: Shape of the geometric imperfection for the clamped model

6.6. Numerical results

For both boundary conditions, eleven plate thicknesses are analysed with six different initial imperfection each. The force-displacement curves are shown in appendix D. In the following sections, the influence of the initial imperfections on the strength reduction of the plate will be discussed, and if the type of boundary conditions influences the obtained buckling curve. All curves show a significant drop in strength after the failure of the plate, as expected from implementing the lower bound fracture energy.

6.6.1. Buckling curve

The plate slenderness, λ , is a ratio used to classify plates with different geometries and material properties. The slenderness of a plate depends on the critical buckling stress of plate, σ_{cr} , and the material strength of a perfect plate under uniform loading, f_{ult} . The material strength depends on the chosen failure criteria.

$$\lambda = \sqrt{\frac{f_{ult}}{\sigma_{cr}}} \quad (6.1)$$

In the case of $\lambda = 1$, the compressive load coincides with the critical loading. The slenderness is defined for a plate without imperfections and can be derived analytically. The failure load of a plate with initial imperfections, f_{fail} , can be determined with progressive failure analysis. When loading is applied to a plate with eccentricities, additional bending moments arise and additional stresses are introduced. The reduction factor, ρ , describes the strength reduction of the imperfect plate:

$$\rho = \frac{f_{fail}}{f_{ult}} \quad (6.2)$$

Table 6.15 shows the critical stress, slenderness and reduction factors for the different plate thicknesses, applied initial imperfections and boundary conditions. In appendix C, the numerical critical stress values are compared to the analytical determined critical stress values. 'CC' equals the clamped boundary conditions as depicted in figure 6.26 and 'SS' equals the simply supported boundary conditions as shown in figure 6.25. A buckling curve is created from the slenderness values and reduction factors to represent the influence of geometric imperfections on the buckling failure behaviour of the plate. This is done for both boundary conditions and each of the six initial imperfections. The buckling curves can be found in figure 6.29 and 6.30.

The horizontal axis of the buckling curves indicates the plate slenderness, and the vertical axis displays the reduction factor. The elastic buckling strength is depicted with a black dotted line; this line represents the strength reduction due to buckling without residual stresses and geometric imperfections. The horizontal plateau represents thick plates, where the material strength is governing. Around 1.5 slenderness, the elastic buckling strength crosses the curves with initial imperfections. Plate slenderness above 1.5 equals a plate where the critical buckling stress is below the material strength of the plate. When they reach the critical buckling stress, these plates will buckle and continue to carry the loading until the material strength is reached.

Thickness (mm)	BC (-)	σ_{cr} (N/mm ²)	λ (-)	ρ (-)					
				B/1000	B/640	B/320	B/240	B/160	B/125
6.88	CC	58.39	2.42	0.323	0.323	0.322	0.320	0.319	0.317
10.40	CC	135.16	1.59	0.453	0.453	0.455	0.449	0.446	0.443
13.76	CC	231.11	1.21	0.670	0.648	0.602	0.577	0.539	0.523
16.00	CC	306.63	1.05	0.793	0.754	0.689	0.659	0.611	0.586
20.64	CC	486.97	0.84	0.905	0.875	0.808	0.758	0.718	0.685
24.00	CC	632.83	0.73	0.933	0.908	0.851	0.804	0.766	0.733
27.52	CC	794.54	0.66	0.947	0.923	0.878	0.836	0.800	0.774
32.00	CC	1006.97	0.58	0.962	0.940	0.898	0.860	0.829	0.797
34.40	CC	1121.35	0.55	0.964	0.945	0.905	0.870	0.838	0.808
41.28	CC	1441.14	0.49	0.966	0.956	0.924	0.895	0.859	0.831
48.00	CC	1729.62	0.44	0.970	0.953	0.923	0.893	0.872	0.846
6.88	SS	31.50	3.29	0.348	0.348	0.349	0.350	0.350	0.351
10.40	SS	70.28	2.20	0.418	0.417	0.416	0.414	0.413	0.413
13.76	SS	120.90	1.68	0.416	0.419	0.424	0.426	0.428	0.428
16.00	SS	161.22	1.45	0.466	0.451	0.447	0.443	0.440	0.439
20.64	SS	260.32	1.14	0.679	0.654	0.603	0.577	0.541	0.523
24.00	SS	343.86	1.00	0.796	0.759	0.706	0.677	0.627	0.604
27.52	SS	440.59	0.88	0.881	0.849	0.781	0.750	0.700	0.669
32.00	SS	575.29	0.77	0.926	0.900	0.842	0.810	0.759	0.727
34.40	SS	651.91	0.72	0.937	0.915	0.862	0.834	0.785	0.752
41.28	SS	884.62	0.62	0.958	0.941	0.900	0.876	0.834	0.803

Table 6.14: Numerical results for the critical stress, relative slenderness and reduction factor for the different plate thickness, varying initial imperfection sizes and two types of boundary conditions

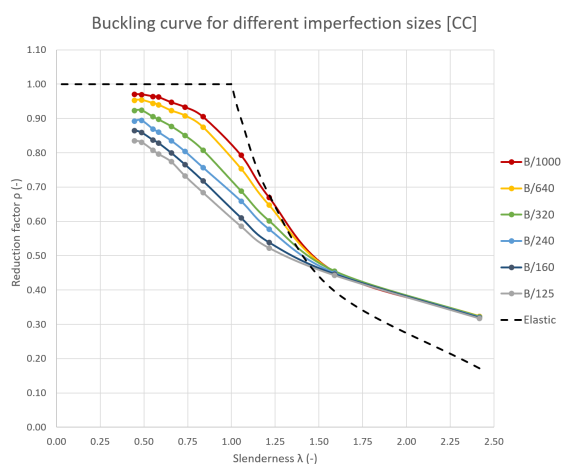


Figure 6.29: Buckling curve for different initial imperfections with clamped boundary conditions

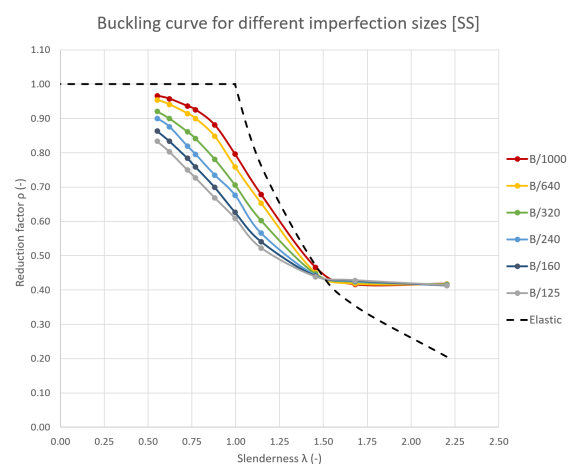


Figure 6.30: Buckling curve for different initial imperfections with simply supported boundary conditions

6.6.2. Design code

CUR Recommendation 96 (2017) considers the buckling strength of a plate to be equal to the elastic buckling strength, which does not take the non-linear buckling behaviour due to residual stresses and geometric imperfections into account. The reduction factor as determined from the elastic buckling strength is shown with a black dotted line in figure 6.29 and 6.30. It is the upper value for thick and mid-thick plates that do not reach the critical buckling stress. The design value for the compressive force is multiplied by the reduction factor obtained from the elastic buckling curve. For numerical analysis, the recommendation is provided to include all imperfections by modelling a dominant imperfection with appropriate magnitude, such as the out-of-straightness imperfection with amplitude $B/125$. For plate slenderness around 1.0, buckling curves in figure reffig:curveCC and 6.30 show a difference in reduction factor compared to the elastic buckling strength of 15% and 40% for $B/1000$ and $B/125$, respectively. The conservative option to implement $B/125$ leads to the use of unnecessary thick plates.

6.6.3. Influence of initial imperfection size

The influence of geometrical imperfections on the strength of the plate is shown in figure 6.29 and 6.30. For thick and mid-thick plates, the plates fail before they reach the critical buckling stress, and a larger imperfections result in a higher strength reduction. Large initial imperfections can result in 40% strength reduction compared to the elastic buckling strength. The difference in reduction factor between an initial imperfection of $B/1000$ and $B/125$ is shown in table 6.15 for clamped boundary conditions and in table 6.16 for simply supported boundary conditions. The results are compared in figure 6.31.

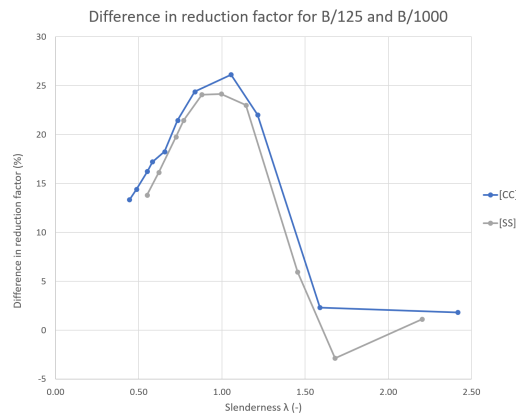


Figure 6.31: Difference in reduction factor between $B/1000$ and $B/125$ for simply supported [SS] and clamped [CC] boundary conditions

The difference in reduction factor is larger for the plate with clamped boundary conditions than for the plate with simply supported boundary conditions. The largest difference in ultimate strength between an initial imperfection of $B/1000$ and $B/125$ can be found for plate slenderness around 1.0, where the critical stress coincides with the ultimate strength of a perfect plate. Here, an initial imperfection of $B/125$ resulted in 40% strength reduction compared to the elastic buckling strength. For the plates with clamped boundary conditions, a reduction factor difference of up to 26% is found. The difference is most significant for slenderness values between 0.84 and 1.21. For simply supported boundary conditions, the largest difference can be found for a slenderness range of 0.88 till 1.14, reaching a difference of 24%. On average, the difference in reduction factor is 16.14% and 14.65%, for clamped and simply supported boundary conditions, respectively.

Plates with relatively high slenderness have an ultimate strength higher than their critical buckling stress. The plates buckle when the critical load is reached and continue to carry the loading. These thin plates have the lowest buckling resistance. The size of the initial imperfection does not significantly influence the ultimate strength, and the difference in reduction factor is below 3%. For plates with slenderness above 1.0, the difference in reduction factor for different imperfection sizes decreases for an increase in plate slenderness.

Plate thickness (mm)	λ	Difference (%)
6.88	2.42	1.83
10.40	1.59	2.32
13.76	1.21	22.03
16.00	1.05	26.13
20.64	0.84	24.37
24.00	0.73	21.45
27.52	0.66	18.24
32.00	0.58	17.22
34.40	0.55	16.23
41.28	0.49	14.39
48.00	0.44	13.33

Table 6.15: Difference in reduction factor for initial imperfection B/1000 and B/125 for clamped boundary conditions

Plate thickness (mm)	λ	Difference (%)
6.88	3.29	-0.81
10.40	2.20	1.11
13.76	1.68	-2.87
16.00	1.45	5.94
20.64	1.14	23.01
24.00	1.00	24.14
27.52	0.88	24.08
32.00	0.77	21.45
34.40	0.72	19.75
41.28	0.62	16.12
48.00	0.55	13.81

Table 6.16: Difference in reduction factor for initial imperfection B/1000 and B/125 for simply supported boundary conditions

6.6.4. Influence of boundary conditions

The buckling curves for an initial imperfection size of B/1000 and B/125 with simply supported (SS) and clamped (CC) boundary conditions are compared in 6.32 and 6.33, to analyse if changing the boundary conditions results in a different buckling curve.

Imperfection size B/1000

For plate slenderness between 0.55 and 0.84, there is no difference in the reduction factor for both boundary conditions. For mid-thick plates, ranging from 1.00 and 1.50, the CC curve is slightly shifted to the right; clamped thinner plates have the same strength reduction as thicker simply supported plates. For thin plates with slenderness above 1.50, the situation switches around.

Imperfection size B/125

For slenderness values of 0.72 and lower, thick clamped plates have a slightly higher strength reduction than similar simply supported plates. When the plate slenderness is between 0.72 and 1.05, this difference disappears. The clamped plates show less strength reduction for higher slenderness values except for the thickest clamped plate, which has a notable lower strength compared to a simply supported plate with the same thickness.

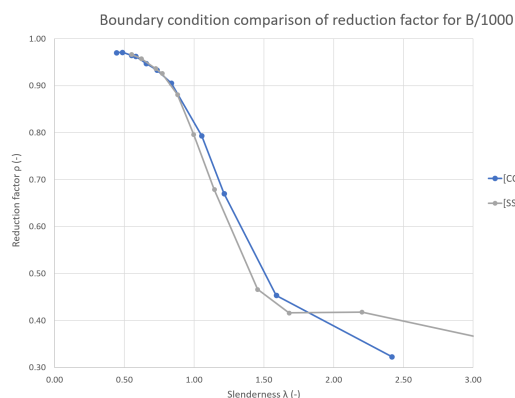


Figure 6.32: Reduction factor comparison for both types of boundary conditions and initial imperfection of B/1000

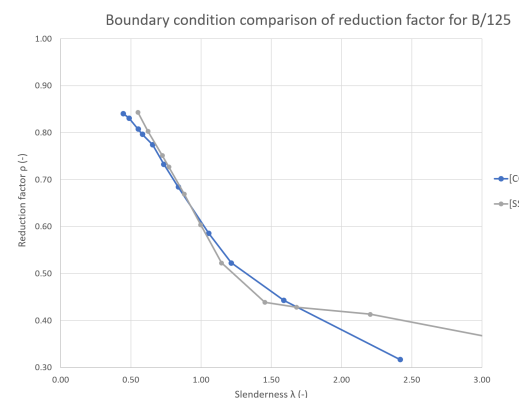


Figure 6.33: Reduction factor comparison for both types of boundary conditions and initial imperfection of B/125

The strength reduction values for slenderness above 1.50 differ significantly. A possible explanation could be the difference in initial imperfection shape. The imperfection size is the same, but the out-of-plane deformation does not coincide. Initial imperfections have the most significant influence on mid-thick plates. The highest strength reduction between an initial imperfection of B/1000 and B/125

was found for plate slenderness around 1.0. When comparing the curves of both boundary conditions for this slenderness value, the reduction factor is reduced by 0.05 for the simply supported curve, which equals a lower buckling strength. This difference occurs for a small imperfection of $B/1000$ and disappears for a large imperfection of $B/125$. The largest difference between the two boundary conditions is found for plate slenderness around 1.45; an initial imperfection of $B/1000$ shows a 0.1 decrease in reduction factor for the buckling curve with simply supported boundary conditions. For an imperfection size $B/125$, this decrease reduces to 0.05.

6.6.5. Failure modes

To create a better understanding of why the plates fail, the failure behaviour of four of the models is analysed. For each model, it is studied which failure mode occurs first and which failure mode results in failure of the plate. The models are all in the slenderness range of 1.00 and 1.50. In figure D.12 up to and including D.2, the force-displacement curves of the four plates are shown. The four models are a clamped plate with an initial imperfection size of $B/1000$ and $B/125$ and a simply supported plate with the same imperfections. On each of the curves, the displacement at which a certain failure mode occurs is plotted. The black dotted line equals the critical buckling stress obtained from linear buckling analysis (LBA).

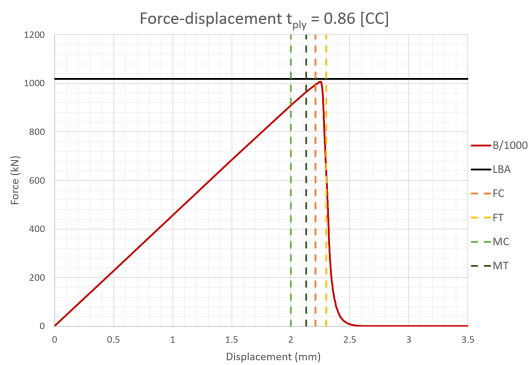


Figure 6.34: Force-displacement curve for plate thickness of 13.76 mm, $\lambda = 1.21$, initial imperfection size of $B/1000$ and clamped boundary conditions

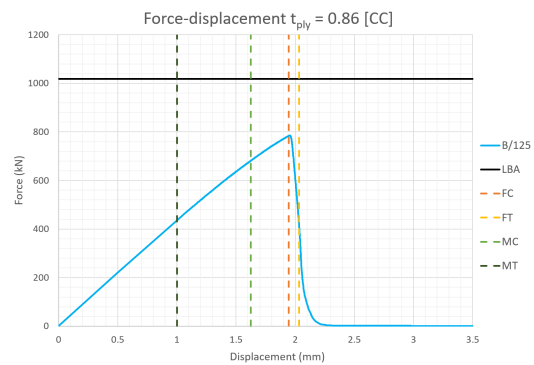


Figure 6.35: Force-displacement curve for plate thickness of 13.76 mm, $\lambda = 1.21$, initial imperfection size of $B/125$ and clamped boundary conditions

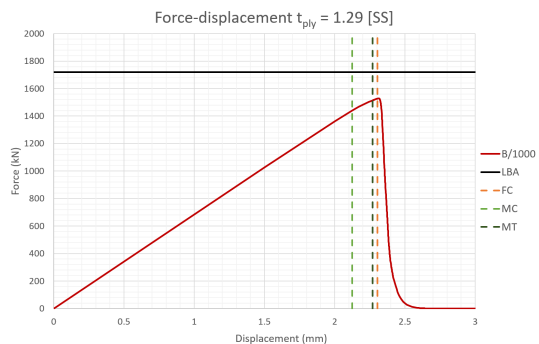


Figure 6.36: Force-displacement curve for plate thickness of 20.64 mm, $\lambda = 1.14$, initial imperfection size of $B/1000$ and simply supported boundary conditions

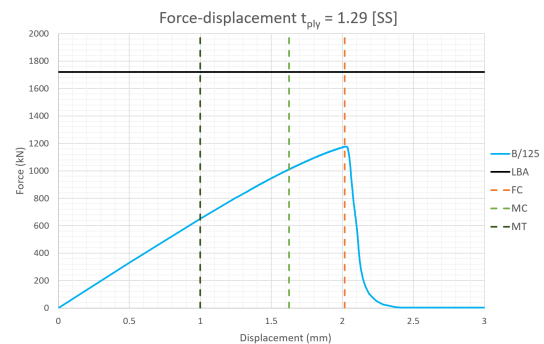


Figure 6.37: Force-displacement curve for plate thickness of 20.64 mm, $\lambda = 1.14$, initial imperfection size of $B/125$ and simply supported boundary conditions

For all four models, the material fails when the fibres fail in compression (FC). For the small initial imperfection of $B/1000$, the first failure mode is matrix failure in compression (MC), followed by matrix failure in tension (MT). For the larger initial imperfections of $B/125$, these two failure modes are switched. First, the matrix fails in tension, followed by matrix failure in compression. The difference between the clamped and simply supported boundary conditions is that fibre failure in tension (FT) does not occur for the latter. For the applied imperfection of $B/1000$, all failure modes occur close to the point of failure, while for an applied imperfection of $B/125$, the first two failure modes occur at a lower displacement. The failure modes are displayed in figure 6.38 up to and including 6.53.

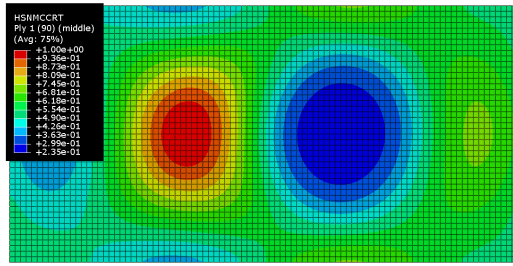


Figure 6.38: Clamped BC and initial imperfection of B/1000 - First failure mode: matrix in compression

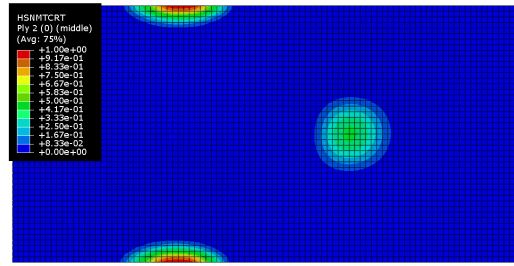


Figure 6.39: Clamped BC and initial imperfection of B/1000 - Second failure mode: matrix in tension

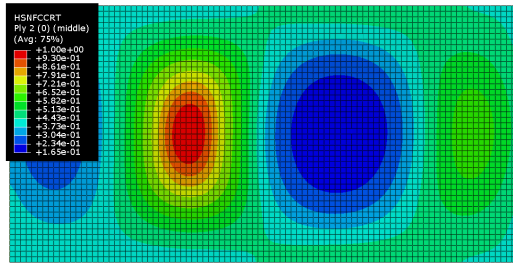


Figure 6.40: Clamped BC and initial imperfection of B/1000 - Third failure mode: fibres in compression

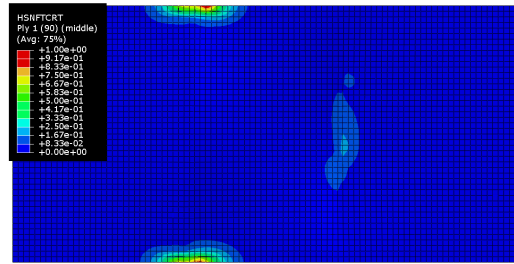


Figure 6.41: Clamped BC and initial imperfection of B/1000 - Fourth failure mode: fibres in tension

The first failure of the matrix in compression occurs in ply 1, which is the top, and because of symmetry, the bottom ply. This ply is in the 90° direction. The second and third failure mode occur in the third ply, which is oriented in the 0° direction. The fourth failure mode is again in the first ply and occurs due to damage at the edges. The ply in which each failure mode occurs is the same for the initial imperfection of B/1000 and B/125. However, the larger imperfection shows an increased damaged area for the first three failure modes.

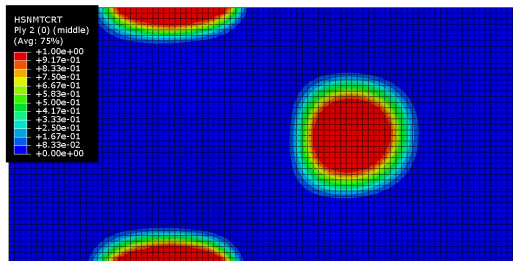


Figure 6.42: Clamped BC and initial imperfection of B/125 - First failure mode: matrix in tension

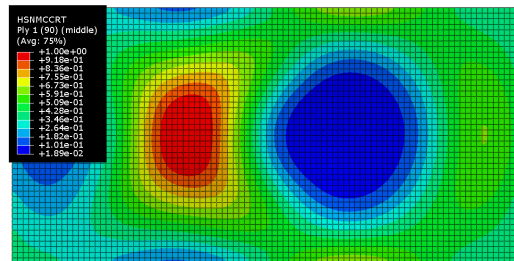


Figure 6.43: Clamped BC and initial imperfection of B/125 - Second failure mode: matrix in compression

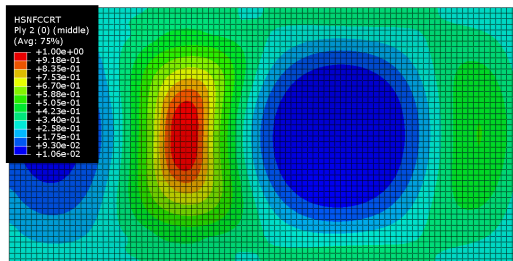


Figure 6.44: Clamped BC and initial imperfection of B/125 - Third failure mode: fibres in compression

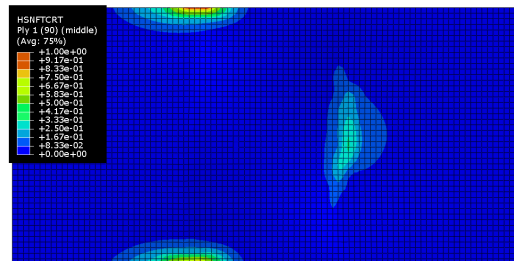


Figure 6.45: Clamped BC and initial imperfection of B/125 - Fourth failure mode: fibres in tension

When the failure modes for the two types of boundary conditions are compared, a couple of differences can be seen. The damaged area is more significant for the simply supported plates, which relates to the

first buckling shape mode for this boundary condition. For the clamped boundary conditions, there is notable damage around the edges. Due to a larger flat area at the edges, the stress concentrations will move around the imperfection and towards these flat areas that can still resist loading. This could also be related to why fibres' failure in tension only occurs for the plates with clamped boundary conditions. The failure occurs near the edges, and for the simply supported plates, the stress can not arise at this location.

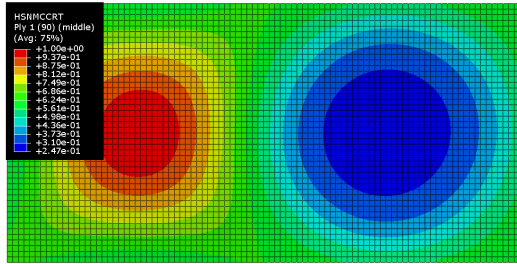


Figure 6.46: Simply supported BC and initial imperfection of B/1000 - First failure mode: matrix in compression

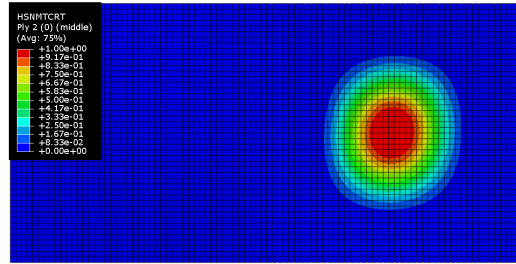


Figure 6.47: Simply supported BC and initial imperfection of B/1000 - Second failure mode: matrix in tension

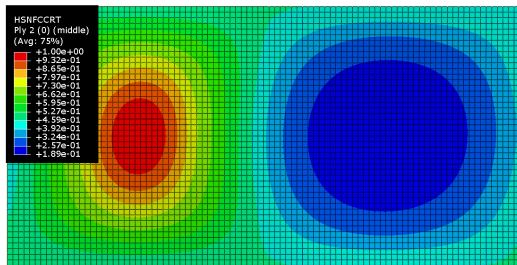


Figure 6.48: Simply supported BC and initial imperfection of B/1000 - Third failure mode: fibres in compression

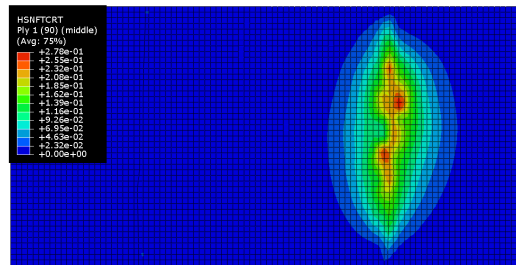


Figure 6.49: Simply supported BC and initial imperfection of B/1000 - No failure of fibres in tension

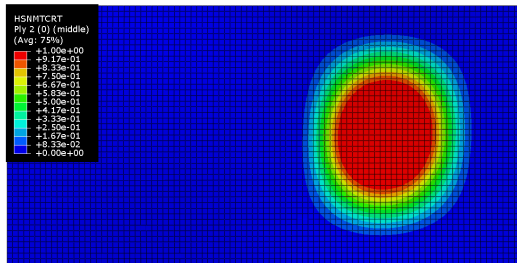


Figure 6.50: Simply supported BC and initial imperfection of B/125 - First failure mode: matrix in tension

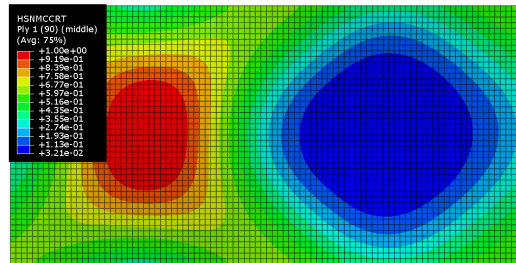


Figure 6.51: Simply supported BC and initial imperfection of B/125 - Second failure mode: matrix in compression

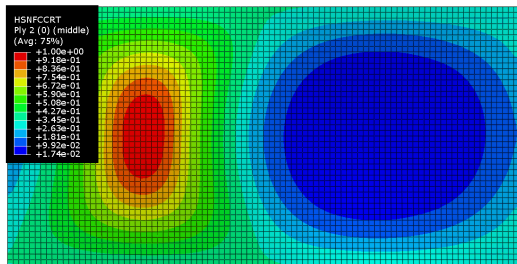


Figure 6.52: Simply supported BC and initial imperfection of B/125 - Third failure mode: fibres in compression

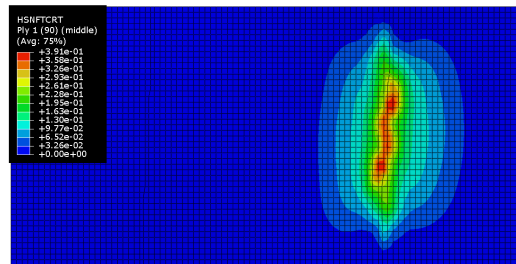


Figure 6.53: Simply supported BC and initial imperfection of B/125 - No failure of fibres in tension

6.7. Conclusion

A two-part parametric study is performed. The first part is performed to validate if progressive failure analysis with Hashin damage criteria based on lower bound fracture energy can be used for determining the non-linear buckling behaviour of a GFRP laminate. In the second part, the effects of initial imperfections on the ultimate compressive strength of composite plate-like structures are studied. In part 1, numerical analysis is performed on experimental tests obtained from literature. Two different lay-ups and three different initial imperfections size are implemented in these tests. The buckling behaviour of the plates was tested in a test rig, which allowed for some degree of movement. By applying different types of boundary conditions, it was determined that restricting the movement of the plate in all directions most accurately modelled the test set-up. For this type of boundary conditions, the numerical determined ultimate strength had an average difference of 7.7%. When rotation was allowed in the model, the in-plane and out-of-plane displacement of the model were better approximated, but the ultimate strength deviated by 30%. The lower bound fracture energy, increased by 10%, was implemented. The numerical results all showed an abrupt drop in strength and stiffness when the ultimate strength of the plate was reached. The lower bound fracture energy resulted in an average strength difference of 7.7%, partly explained by the uncertainties about the boundary conditions and material properties. It is concluded that the Hashin damage criteria with lower bound fracture energy can be used for progressive ply analysis of non-linear buckling analysis.

In the second part, a non-linear buckling analysis is performed to study the influence of initial imperfections on the buckling strength of a GFRP laminate. Two boundary conditions are applied to analyse if these model properties influence the resulting buckling curve. The highest strength reduction between an initial imperfection of $B/1000$ and $B/125$ was found for plate slenderness around 1.0. When comparing the reduction factor for this plate slenderness for both boundary conditions, the reduction factor is reduced by 0.05 for the simply supported curve, which equals a lower buckling strength. This difference occurs for a small imperfection of $B/1000$ and disappears for a large imperfection of $B/125$. The largest difference between the two boundary conditions is found for plate slenderness around 1.45; an initial imperfection of $B/1000$ shows a 0.1 decrease in reduction factor for the buckling curve with simply supported boundary conditions. For an imperfection size $B/125$, this decrease reduces to 0.05. Failure of fibres in compression is for both boundary conditions the failure mode that results in failure of the plate. For simply supported boundary conditions, the matrix fails first in compression, followed by matrix failure in tension. For clamped plates, the occurring order of these failure modes is switched.

The buckling curves are analysed to determine the influence of initial imperfections on the strength of a GFRP plate. A higher initial imperfection results in a higher ultimate strength reduction factor and thus a lower buckling resistance. Higher plate slenderness equals thinner plates, which are more prone to buckling. The influence of the imperfection size is most apparent for the plates with relative slenderness around 1.0, where the critical stress coincides with the ultimate strength of the perfect plate. Here, an initial imperfection of $B/125$ resulted in 40% strength reduction compared to the elastic buckling strength. For clamped boundary conditions, the imperfection size results in a difference in the reduction factor of up to 26% for slenderness values between 0.84 and 1.21. For simply supported boundary conditions, a reduction factor difference of 24% can be found for the slenderness range of 0.88 to 1.14. The conservative option of an imperfection size of $B/125$ results in unnecessary thick plates.

Conclusion & recommendation

7.1. Conclusion

This paper investigates how the non-linear buckling behaviour of GFRP plates can be predicted with progressive failure analysis. Abaqus implement the Hashin damage criteria as default criteria for the damage behaviour of FRP materials. These criteria require the input of the material's fracture energy. An accurate implementation of the fracture energy is necessary because the fracture energy of each failure mode influences the damaged area, state of damage of the finite elements, the ultimate load prediction and the post-failure behaviour. Due to a lack of experimental data, the actual fracture energy of the material could not be determined, and the lower bound value is implemented to analyse the buckling behaviour of a GFRP plate. The lower bound fracture energy is a conservative option for modelling failure of a material; it equals abrupt failure and thus no post-failure load carrying capacity in the material. However, when the actual fracture energy of the material is lower than the determined lower bound value, the fracture toughness of the material is overestimated.

The plate's material properties and lower bound fracture energy are determined from numerical analysis of uni-directional coupon experiments. Numerical analysis of multi-directional coupon experiments validated the use of lower bound fracture energy for progressive failure analysis. Implementation of the lower bound fracture energy for non-linear buckling analysis was affirmed by numerical analysis of experimental buckling tests.

A parametric study is performed to determine the load-carrying capacity of a GFRP plate with post-buckling behaviour. A buckling curve is created by varying the thickness of the plate. The influence of geometric imperfections on buckling strength reduction is analysed by applying different initial imperfections. Two types of boundary conditions are enforced to determine if the boundary conditions alter the resulting buckling curve. The following conclusions are drawn in this report:

- Abaqus/Standard implemented the Hashin damage criteria for FRP material by default. Damaged quasi-brittle materials experience strain-softening, which can lead to deformation localisation in a single element. To prevent the localisation of smeared cracking into arbitrarily small regions, the stress is related to the deformation of a finite volume. This is done by adjusting the energy dissipated by each failure mechanism and defining the fracture energy as a material parameter. The fracture energy is now dependent on a characteristic length (L_c), which estimates the fracture process zone length based on material properties. For both conventional and continuum shell elements, the characteristic length is equal to the square root of the area of the element.
- Numerical issues can occur when the fracture energy input for the numerical analysis is too low. Abaqus/Standard calculates the minimal required fracture energy that leads to failure based on the material properties and the element's actual characteristic length. Deformation of the elements can lead to a change in the characteristic element length. Abaqus/Standard is programmed to increase the implemented fracture energy if it is below the minimum required

value. After the material reaches the ultimate strength, a more gradual stress decrease occurs instead of the expected abrupt drop in strength, and a low fracture energy value is not a conservative solution. Adding a minimum of two % to the fracture energy lower bound value prevented this problem.

- Progressive failure analysis of four multi-directional coupon experiments verified that increasing the lower bound fracture energy value does not change the validity of the numerical results. The lower bound fracture energy input for these models was increased by 5% and 10%. The numerical results are in good agreement with the test results.
- The lower bound fracture energy, increased by 10%, was implemented for progressive failure analysis of non-linear buckling experiments. Two GFRP plates with varying thickness and three different types of initial imperfections were analysed. The ultimate strength was estimated with an average difference of 7.7% compared to the experimental results.
- A clamped and simply supported type of boundary conditions were applied for non-linear buckling analysis. The buckling curves were comparable for slenderness values below 1.50. The most significant difference in the reduction factor for the two boundary conditions is found for plate slenderness of 1.45; an initial imperfection of B/1000 showed a 0.1 decrease of the reduction factor for the simply supported plate. For an imperfection size of B/125, this decrease reduced to 0.05. Failure of the fibres in compression is for both boundary conditions the failure mode that results in failure of the plate.
- Initial imperfections in a plate reduce the buckling strength of the material. The influence of the imperfection size is most apparent for plates with relative slenderness around 1.0, where the critical stress coincides with the ultimate strength of the perfect plate. An initial imperfection of B/125 resulted in a 40% strength reduction compared to the elastic buckling strength. The average difference in reduction factor between an initial imperfection of B/1000 and B/125 was 16%, with a maximum difference of 26%. The conservative option of B/125, as recommended by the design codes, resulted in up to 26% higher strength reduction compared to an initial imperfection of B/1000, and can lead to over dimensioning of the plates.

7.2. Recommendation

This study can be extended by performing further research into the following topics:

- Experimental tests are available for the determination of the fracture toughness of a material. In the absence of experimental data, the stress-strain curve of coupon tests can be used to approximate the fracture energy of a material. Due to the large scatter in data from the coupon tests, the fracture energy could not be determined, and the lower bound value was used. It is recognised that this report does not model the actual post-failure behaviour. Experimental research for determining fracture energy values of GFRP plates is highly recommended to obtain more data to improve the numerical analyses and increase the understanding of GFRP failure behaviour.
- The fracture energy is implemented in relation to the characteristic element length, which represents the fracture process zone. The relation was demonstrated by a small sensitivity study, where the fracture energy input and element size were scaled separately. An additional sensitivity study could provide valuable information about the maximum allowable mesh size to determine a good fit between low computational costs and numerical accuracy.
- Previous literature has shown that a continuum stacked shell approach with cohesive zone modelling can capture failure behaviour of FRP well. The use of Abaqus/Standard led to convergence issues when this modelling method was applied. A repeat of this study, with a continuum stacked shell approach with cohesive zone modelling, could better capture the failure behaviour and improve the understanding of the influence of the fracture energy on GFRP failure behaviour. Using explicit analysis instead of implicit analysis should dismiss the convergence issues.

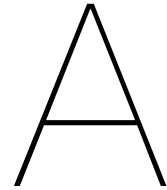
- The modelling accuracy of FRP laminates could be increased even more by using a 3D damage model. The Hashin damage model can only be used for shell elements and not for solid elements. Implementing the Hashin failure criteria in Abaqus/Explicit, using a user subroutine, could significantly increase the modelling accuracy.
- In this research, the buckling curves from two plates with different boundary conditions are compared. The buckling curves are similar, but differences do occur. To the author's knowledge, the exact reason for this difference is unknown. Additional research could improve the understanding of the influence of boundary conditions on non-linear buckling results. The initial imperfection is applied for both plates as the first mode shape for the respective boundary condition, similar to steel structures. This difference in mode shape results in different damaged areas. For both plates, failure of the fibres in compression is the definitive failure mode of the plate, which is as expected with buckling behaviour. However, it is interesting to notice that the first failure modes are different.
- It is recognised that the ply thickness used to create the buckling curve is not practical. The number of variables had to be limited, and it was chosen to vary the thickness of the laminate, the size of initial imperfection and the boundary conditions. A large ply thickness was needed to obtain thicker laminates, which have low relative slenderness. A change in laminate lay-up can be applied to achieve similar slenderness values.

References

- Akbarov, S. (2013). *Stability loss and buckling delamination: Three-dimensional linearized approach for elastic and viscoelastic composites*. Springer, Berlin, Heidelberg.
- Al-Moussawi, H., Drown, E. K., and Drzal, L. T. (1993). The silane/sizing composite interphase. *Polymer Composites*, 14(3):195–200.
- Almeida-Fernandes, L., Silvestre, N., and Correia, J. R. (2019). Characterization of transverse fracture properties of pultruded gfrp material in tension. *Composites Part B: Engineering*, 175:107095.
- Asicone, L., Berardi, V. P., Giordano, A., and Spadea, S. (2012). Buckling failure modes of frp thin-walled beams. *Composites Part B: Engineering*, 47:357–364.
- ASTM D3039 (2017). Standard test method for tensile properties of polymer matrix composite materials.
- Barbero, E., Cosso, F., Roman, R., and Weadon, T. (2013). Determination of material parameters for Abaqus progressive damage analysis of e-glass epoxy laminates. *Composites Part B: Engineering*, 46:211–220.
- Bazant, Z. and Cedolin, L. (2010). *Stability of structures: Elastic, inelastic, fracture and damage theories*. World Scientific Publishing Co.
- Bazant, Z. and Oh, B. (1983). Crack band theory for fracture of concrete. *Matériaux et Constructions*, 16:155–177.
- Beura, S., Thatoi, D., Chakraverty, A. P., and Mohanty, U. (2018). Impact of the ambiance on gfrp composites and role of some inherent factors: A review report. *Journal of Reinforced Plastics and Composites*, 37:533–547.
- Cornelissen, L. (2020). Pin bearing in glass fiber-reinforced polyester: An experimental and numerical study on the static and fatigue response of a gfrp laminate. Master's thesis, Technical University Delft.
- Csillag, F., Pavlovic, M., and Van Der Meer, F. (2019). Progressive damage analysis of pin bearing failure in gfrp using continuum shell fe modelling approach. In *9th Biennial Conference on Advanced Composites in Construction 2019, ACIC 2019 3- 5 September 2019, Birmingham, United Kingdom*, pages 68–74. 9th Biennial Conference on Advanced Composites in Construction 2019, ACIC 2019 ; Conference date: 03-09-2019 Through 05-09-2019.
- CUR Recommendation 96 (2017). *Aanbeveling 96:2017 Vezelversterkte kunststoffen in bouwkundige en civieltechnische draagconstructies*. SBRCURnet.
- Davalos, J. F., Barbero, E. J., and Qiao, P. (2002). *Step-by-Step Engineering Design Equations for Fiber-reinforced Plastic Beams for Transportation Structures*.
- Degenhardt, R., Castro, S., Arbelo, M., Zimmerman, R., Khakimova, R., and Kling, A. (2014). Future structural stability design for composite space and airframe structures. *Thin-Walled Structures*, 81:29–38.
- Ebnesajjad, S. (2016). Introduction to plastics. In Erwin Baur and Katja Ruhrberg and William Woishnis, editor, *Chemical Resistance of Commodity Thermoplastics*, Plastics Design Library, pages xiii – xxv. William Andrew Publishing.
- Greenhalgh, E. S. (2009). 7 - defects and damage and their role in the failure of polymer composites. In *Failure Analysis and Fractography of Polymer Composites*, Woodhead Publishing Series in Composites Science and Engineering, pages 356–440. Woodhead Publishing.

- Gu, J. and Chen, P. (2017). Some modifications of hashin's failure criteria for unidirectional composite materials. *Composite Structures*, 182:143–152.
- Gunes, O. (2013). 5 - failure modes in structural applications of fiber-reinforced polymer (frp) composites and their prevention. In *Developments in Fiber-Reinforced Polymer (FRP) Composites for Civil Engineering*, Woodhead Publishing Series in Civil and Structural Engineering, pages 115 – 147. Woodhead Publishing.
- Hashin, Z. (1980). Failure Criteria for Unidirectional Fiber Composites. *Journal of Applied Mechanics*, 47(2):329–334.
- Hayman, B., Berggreen, C., Lundsgaard-Larsen, C., Delarche, A., Toftegaard, H., Dow, R. S., Downes, J., Misirlis, K., Tsouvalis, N., and Douka, C. (2011). Studies of the buckling of composite plates in compression. *Ships and Offshore Structures*, 6(1-2):81–92.
- Helbig, D., Silva, C. C. C. d., Real, M. d. V., Santos, E. D. d., and Rocha, L. A. O. (2016). Study About Buckling Phenomenon in Perforated Thin Steel Plates Employing Computational Modeling and Constructal Design Method. *Latin American Journal of Solids and Structures*, 13:1912 – 1936.
- Hill, R. (1948). A theory of the yielding and plastic flow of anisotropic metals. *Proceedings of the Royal Society of London. Series A. Mathematical and Physical Sciences*, 193:281 – 297.
- Hoffman, O. (1967). The brittle strength of orthotropic materials. *Journal of Composite Materials*, 1(2):200–206.
- Joint Research Centre (2016). *EUR 27666 EN "Prospect for New Guidance in the Design of FRP"*.
- KACHANOV, L. M. (1958). Time of the rupture process under creep conditions, izy akad. *Nank S. S. R. Otd Tech Nauk*, 8:26–31.
- Kalveram, S. (2015). Mechanical properties of fiber-reinforced polymer derived ceramics.
- Kaskovits, A. (2018). Influence of initial imperfections on buckling of fibre reinforced polymer plates produced by vacuum assisted resin transfer molding. Master's thesis, Technical University Delft.
- Kollár, L. P. (2003). Local buckling of fiber reinforced plastic composite structural members with open and closed cross sections. *Journal of Structural Engineering*, 129(11):1503–1513.
- Kuldeep Agarwal, Suresh K Kuchipudi, Benoit Girard, and Matthew Houser (2018). Mechanical properties of fiber reinforced polymer composites: A comparative study of conventional and additive manufacturing methods. *Journal of Composite Materials*, 52(23):3173–3181.
- Landolfo, R. (2008). Cold-formed (cf) structures eurocode 9 - part 1.4.
- Lapczyk, I. and Hurtado, J. A. (2007). Progressive damage modeling in fiber-reinforced materials. *Composites Part A: Applied Science and Manufacturing*, 38(11):2333 – 2341. CompTest 2006.
- Maimí, P., Camanho, P., Mayugo, J., and Dávila, C. (2007). A continuum damage model for composite laminates: Part i – Constitutive model. *Mechanics of Materials*, 39(10):897–908.
- Matzenmiller, A., Lubliner, J., and Taylor, R. (1995). A constitutive model for anisotropic damage in fiber-composites. *Mechanics of Materials*, 20(2):125 – 152.
- Normcommissie:310061 (1999). NEN-EN-ISO 14126 Fibre Reinforced Plastic Composites - Determination of compressive properties in the in-plane direction.
- Normcommissie:310061 (2012). NEN-EN-ISO 14129 Fibre Reinforced Plastic Composites - Determination of tensile properties - Part 1: General principles.
- Nunes, F., Silvestre, N., and Correia, J. R. (2016). Structural behaviour of hybrid frp pultruded columns. part 2: Numerical study. *Composite Structures*, 139:304–319.
- Nunes, F., Silvestre, N., and Correia, J. R. (2017). Progressive damage analysis of web crippling of gfrp pultruded i-sections. *Journal of Composites for Construction*, 21(3):04016104.

- Pearce, G., Johnson, A., Hellier, A., and Thomson, R. (2014). A study of dynamic pull-through failure of composite bolted joints using the stacked-shell finite element approach. *Composite Structures*, 118:86–93.
- Prince-Lund Engineering, P. (2011). Frp reinforcement for structures.
- Rahimian Koor, S. S., Karimzadeh, A., Yidris, N., Petru, M., Ayatollahi, M. R., and TAMIN, M. (2020). An energy-based concept for yielding of multidirectional frp composite structures using a mesoscale lamina damage model. *Polymers*, 12:1–18.
- Rudnicki, J. and Rice, J. (1975). Conditions for the localization of deformation in pressure-sensitive dilatant materials. *Journal of the Mechanics and Physics of Solids*, 23(6):371 – 394.
- Sungkha777 (2016). Cc by-sa 3.0. via Wikimedia Commons.
- Systèmes, D. (2011). Abaqus/CAE User's Manual. .
- Tan, J., Deshpande, V., and Fleck, N. (2016). Prediction of failure in notched carbon-fibre-reinforced-polymer laminates under multi-axial loading. *Philosophical Transactions of the Royal Society A: Mathematical, Physical and Engineering Sciences*, 374:20150273.
- Tsai, S., Aeronautics, U. S. N., Administration, S., and Corporation, P. (1965). *Strength Characteristics of Composite Materials*. NASA contractor report. National Aeronautics and Space Administration.
- Ubaid, J., Kashfuddoja, M., and Ramji, M. (2014). Strength prediction and progressive failure analysis of carbon fiber reinforced polymer laminate with multiple interacting holes involving three dimensional finite element analysis and digital image correlation. *International Journal of Damage Mechanics*, 23(5):609–635.
- Uddin, N. (2013). *Developments in fiber-reinforced polymer (FRP) composites for civil engineering*. Elsevier.
- Unnthorsson, R. and Runarsson, T. (2020). Ndt methods for evaluating carbon fiber composites.
- Vignjevic, R., Djordjevic, N., Gemkow, S., Vuyst, T. D., and Campbell, J. (2014). Sph as a nonlocal regularisation method: Solution for instabilities due to strain-softening. *Computer Methods in Applied Mechanics and Engineering*, 277:281 – 304.
- Vignjevic, R., Djordjevic, N., Vuyst, T. D., and Gemkow, S. (2018). Modelling of strain softening materials based on equivalent damage force. *Computer Methods in Applied Mechanics and Engineering*, 335:52 – 68.
- Xin, H., Liu, Y., Mosallam, A. S., He, J., and Du, A. (2017). Evaluation on material behaviors of pultruded glass fiber reinforced polymer (gfrp) laminates. *Composite Structures*, 182:283–300.



Damage variables one-element model

A.1. Conventional shell element results

The displacement of the conventional shell models with a size of 1.0 by 1.0 millimetre is depicted in figure A.1, for each of the four failure modes.

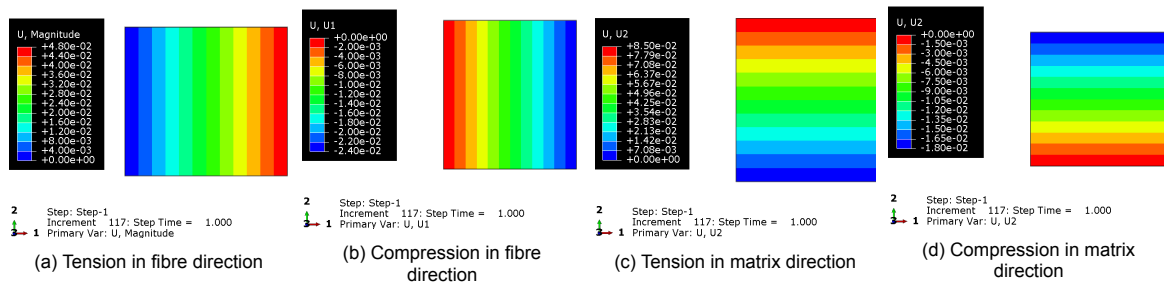


Figure A.1: Applied displacement for the conventional shell models of 1.0 by 1.0 millimetres for each of the four loading directions

A.1.1. Damage variables

The damage variables describe if the model is damaged in one of the four failure modes. For the 1.0 by 1.0 millimetres models the damage variables for a failed element are shown in figure A.7 up to and including A.10. When the material strength is reached, the damage variable in the direction of the loading should be '1.0', which equals completely damaged, and in the other directions '0.0', which equals no damage.

Tension in fibre direction

The damage variable for tension in fibre direction is '1.0', while the other three damage variables are '0.0'. Only failure in tension in fibre direction occurred.

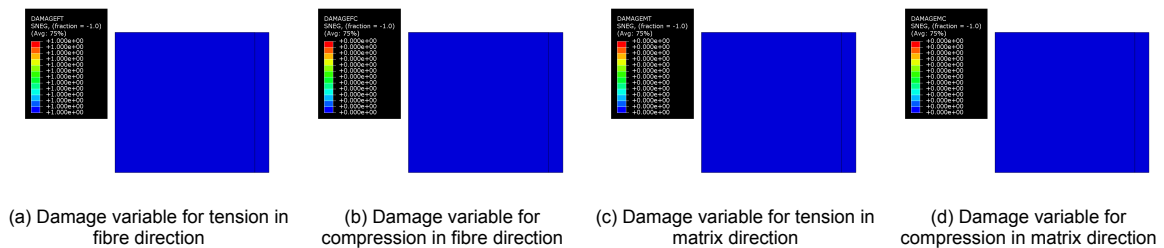


Figure A.2: The four damage variables for the conventional shell model loaded in tension in fibre directions

Compression in fibre direction

The damage variable for compression in fibre direction is '1.0', while the other three damage variables are '0.0'. Only failure in compression in fibre direction occurred.

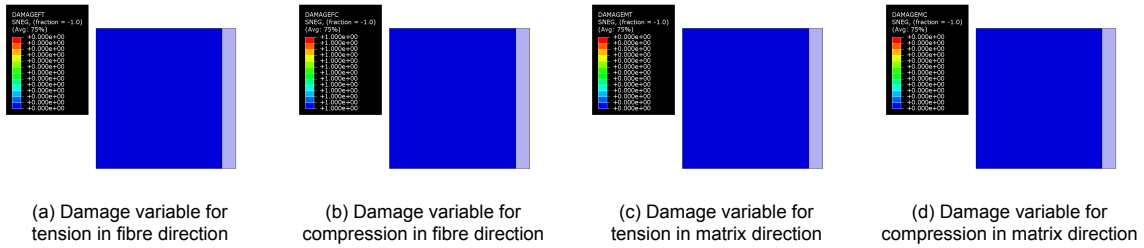


Figure A.3: The four damage variables for the conventional shell model loaded in tension in fibre directions

Tension in matrix direction

The damage variable for tension in matrix direction is '1.0', while the other three damage variables are '0.0'. Only failure in tension in matrix direction occurred.

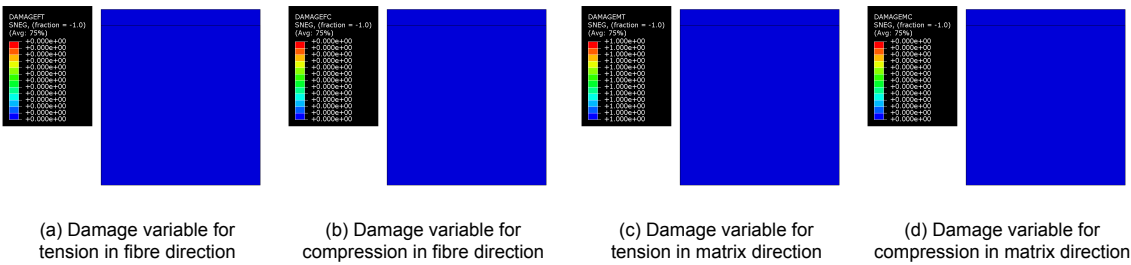


Figure A.4: The four damage variables for the conventional shell model loaded in tension in fibre directions

Compression in matrix direction

The damage variable for compression in matrix direction is '1.0', while the other three damage variables are '0.0'. Only failure in compression in matrix direction occurred.

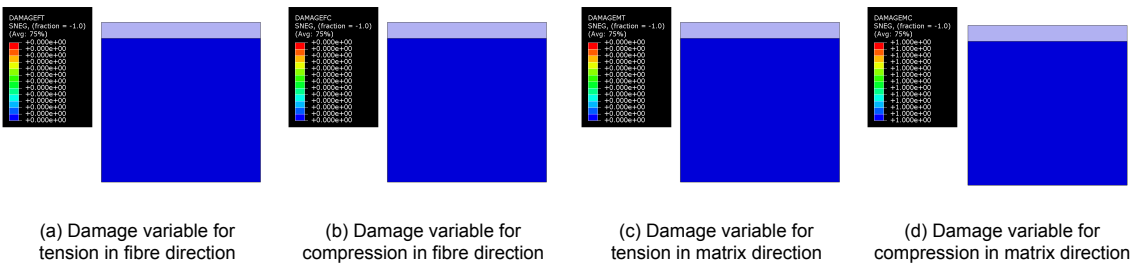


Figure A.5: The four damage variables for the conventional shell model loaded in tension in fibre directions

For each of the four models, only damage in the failure mode related to the respective loading direction developed.

A.2. Continuum shell element results

The displacement of the continuum shell models in each of the four loading directions is depicted in figure A.1.

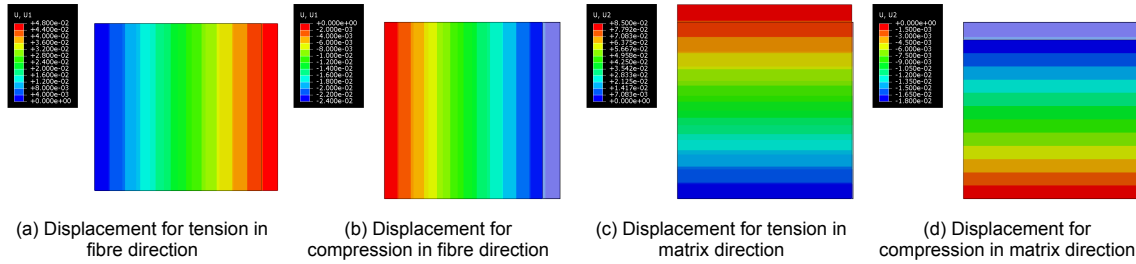


Figure A.6: The continuum shell model for each of the four loading directions in the displaced situation

A.2.1. Damage variables

The damage variables describe if the model is damaged in one of the four failure modes. For the 1.0 by 1.0 millimetres models the damage variables for a failed element are shown in figure A.7 up to and including A.10. When the material strength is reached, the damage variable in the direction of the loading should be '1.0', which equals completely damaged, and in the other directions '0.0', which equals no damage.

Tension in fibre direction

The damage variable for tension in fibre direction is '1.0', while the other three damage variables are '0.0'. Only failure in tension in fibre direction occurred.

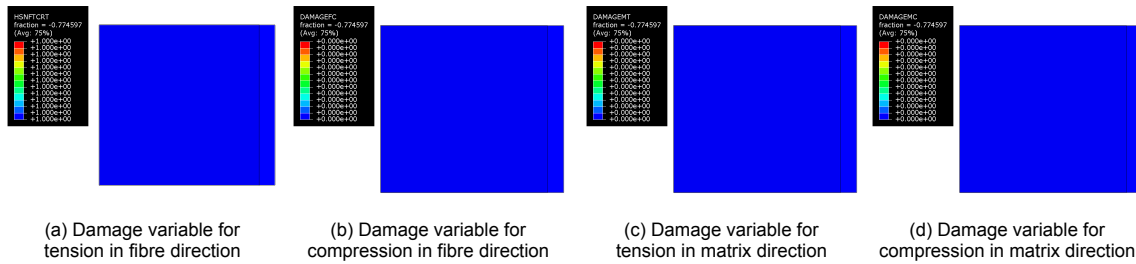


Figure A.7: The four damage variables for the continuum shell model loaded in tension in fibre directions

Compression in fibre direction

The damage variable for compression in fibre direction is '1.0', while the other three damage variables are '0.0'. Only failure in compression in fibre direction occurred.

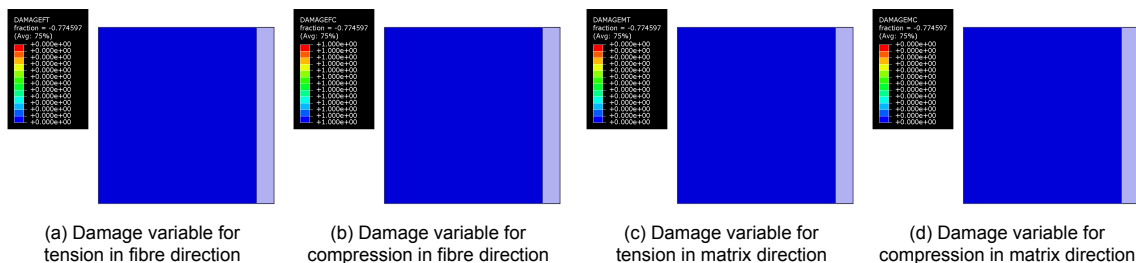


Figure A.8: The four damage variables for the continuum shell model loaded in tension in fibre directions

Tension in matrix direction

The damage variable for tension in matrix direction is '1.0', while the other three damage variables are '0.0'. Only failure in tension in matrix direction occurred.

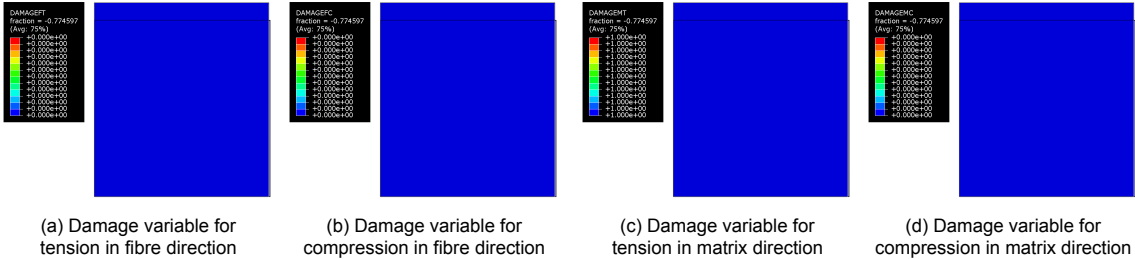


Figure A.9: The four damage variables for the continuum shell model loaded in tension in fibre directions

Compression in matrix direction

The damage variable for compression in matrix direction is '1.0', while the other three damage variables are '0.0'. Only failure in compression in matrix direction occurred.

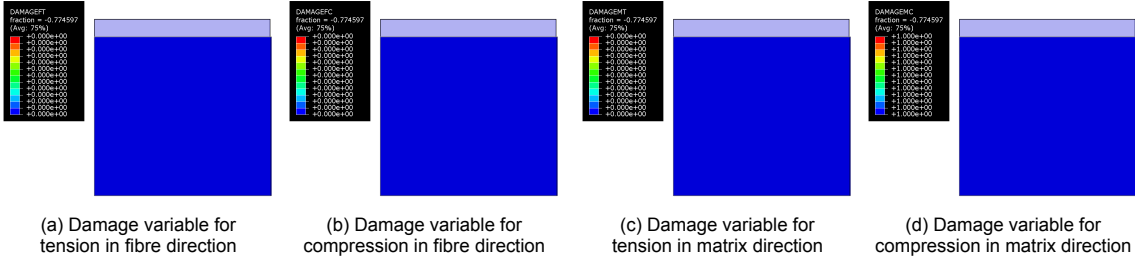


Figure A.10: The four damage variables for the continuum shell model loaded in tension in fibre directions

For each of the four models, only damage in the failure mode related to the respective loading direction developed.

B

Continuum shell model with cohesive zone modelling

The multi-directional coupons were modelled as a stacked continuum shell element with cohesive zone modelling (CZM). The stacked shell approach divides a laminate into multiple sub-laminates for one or more plies. A continuum shell element represents each sub-laminate, and the sub-laminates are coupled with a cohesive zone. This method can capture the failure behaviour of FRP well, including the occurrence of delamination. In this model, the cohesive zone is created with a surface-to-surface contact between the different plies. This approach is schematised in figure B.1. The contact properties for the surface-to-surface contact are stated in table B.1.

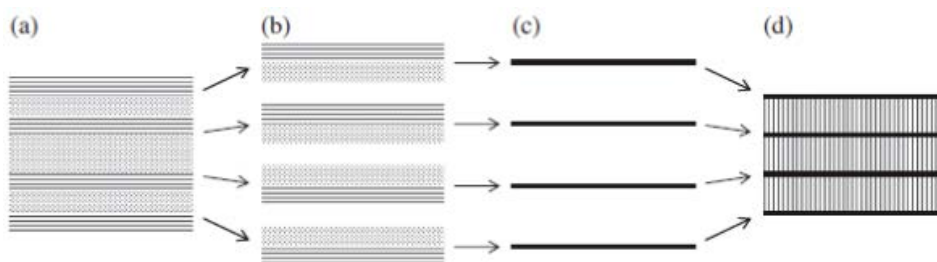


Figure B.1: Stacked shell method: (a) laminate cross-section, (b) laminate split in plies, (c) shell model of sub-laminates, (d) stacked shells with CZM (Pearce et al., 2014)

	Normal (Mode I)	1st shear (Mode II)	2nd shear (Mode III)
Strength (MPa)	25.8	31	31
Fracture Energy (N/mm)	1.1	2.79	2.79

Table B.1: Surface-to-surface properties \citep{Lieuwe}

The boundary conditions are shown in figure B.2. The applied mesh consists of SC8R elements: 8-node hexahedron, general-purpose and finite membrane strains. The characteristic element length is chosen to be equal to the thickness of each ply, which is 0.43 millimetres. Static general analysis has been performed. The solver failed before the ultimate strength was reached due to convergence issues, as shown in figure B.4. The numerical result is compared to the average experimental result. In implicit analyses, as used in Abaqus/Standard, strain-softening of materials often leads to convergence difficulties.

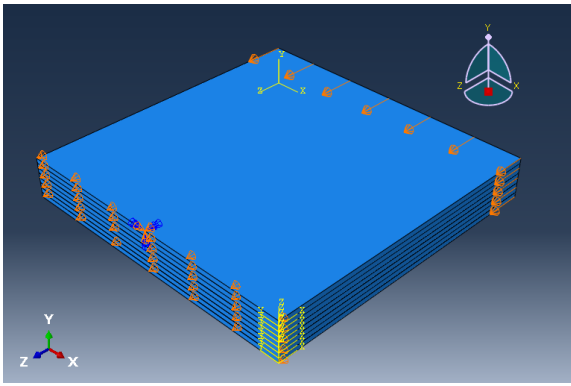


Figure B.2: Boundary conditions

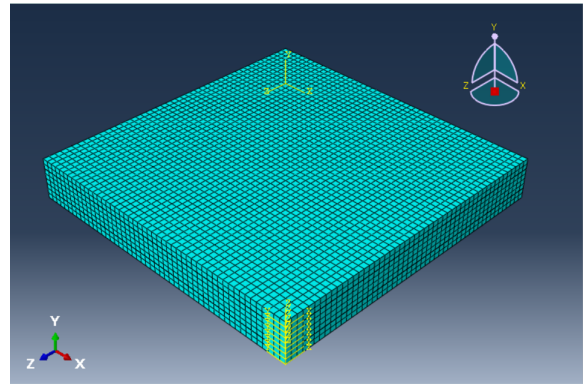


Figure B.3: SC8R elements with a length of 0.43 millimetre

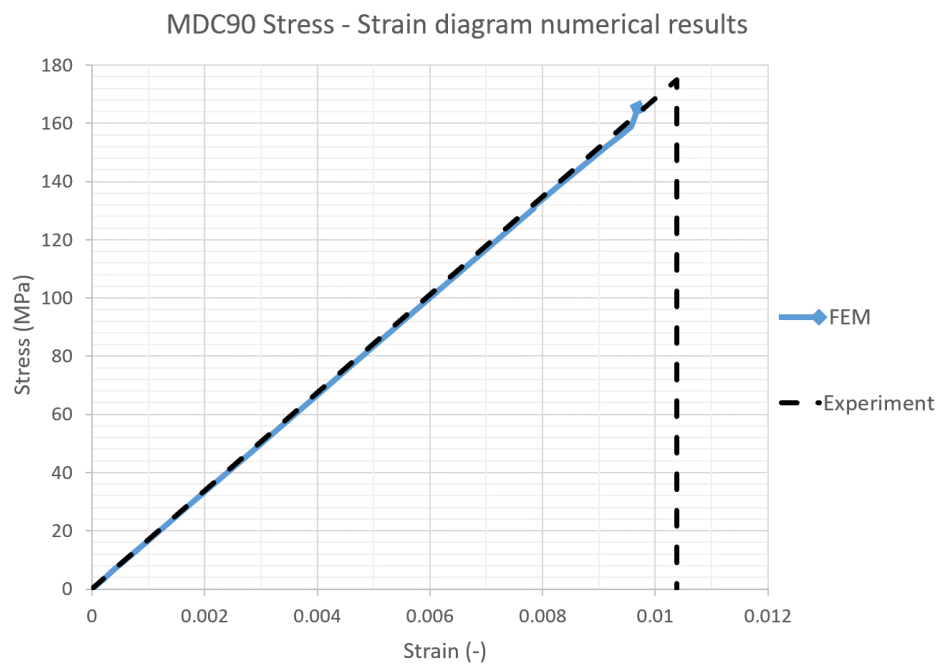
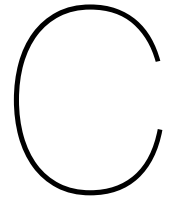


Figure B.4: Stress-strain curve continuum shell model with cohesive zone modelling



Classical Laminate Theory

Due to the anisotropic behaviour of FRP material, the description of elastic material is not the same as for engineering materials such as steel and concrete. The elastic properties of a laminate can be calculated with the classical laminate theory. This theory is based on the assumption that the deformation of the laminate behaves as a thin plate.

$$\varepsilon(x, y, z) = \varepsilon^0(x, y) + \kappa(x, y)z$$

- ε is the in plane strain vector;
- ε^0 is the strain at mid-plane;
- κ is the curvature;
- z is the thickness coordinate.

$$\begin{aligned}\varepsilon &= \{\varepsilon_{xx} \quad \varepsilon_{yy} \quad \gamma_{xy}\}^T \\ \varepsilon^0 &= \{\varepsilon_{xx}^0 \quad \varepsilon_{yy}^0 \quad \varepsilon_{xy}^0\}^T \\ \kappa &= \{\kappa_{xx} \quad \kappa_{yy} \quad \kappa_{xy}\}^T\end{aligned}$$

The stress resultants are calculated as distributed membrane forces, \mathbf{N} , and distributed bending moments, \mathbf{M} . The relation between the stress resultants and the deformation is as follows:

$$\begin{Bmatrix} \mathbf{N} \\ \mathbf{M} \end{Bmatrix} = \begin{bmatrix} \mathbf{A} & \mathbf{B} \\ \mathbf{B} & \mathbf{D} \end{bmatrix} \begin{Bmatrix} \varepsilon \\ \kappa \end{Bmatrix}$$

The components \mathbf{A} , \mathbf{B} and \mathbf{D} are 3×3 stiffness matrices. A multi-layered material has different elastic properties for each layer with a different fibre direction. Plies from the same material have the same $\overline{\mathbf{Q}}$ matrix. However, the \mathbf{Q} matrices will differ because of the different fibre angles, which influence the transformation from the local to global coordinate frame. To transform from local to global coordinate frame, the following set of equations is used-the quantities defined in the local coordinate frame are indicated with an over-bar:

$$\sigma = \mathbf{Q}\varepsilon \quad \text{with} \quad \mathbf{Q} = \overline{\mathbf{Q}}\mathbf{T}^T$$

$$\bar{\mathbf{Q}} = \begin{bmatrix} \frac{1}{E_1} & -\frac{\nu_{12}}{E_1} & 0 \\ -\frac{\nu_{12}}{E_1} & \frac{1}{E_2} & 0 \\ 0 & 0 & \frac{1}{G_{12}} \end{bmatrix}^{-1}$$

$$\mathbf{T} = \begin{bmatrix} \cos^2 \theta & \sin^2 \theta & -2 \sin \theta \cos \theta \\ \sin^2 \theta & \cos^2 \theta & 2 \sin \theta \cos \theta \\ \sin \theta \cos \theta & -\sin \theta \cos \theta & \cos^2 \theta - \sin^2 \theta \end{bmatrix}$$

A component-wise calculation can be performed with the following formulas:

$$\begin{aligned} Q_{11} &= \bar{Q}_{11} \cos^4 \theta + \bar{Q}_{22} \sin^4 \theta + (2\bar{Q}_{12} + 4\bar{Q}_{66}) \sin^2 \theta \cos^2 \theta \\ Q_{12} &= (\bar{Q}_{11} + \bar{Q}_{22} - 4\bar{Q}_{66}) \cos^2 \theta \sin^2 \theta + \bar{Q}_{12} (\cos^4 \theta + \sin^4 \theta) \\ Q_{16} &= (\bar{Q}_{11} - \bar{Q}_{12} - 2\bar{Q}_{66}) \cos^3 \theta \sin \theta - (\bar{Q}_{22} - \bar{Q}_{12} - 2\bar{Q}_{66}) \cos \theta \sin^3 \theta \\ Q_{22} &= \bar{Q}_{11} \sin^4 \theta + \bar{Q}_{22} \cos^4 \theta + (2\bar{Q}_{12} + 4\bar{Q}_{66}) \sin^2 \theta \cos^2 \theta \\ Q_{26} &= (\bar{Q}_{11} - \bar{Q}_{12} - 2\bar{Q}_{66}) \sin^3 \theta \cos \theta - (\bar{Q}_{22} - \bar{Q}_{12} - 2\bar{Q}_{66}) \sin \theta \cos^3 \theta \\ Q_{66} &= (\bar{Q}_{11} + \bar{Q}_{22} - 2\bar{Q}_{12} - 2\bar{Q}_{66}) \sin^2 \theta \cos^2 \theta + \bar{Q}_{66} (\sin^4 \theta + \cos^4 \theta) \end{aligned}$$

The **A**, **B** and **D** matrices of the laminate depend on the parameter h , which is the vertical position of the ply from the mid-plane, and are calculated as follows:

- The extensional stiffness matrix:

$$\mathbf{A} = \sum_{j=1}^n (z_j - z_{j-1}) \mathbf{Q}_j$$

- The strain-curvature coupling stiffness matrix:

$$\mathbf{B} = \sum_{j=1}^n \frac{1}{2} (z_j^2 - z_{j-1}^2) \mathbf{Q}_j$$

- The bending stiffness matrix:

$$\mathbf{D} = \sum_{j=1}^n \frac{1}{3} (z_j^3 - z_{j-1}^3) \mathbf{Q}_j$$

The critical buckling load is dependent on the material properties, boundary- and loading conditions, which are stated in table C.1. The length and width are described with a and b , m is the number of half-waves of the plate and, AR is the aspect ratio, which is the ratio between the width and the length of the plate.

E1	E2	G12	v12	a	b	m	AR	t
41.7	12	3.8	0.28	640	320	2	0.5	6.44
GPa	GPa	GPa	(-)	mm	mm	(-)	(-)	mm

Table C.1: Material properties and buckling coefficients

Implementing the material properties of the GFRP plate results in the following matrices:

$$\bar{\mathbf{Q}} = \begin{bmatrix} 42.66 & 3.44 & 0.00 \\ 3.44 & 12.28 & 0.00 \\ 0.00 & 0.00 & 3.80 \end{bmatrix}^{-1}$$

$$\mathbf{A} = \begin{bmatrix} 227.12 & 37.78 & 0.00 \\ 37.78 & 122.60 & 0.00 \\ 0.00 & 0.00 & 40.28 \end{bmatrix}$$

$$\mathbf{B} = \begin{bmatrix} 0.00 & 0.00 & 0.00 \\ 0.00 & 0.00 & 0.00 \\ 0.00 & 0.00 & 0.00 \end{bmatrix}$$

$$\mathbf{D} = \begin{bmatrix} 816.12 & 117.68 & 7.25 \\ 117.68 & 626.07 & 7.25 \\ 7.25 & 7.25 & 127.51 \end{bmatrix}$$

The critical buckling load is calculated according to the following formula for simply supported boundary conditions (SS):

$$N_o = \frac{\pi^2 [D_{11}m^4 + 2(D_{12} + 2D_{66})m^2(AR)^2 + D_{22}(AR)^4]}{a^2m^2}$$

The critical buckling load is calculated according to the following formula for clamped boundary conditions (CC):

$$\lambda = \frac{a}{b} \left(\frac{D_{22}}{D_{11}} \right)^{1/4} \quad N_o = \frac{\pi^2}{b^2} \sqrt{D_{11}D_{22}} (K) \quad K = \frac{4^2}{\lambda^2} + \frac{8(D_{12} + 2D_{66})}{3\sqrt{D_{11}D_{22}}} + 4\lambda^2 \quad 0 < \lambda < 1.094$$

$$K = \frac{m^4 + 8m^2 + 1}{\lambda^2(m^2 + 1)} + \frac{2(D_{12} + D_{66})}{\sqrt{D_{11}D_{22}}} + \frac{\lambda^2}{m^2 + 1} \quad \lambda > 1.094$$

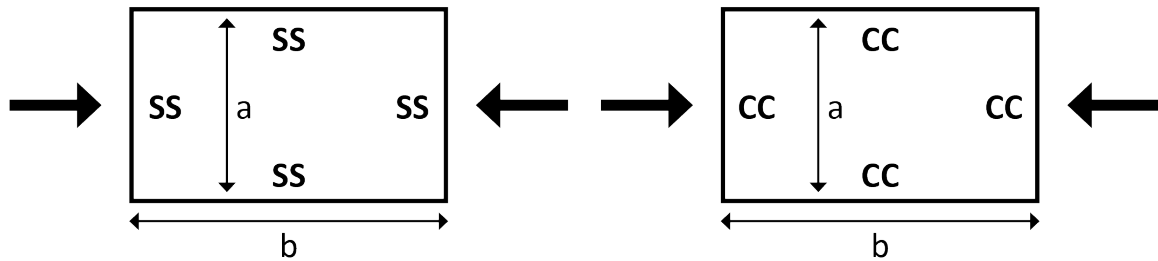
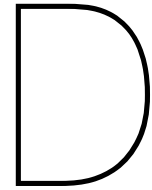


Figure C.1: Critical buckling load for a plate with clamped boundary conditions (CC) and simply supported boundary conditions (SS)

The critical buckling load results from Abaqus and the equations above are presented and compared in table C.2. For the two thinnest plates, the analytical results return lower critical buckling values, and for the other plate thicknesses, the analytical results are higher than the numerical results. The difference is higher for the plates with clamped boundary conditions, with a difference of up to 39%, compared to the simply supported boundary conditions, where the most significant difference is 24%. How thicker the plate, how larger the difference between the analytical and numerical results.

BC	Plate thickness (mm)	Abaqus result (kN)	Calculated result (kN)	Difference (%)
SS	6.88	69.34	67.08	-3.4%
SS	10.40	233.90	231.71	-0.9%
SS	13.76	532.33	536.67	0.8%
SS	16.00	825.45	843.74	2.2%
SS	20.64	1719.36	1811.25	5.1%
SS	24.00	2640.84	2847.62	7.3%
SS	27.52	3880.03	4293.33	9.6%
SS	32.00	5890.92	6749.92	12.7%
SS	34.40	7176.26	8385.41	14.4%
SS	41.28	11685.50	14489.98	19.4%
SS	48.00	17265.50	22780.99	24.2%
CC	6.88	128.56	127.92	-0.5%
CC	10.40	449.82	441.84	-1.8%
CC	13.76	1017.64	1024.45	0.7%
CC	16.00	1569.97	1608.90	2.4%
CC	20.64	3216.35	3453.81	6.9%
CC	24.00	4860.15	5430.04	10.5%
CC	27.52	6997.06	8186.80	14.5%
CC	32.00	10311.40	12871.20	19.9%
CC	34.40	12343.80	15989.85	22.8%
CC	41.28	19036.90	27630.45	31.1%
CC	48.00	26476.20	43440.28	39.1%

Table C.2: Numerical and analytical determined critical buckling load and their difference for varying plate thickness with two types of boundary conditions



Stress-displacement buckling models

The stress-displacement curves of the plates used to create the buckling curves discussed in chapter 6. Simply supported and clamped boundary conditions are represented in the first and second section, respectively. The thickness of the plates ranges from 6.88 to 48.00 millimetres. Progressive failure analysis is performed on each plate with six different initial imperfection sizes, ranging from B/1000 to B/125. 'LBA' represents the critical buckling stress determined from linear buckling analysis. Thin plates buckle when they reach the critical buckling stress and continue to carry the loading until the material strength is reached. Thick plates fail before reaching their critical buckling stress.

D.1. Simply supported boundary conditions

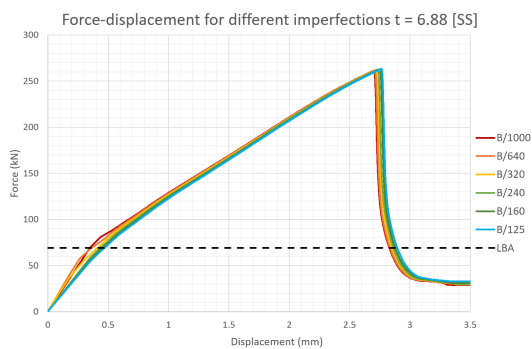


Figure D.1: Stress-displacement curve for laminate thickness 6.88 mm

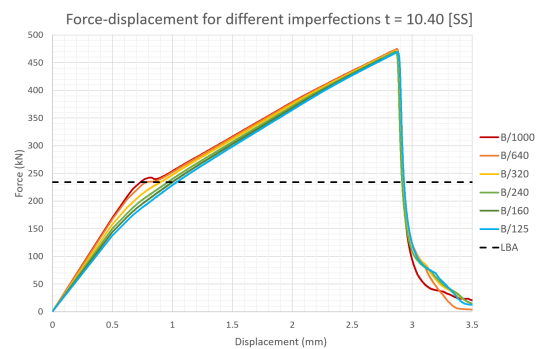


Figure D.2: Stress-displacement curve for laminate thickness 10.40 mm

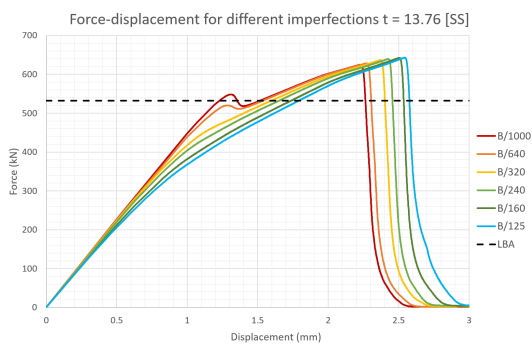


Figure D.3: Stress-displacement curve for laminate thickness 13.76 mm

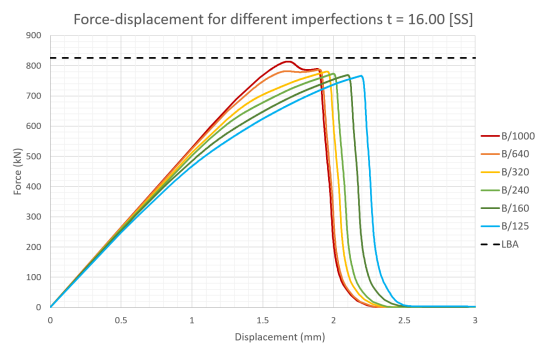


Figure D.4: Stress-displacement curve for laminate thickness 16.00 mm

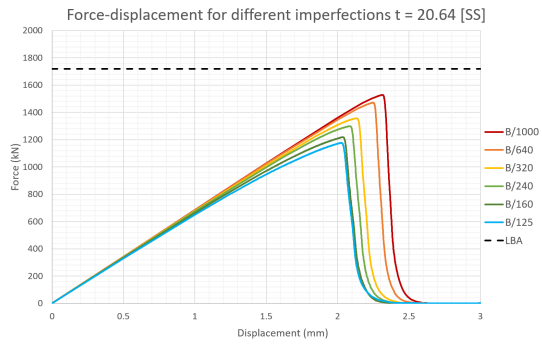


Figure D.5: Stress-displacement curve for laminate thickness 20.64 mm

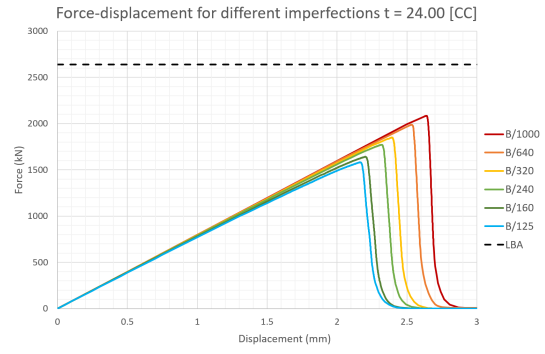


Figure D.6: Stress-displacement curve for laminate thickness 24.00 mm

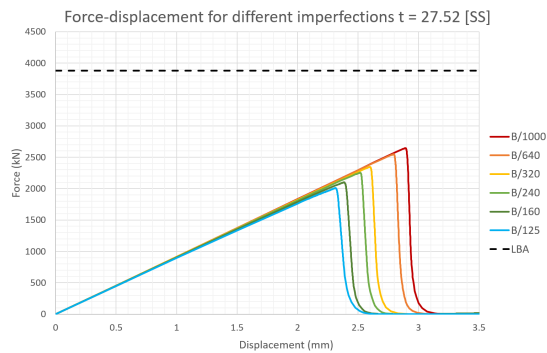


Figure D.7: Stress-displacement curve for laminate thickness 27.52 mm

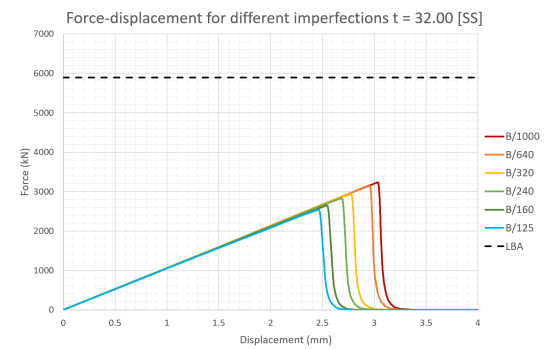


Figure D.8: Stress-displacement curve for laminate thickness 32.00 mm

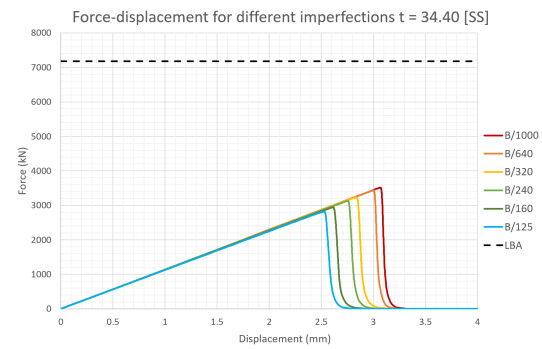


Figure D.9: Stress-displacement curve for laminate thickness 34.40 mm

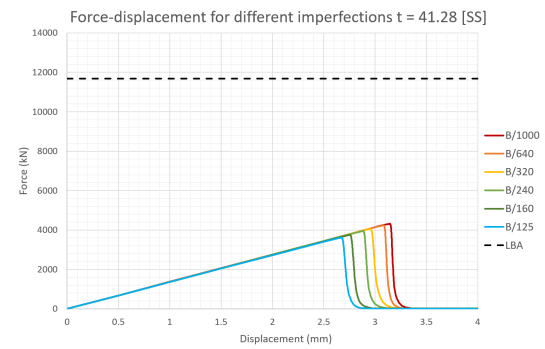


Figure D.10: Stress-displacement curve for laminate thickness 41.28 mm

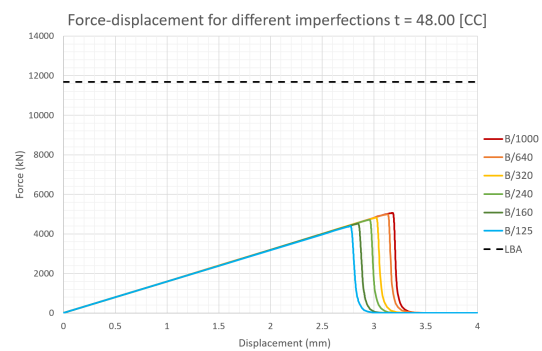


Figure D.11: Stress-displacement curve for laminate thickness 48.00 mm

D.2. Clamped boundary conditions

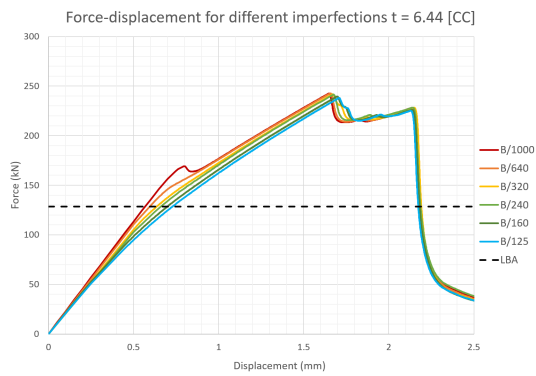


Figure D.12: Stress-displacement curve for laminate thickness 6.88 mm

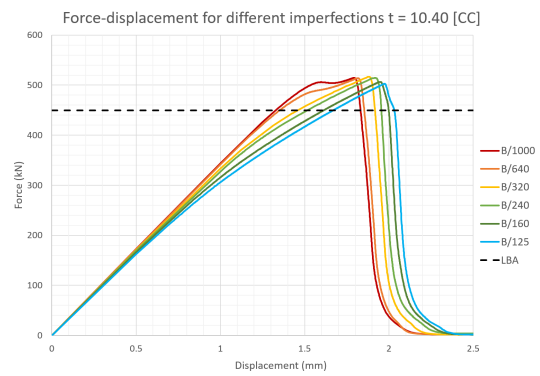


Figure D.13: Stress-displacement curve for laminate thickness 10.40 mm

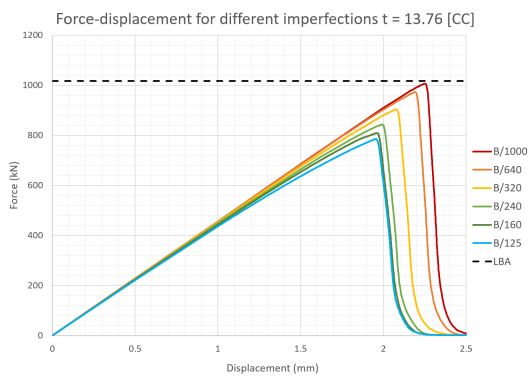


Figure D.14: Stress-displacement curve for laminate thickness 13.76 mm

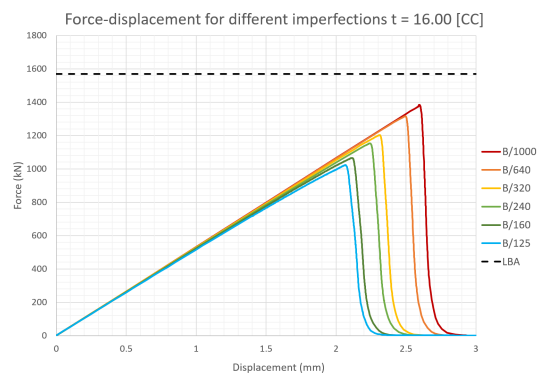


Figure D.15: Stress-displacement curve for laminate thickness 16.00 mm

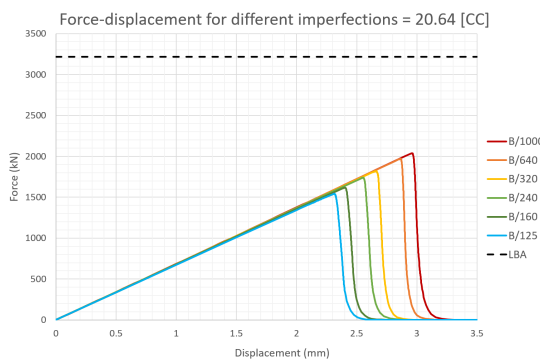


Figure D.16: Stress-displacement curve for laminate thickness 20.64 mm

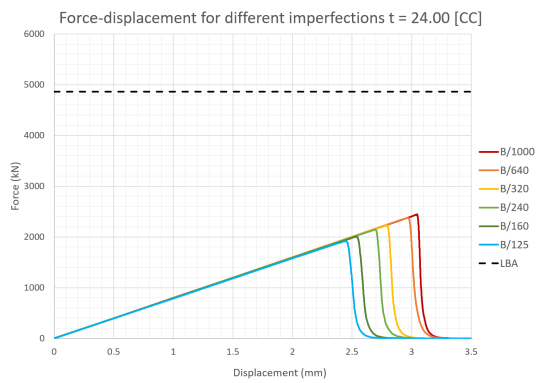


Figure D.17: Stress-displacement curve for laminate thickness 24.00 mm

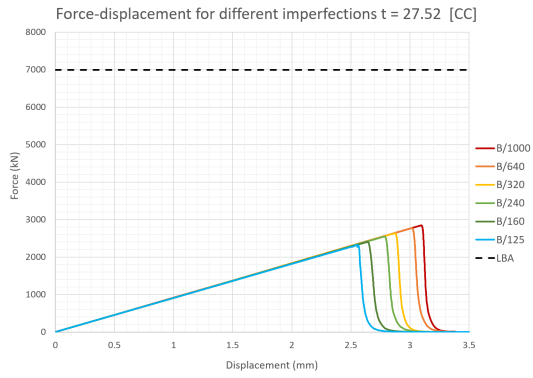


Figure D.18: Stress-displacement curve for laminate thickness 27.52 mm

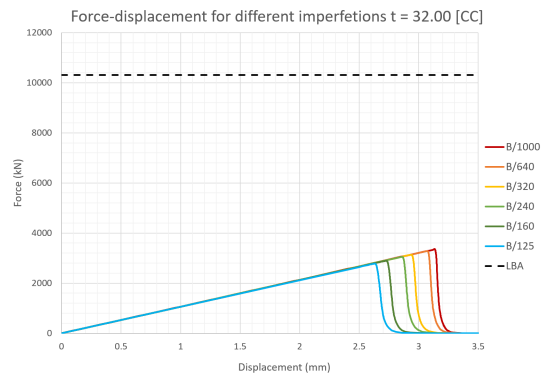


Figure D.19: Stress-displacement curve for laminate thickness 32.00 mm

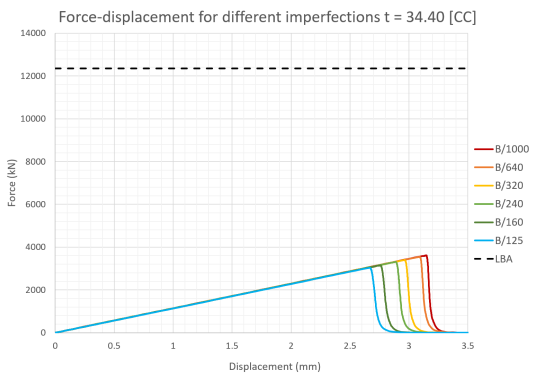


Figure D.20: Stress-displacement curve for laminate thickness 34.40 mm

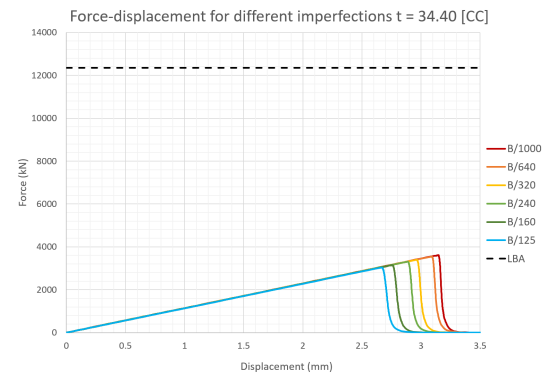


Figure D.21: Stress-displacement curve for laminate thickness 41.28 mm

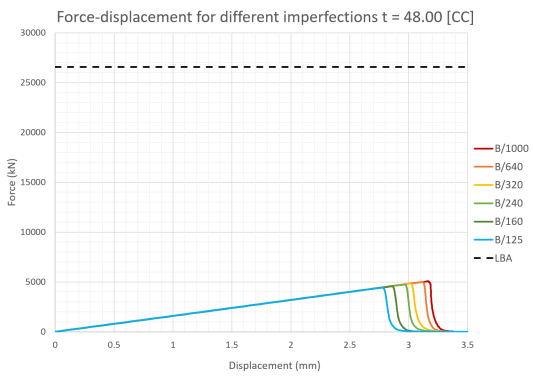


Figure D.22: Stress-displacement curve for laminate thickness 48.00 mm